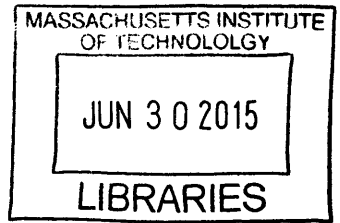


ARCHIVES



Gallium Nitride MEMS Resonators

by

Laura C. Popa

Submitted to the Department of Physics
in partial fulfillment of the requirements for the degree of

Doctor of Philosophy

at the

MASSACHUSETTS INSTITUTE OF TECHNOLOGY

February 2015

© Massachusetts Institute of Technology 2015. All rights reserved.

Signature redacted

Author

Department of Physics
January 30, 2015

Signature redacted

Certified by

Dana Weinstein
Associate Professor
Thesis Supervisor

Signature redacted

Certified by

Pablo Jarillo-Herrero
Associate Professor
Thesis Supervisor

Signature redacted

Accepted by

Krishna Rajagopal
Chairman, Department of Physics

Gallium Nitride MEMS Resonators

by

Laura C. Popa

Submitted to the Department of Physics
on January 30, 2015, in partial fulfillment of the
requirements for the degree of
Doctor of Philosophy

Abstract

As a wide band-gap semiconductor, with large breakdown fields and saturation velocities, Gallium Nitride (GaN) has been increasingly used in high-power, high-frequency electronics and monolithic microwave integrated circuits (MMICs). At the same time, GaN also has excellent electromechanical properties, such as high acoustic velocities and low elastic losses. Together with a strong piezoelectric coupling, these qualities make GaN ideal for RF MEMS resonators. Hence, GaN technology offers a platform for the seamless integration of low-loss, piezoelectric RF MEMS resonators with high power, high frequency electronics. Monolithic integration of MEMS resonators with ICs would lead to reduced parasitics and matching constraints, enabling high-purity clocks and frequency-selective filters for signal processing and high-frequency wireless communications.

This thesis highlights the physics and resonator design considerations that must be taken into account in a monolithically integrated solution. We then show devices that achieve the highest frequency-quality factor product in GaN resonators to date (1.56×10^{13}). We also highlight several unique transduction mechanisms enabled by this technology, such as the ability to use the 2D electron gas (2DEG) channel of High Electron Mobility Transistors (HEMTs) as an electrode for transduction. This enables a unique out-of-line switching capability which allowed us to demonstrate the first DC switchable solid-state piezoelectric resonator. Finally, we discuss the benefits of using active HEMT sensing of the mechanical signal when scaling to GHz frequencies, which enabled the highest frequency lithographically defined resonance reported to date in GaN (3.5 GHz). These demonstrated features show high potential for low-loss, reconfigurable systems for wireless communications.

Thesis Supervisor: Dana Weinstein
Title: Associate Professor

Thesis Supervisor: Pablo Jarillo-Herrero
Title: Associate Professor

Acknowledgments

There are many people that I am deeply grateful to for their support over the past years, without which this work would have not been possible. First, it has been a great pleasure to work under the supervision of Prof. Dana Weinstein, who had enough faith in me to take me on as a graduate student without any prior experience in MEMS or microfabrication. She is the one who introduced me to the world of MEMS, and provided the technical support for me to become well-versed in this topic. I am extremely thankful for all of her guidance, support and encouragement during these years.

I am also extremely grateful to my thesis committee, Professors Pablo Jarillo-Herrero, Nergis Mavalvala, and Raymond Ashoori, for finding time in their busy schedules to meet with me and provide useful feedback and comments.

A crucial part of the PhD experience was learning and growing as a researcher together with my classmates and labmates. I am particularly thankful to past and present members of our research group, HybridMEMS: Radhika Marathe, Wentao Wang, Bichoy Bahr, Siping Wang, Matt Storey, Tianyi Zeng, Gunjan Agarwal, Bethany Kroese, and Steven Ye. I thank them for many useful technical discussions, as well as for their support and friendship during these past years. Additionally, I would like to thank Prof. Tomas Palacios and his research group (Advanced Semiconductor Materials and Devices) for sharing their wisdom in GaN fabrication, especially Daniel Piedra, Omair Saadat, and Mohamed Azize. I am particularly thankful to Mohamed for his constant support throughout my PhD, and for assisting me with the measurement of my very first fabricated GaN sample.

A large part of my research was dependent on microfabrication, and I couldn't have made any progress without the help of our amazing support staff at the Microsystems Technology Labs at MIT. I am particularly indebted to Vicky Diadiuk, Dennis Ward, Eric Lim, Paul Tierney, Donal Jamieson, Dave Terry, Paul McGrath, Paudely Zamora, Dan Adams and Ryan O'Keefe. Besides technical staff, there are also many people on the administrative team that did their best to ensure that we

had all the resources to proceed with our work. A few names that come to mind are Ludmilla Leoparde, Valerie DiNardo and Steven O'Hearn. Besides, I would like to thank Debb Hodges-Pabon for all her care, support and friendship during these past years. It is people like her that make MTL a special, nurturing community. Additionally, from the Physics Department, I had a lot of help and support from Cathy Modica, Crystal Nurazura and Katie Lewis.

The ground-breaking results demonstrated in this work were mainly possible through access to superior GaN material quality, which was provided to us by Raytheon. I am particularly thankful to Dr. Thomas Kazior for providing these resources, as well as for all of his guidance and technical support during this collaboration. Additionally, I thank Dr. William Hoke and Dr. Brian Schultz for leading the MBE growth of GaN.

There are other sources of funding that made this work possible, including the MIT GaN Energy Initiative, and the DARPA Diverse Accessible Heterogeneous Integration (DAHI) Program. I am particularly thankful to Dr. Daniel Green and his team for leading the DAHI effort and providing useful feedback and guidance.

The chain of people that I inspired me to follow the path of pursuing a PhD in Physics begins long before graduate school. Starting with high-school in Romania, I am extremely grateful to my Physics teacher, Mihai Surdu, for wonderful and passionate lectures. I am also thankful to Adriana Tepelea for helping me perfect my English skills, as well as to my Romanian literature teacher, Codina Savulescu, for providing inspiration and knowledge that I used in many situations throughout my academic and personal life. Most of all, I will always cherish the memory of my Mathematics teacher, Dorin Moraru, for inspiring me to constantly work hard to achieve excellence. Some of the skills that I learned from him carried on for many years later, including my time as a PhD student.

I am also extremely grateful to all my friends that supported me during these past years. I am particularly grateful to Madalina Ursu, Ilinca Munteanu, Melania Macko and her entire family, Evelina Polyzoeva and Alex Guo. Additionally, my roommates in Boston, Roberto Sanchis-Ojeda, Eugene Yurtsev, Nuria Caniguer-

Vila, and Enrique Lizzaraga, have been like a second family to me and I am extremely grateful to have shared many good and bad moments throughout this journey.

Finally, I don't have enough words of appreciation to thank my family for all their support during the past years. I am extremely grateful for all of the sacrifices that my parents, Daniela and Sever, made so that I could study abroad and accomplish all of the great results that led to this PhD. Even more than that, I am thankful for all their efforts to introduce my brother and I to the world of Mathematics and Natural Sciences, from early on, which then carried throughout my entire educational path. I dedicate this work to them, for their constant support and love.

Contents

1	Introduction	27
1.1	Motivation	27
1.2	Electromechanical Devices in Wireless Communications	29
1.2.1	Quartz Resonators	31
1.2.2	Surface Acoustic Wave Devices	32
1.2.3	Bulk Acoustic and Film Bar Acoustic Resonators	32
1.2.4	Contour Mode MEMS Resonators	35
1.3	Gallium Nitride MEMS Resonators	36
1.3.1	GaN technology	36
1.4	Thesis Contribution	38
1.5	Thesis Outline	38
2	Theory and Modelling of Piezoelectric MEMS Resonators	41
2.1	Resonance and the Harmonic Oscillator	41
2.1.1	Simple Harmonic Oscillator	42
2.1.2	Damped Harmonic Oscillator	43
2.1.3	Driven, Damped Harmonic Oscillator: Resonance	46
2.2	Constitutive Relations for Waves Propagating in Elastic Media	48
2.2.1	Deformation and Strain	49
2.2.2	Stress and the Equation of Motion	50
2.2.3	Constitutive Relations: Hooke's Law	51
2.2.4	Wave equation	52
2.2.5	Lamb Mode Resonators	54

2.3	Transduction Mechanisms	56
2.3.1	Capacitive Transduction	58
2.3.2	Piezoelectric Transduction	59
2.3.3	Commonly Used Piezoelectric Transducers	61
2.3.4	Comparison Between Capacitive and Piezoelectric Transduction	63
2.3.5	Electromechanical Coupling Efficiency	66
2.4	Lumped Modeling of MEMS Resonators	69
2.4.1	Lumped Mechanical Components	69
2.4.2	Lumped Electrical Components	73
2.4.3	Modified Butterworth van Dyke Model	75
2.5	Dissipation Mechanisms in Acoustic Resonators	77
2.5.1	Air Damping	78
2.5.2	Surface Losses	79
2.5.3	Losses due to Mode Coupling	79
2.5.4	Loss due to Dissipation through Anchoring Beams	80
2.5.5	Thermoelastic Damping	80
2.5.6	Phonon-Phonon Scattering	80
2.5.7	Phonon-Electron Scattering	81
2.5.8	Intrinsic Loss in Gallium Nitride	83
3	Fabrication and Characterization	87
3.1	GaN Growth and Characterization	87
3.1.1	XRD	88
3.1.2	Nanoindentation	88
3.2	GaN Resonators in MMIC Technology	90
3.2.1	Au-based fabrication	90
3.2.2	Au-free HEMT Technology	95
3.3	Characterization	98
3.3.1	RF Measurements	98
3.3.2	De-embedding	99

3.3.3	Operation in Ambient Conditions	100
3.3.4	Power Handling	101
4	2D Electron Gas-Based Transduction	103
4.1	Motivation	103
4.2	2D Electron Gases in AlGa _N /Ga _N	105
4.3	Switchable Piezoelectric Transduction through Screening of the Acoustic Fields	108
4.3.1	Principle of Operation	108
4.3.2	Results	110
4.3.3	Discussion	111
4.4	Switchable Piezoelectric Transduction through Depletion of the 2DEG Electrodes	115
4.4.1	Motivation	115
4.4.2	Principle of Operation	115
4.4.3	Results	116
4.4.4	Discussion	119
4.5	Metal-Free Piezoelectric Resonators	119
4.5.1	Motivation	119
4.5.2	Principle of Operation	121
4.5.3	Results	122
4.5.4	Discussion	124
5	Lamb-Mode Resonators in Ga_N MMIC Technology	125
5.1	Motivation	125
5.2	Ga _N Lamb-mode resonators	127
5.3	Implementation in Ga _N MMIC Technology	133
5.4	Experimental Results	135
5.4.1	Parameter Extraction	140
5.4.2	Quality Factor	143
5.4.3	Transduction Efficiency	149

5.4.4	Ambient Operation and Power Handling	155
5.5	Discussion and Benchmarking	158
6	GaN Resonant Body Transistor	163
6.1	Motivation	163
6.2	Principle of operation	164
6.3	Experimental Results	167
6.3.1	DC Behavior of RBT	167
6.3.2	RF Behavior of RBT	169
6.4	Mechanically Coupled RBTs	169
6.4.1	Principle of Operation	169
6.4.2	Experimental Results	170
6.5	Discussion and Benchmarking	177
7	Conclusion	179
7.1	Summary of Results	179
7.2	Future Directions	181
7.2.1	Sensors	181
7.2.2	Mesoscopic Physics	182
A	Material Properties	185
A.1	Piezoelectric Wurtzite Materials	185
A.2	Isotropic Materials	187
B	Fabrication Procedures	189
B.1	Au-free Fabrication Procedure	189
B.2	Au-free Ohmic Optimization	195

List of Figures

1-1	Guglielmo Marconi operating apparatus similar to that used by him to transmit the first wireless signal across the Atlantic Ocean, 1901. . . .	28
1-2	(a) Prototype superheterodyne receiver built at Armstrong's Signal Corps laboratory in Paris during World War I (source:wikipedia.com). (b) Example of front-end architecture of modern superheterodyne receiver. Electromechanical resonators such as SAW, BAW or MEMS Resonators can be used as both frequency sources and filters due to their sharp inherent frequency response.	30
1-3	Original illustration of SAW Device demonstrated by White in 1965 [1].	32
1-4	Two commonly encountered Bulk Acoustic Wave (BAW) devices as introduced in [2].	33
1-5	Examples of various contour mode MEMS resonators: (a) Longitudinal bar (Lamb-wave) [3], (b) Lame mode [4], and (c) ring-extensional mode [5].	34
1-6	(a) Wurtzite crystal structure of GaN. (b) AlGa _N /GaN heterostructure can be grown on a variety of substrates, including Si-111, SiC, diamond, and sapphire.	36
2-1	A model of the simple harmonic oscillator.	41
2-2	Normalized amplitude of the damped harmonic oscillator for different values of the dissipation rate.	44
2-3	Amplitude (a) and phase (b) of the driven, damped harmonic oscillator for different values of the dissipation rate.	47

2-4	(a) Guided waves are propagating in an infinite plate of thickness $2d$ in the x-direction. The system of coordinates is placed with the center on the median plane of the plate. (b) Cross-section of infinite plane shows the zeroth order symmetric Lamb mode (S_0) propagating in the x-direction, for a normalized wavelength $\lambda/2d = 4.3$. In (c), the mode shape of the zeroth order antisymmetric mode (A_0) is shown for a normalized wavelength $\lambda/2d = 6$. In both cases, the superimposed arrows represent the displacement fields, while the color maps the strain fields.	56
2-5	Common types of transduction mechanisms that are compatible with major semiconductor technologies.	57
2-6	Electrostatic transduction of a longitudinal resonant bar (top-view) using two air-gap capacitors.	58
2-7	Common types of transducers used in piezoelectric acoustic devices. (a) Interdigital transducer. (b) Interdigital transducer with a grounded or floating electrode. (c) Fully electroded transducer. (d) 2 Port transducer with bottom electrode.	62
2-8	Piezoelectric transduction of a longitudinal resonant bar (side-view) using a fully electroded piezoelectric film.	63
2-9	Comparison between piezoelectric and electrostatic drive force for different (a) DC bias conditions and (b) different film thicknesses in the case of a longitudinal bar.	64
2-10	(a) Surface acoustic waves are propagating in the x_1 -direction through an infinite piezoelectric substrate. The system of coordinates is placed with the center on the median plane of the plate. (b) Setup for extracting the electromechanical coupling efficiency, k^2 , by computing the difference between the phase velocity when the top surface is set to zero charge (v_0) with the velocity under top surface shorting conditions (v_s).	68
2-11	Methodology for transforming a distributed MEMS resonator model to a lumped equivalent circuit in the electrical domain.	70

2-12	Methodology for transforming a distributed MEMS resonator model to a lumped equivalent circuit in the electrical domain.	71
2-13	Electromechanical analogue between spring-mass-damper in the mechanical domain and RLC network in the electrical one.	74
2-14	Equivalent circuit for modeling MEMS resonator.	76
2-15	Frequency response of MBVD model.	76
2-16	Calculated attenuation coefficients corresponding to the three intrinsic damping mechanisms: thermoelastic damping (TED), phonon-phonon scattering (phonon-phonon) and phonon-electron interactions (phonon-electron). The parameters used in this calculation are listed in Table 2.2.	85
2-17	Calculated (a) attenuation coefficients and (b) $f \cdot Q$ product corresponding to phonon-phonon scattering in GaN, for the 5 main wave types supported by this crystal symmetry. The parameters used in this calculation are listed in Table 2.2.	86
3-1	Structure of MBE-grown GaN on Silicon used in this work.	88
3-2	XRD spectroscopy of MBE GaN on silicon sample representative of the materials used in this thesis.	89
3-3	XRD spectroscopy of MBE GaN on silicon sample representative of the materials used in this thesis.	89
3-4	Fabrication process of GaN MEMS resonators in standard HEMT process with only two additional steps.	91
3-5	SEM image of resonator after the mesa etch step is finalized.	92
3-6	SEM image of resonator after the deep GaN etch is used to pattern the acoustic cavities.	93
3-7	SEM image of resonator after the ohmic metal deposition (a) before and (b) after anneal at $870^{\circ}C$ for 30 sec.	94
3-8	Released resonator.	94

3-9	Fabrication of GaN MEMS resonators in Au-free HEMT process with only two additional steps.	96
3-10	SEM images of HEMTs fabricated in a standard Au-based process (a) and in a Au-free process (b).	98
3-11	S-Parameter Approach for characterizing the response of a 2-Port device. The complex electrical circuit is treated as a "black box" with the terminals acting as the only connection to the external world. . .	99
3-12	Nonlinearity measurement approach. Two strong interfering signals spaced by $2\Delta\omega$ and $\Delta\omega$ will lead to a combined output at the resonant frequency (a). In (b) the Third Order Intercept is defined as the intersection point between the fundamental and nonlinear power outputs.	102
4-1	Example of possible architecture of the front-end of a radio component using MEMS resonators as filters.	104
4-2	AlGaIn/GaN heterostructure, grown epitaxially on a silicon substrate, using a thin AlN nucleation layer.	105
4-3	(a) Cross-section of AlGaIn/GaN heterostructure. (b) Different charge distributions that contribute to the formation of the 2DEG. (c) Energy band diagram, showing confinement of the 2DEG in a potential well at the interface of GaN with AlGaIn.	106
4-4	Switching of piezoelectric resonators through screening of the electric fields. In (a), the 2DEG under the IDT prevents the electric fields from penetrating the volume of the GaN. By applying a DC bias between the two finger sets in the IDT the 2DEG bunches and gets depleted from under one of the electrode pairs, allowing the fields to penetrate and launch acoustic waves.	108

4-5	Different combination of transducers that can be switched off through the screening of the fields. (a) Schottky-Schottky IDT. (b) Schottky-Ohmic IDT. (c) Schottky IDT with Ohmic control gates. (d) Ohmic IDT with Schottky control gates. (e) Schottky IDT with Schottky control gates.	109
4-6	(a) SEM image of a switchable piezoelectric resonator with gate IDT. (b) Measured frequency response for different DC biasing conditions applied to the RF signal electrode.	112
4-7	Driven Finite element analysis of the 2-Port resonator shown in Figure 4-6. (a) S_0 Lamb mode is excited uniformly through the entire width of the resonant cavity. (b) Standing waves get formed in the width dimension as well, giving rise to harmonics of the S_0 Lamb mode. . .	112
4-8	(a) SEM image of a switchable piezoelectric resonator with gate IDT and Schottky control gates. (b) Measured frequency response for different DC biasing conditions applied to the control gate.	113
4-9	Equivalent electrical model for a 2-Port resonator, showing the lumped mechanical branch (blue) and the electrical parasitics (red).	114
4-10	Principle of operation of switchable piezoelectric transducer through the depletion of the 2DEG electrode.	115
4-11	SEM of switchable resonator, a $7.3 \times 70 \mu m$ bar with symmetric electrode configuration for drive and sense.	116
4-12	Measured frequency response of passive resonator in air, showing 19 dB suppression of the signal when transducer is switched off ($V_{DC} = -7 V$).117	
4-13	Equivalent electrical model for a 2-Port switchable resonator using 2DEG bottom electrodes.	118
4-14	2DEG IDT resonators are realized starting from the AlGaIn/GaN heterostructure (a) by patterning 2DEG electrodes are patterned via a shallow AlGaIn etch (b).	120

4-15	(a) SEM of GaN resonator with 2DEG IDT. The 2DEG electrodes are patterned with a 70 nm deep AlGa _N etch. Ohmic contacts are used to access the 2DEG outside of the resonant structure. (b) Strain fields of the bulk contour mode excited using the 2DEG IDT.	120
4-16	Equivalent circuit model of 2DEG IDT. Elements in blue represent the mechanical resonance while elements in grey are electrical parasitics of the structure and are deembedded from the measurement.	122
4-17	(a) Frequency response of “Design A” resonator using 2DEG IDT after deembedding the electrical parasitics. (b) The deembedded measured response of a metal IDT resonator with equivalent design.	123
5-1	Cross-section of an infinite plate of finite thickness, h_{GaN} shows the first two Lamb modes propagating in the x-direction. The zeroth order symmetric Mode, S_0 , is shown for a normalized wavelength $\lambda/2d = 4.3$. The mode shape of the zeroth order antisymmetric mode, A_0 is shown for a normalized wavelength $\lambda/2d = 6$. Arrows represent the displacement fields, while the color maps the strain fields.	128
5-2	Typical interdigital transducer configurations (IDT) used to drive and sense Lamb waves. (a) uses a single metal layer at the top of the piezoelectric film to induce a periodic electric field through the substrate. (b) includes an additional bottom electrode that can be grounded to confine the electric fields in the piezoelectric field.	128
5-3	(a) Guided Lamb-modes propagate in the x-direction in an infinite plate of thickness h_{GaN} . (b) Unit cell used in FEM analysis to extract eigenmodes. (c) Electrical boundary conditions used to extract v_0 and v_s for the two IDT configurations.	129

5-4	Phase velocity dispersion curve for the first Lamb modes, A_0 and S_0 assuming massless electrodes of infinitesimal thickness. The phase velocity corresponding to Rayleigh waves in GaN is overlaid for comparison [6]. Insets show mode shape, with the color map corresponding to the displacement field.	131
5-5	Simulated intrinsic electromechanical coupling efficiency, k^2 of S_0 , and A_0 , respectively. The efficiency of a Rayleigh SAW propagating in GaN is also included for comparison [6].	132
5-6	Different IDT configurations that can be realized in a GaN-HEMT process using: (a) the gate metal, (b) the ohmic metal, (c) ohmic metal over patterned 2DEG electrodes and (d) 2DEG electrodes only.	133
5-7	(a) Unit cell used in frequency response FEM analysis. (b) Electric potential (color map) and fields (arrow plot) induced by the drive signal. (c) Simulated admittance for $h_{GaN} = 0.3$. Inset shows equivalent circuit model. (d) Resonant mode shape.	136
5-8	2D frequency response simulation of (a) phase velocity and (b) effective coupling efficiency, k_{Eff}^2	137
5-9	Fabrication process of GaN Lamb-Mode resonators integrated with HEMTs in a Au-free MMIC process. (a) Starting HEMT epitaxial heterostructure. (b) Standard HEMT front-end process. (c) First modification to HEMT process: deep GaN etch. (d) Second modification to HEMT process: isotropic silicon etch for MEMS release.	138
5-10	(a) SEM image of a 5 th harmonic 1 GHz Lamb Mode resonator. The 3D FEM simulation in (b) illustrates the strain fields induced at resonance.	138
5-11	(a) SEM image of a 15 th harmonic 1GHz Lamb-mode resonator. (b) Measured S Parameters under vacuum.	139

5-12	(a) Equivalent Circuit Model of the Lamb-mode resonators. (b) Frequency response of the device shown in Figure 5-11 is fitted over a wide frequency range, taking into account only the electrical parasitics. (c) Resonance peak is fitted to both mechanical branch and electrical parasitics.	140
5-13	Measured mechanical quality factors (a) and $f \cdot Q$ (b) for devices using three different IDT configurations: gate IDT, ohmic IDT, and ohmic with patterned 2DEG IDT.	145
5-14	Measured frequency response of a 1.9 GHz gate IDT resonator.	146
5-15	Electrically loaded quality factor, Q_L for devices using three different IDT configurations: gate IDT, ohmic IDT, and ohmic with patterned 2DEG IDT. Inset shows average extracted series resistance, scaled by the resonator width.	146
5-16	Mechanical quality factor of resonators with different number of harmonics.	147
5-17	(a) SEM image of a 25 th harmonic 1.9 GHz Lamb-mode resonator. (b) Measured S-Parameters under vacuum. Insets show 3D FEA simulation corresponding to resonance of interest and spurious mode.	150
5-18	(a) Equivalent Circuit Model including spurious mode contribution. (b) Frequency response of the device shown in Figure 5-11 is fitted over a wide frequency range, taking into account only the electrical parasitics. In (c), the resonance peak is fitted to both mechanical branch and electrical parasitics.	151
5-19	Comparison between simulated and measured (a) phase velocity and (b) transduction efficiency for 5 th harmonic devices using different transducers.	153
5-20	Comparison between simulated and measured transduction efficiency for higher harmonic devices using different transducers.	154
5-21	Ambient pressure dependence of mechanical quality factor for 1 GHz Lamb-mode resonator.	156

5-22	Temperature coefficient of frequency (TCF) for 1GHz Lamb-mode resonator.	157
5-23	Power handling measurement of the 1 GHz Lamb-mode resonator, with an IIP3 of 23.1 dBm, with $19.4 \times 90 \mu m^2$ footprint.	157
5-24	Measured $f \cdot Q_m$ from this work and other previously demonstrated GaN resonators from [7], [8], [9], [10], [11], and [12].	159
5-25	Measured k_{Eff}^2 (a) and $FOM = k_{Eff}^2 Q_m$ (b) from this work and other previously demonstrated GaN resonators from [8], [9].	160
6-1	Schematic of GaN Resonant Body Transistor, where acoustic vibrations are driven piezoelectrically across the AlGaIn layer, while sensing of mechanical waves is done with a HEMT.	164
6-2	Equivalent circuit model of the RBT. Blue elements represent the equivalent mechanical RLC branch, according to a Butterworth Van Dyke model while the right side captures the electromechanical transconductance.	166
6-3	SEM of piezoelectric-drive, HEMT-sensed $8.7 \times 70 \mu m$ resonator. The HEMT has gate length of $1 \mu m$	166
6-4	Measured IV curves of the HEMT embedded in resonator (a) before and (b) after release step.	167
6-5	Measured frequency response of PE drive-HEMT sense AlGaIn/GaN resonator, in air. The transconductance, $g_m = Y_{21} - Y_{12}$, is suppressed when the 2DEG under the drive electrode is depleted. The inset shows a FEA simulation of the cross-section of the sense HEMT, where the color map represents the strain fields induced at resonance.	168
6-6	Schematic of GaN Resonant Body Transistor. (a) Placement of drive transducer and sense transistor in the same acoustic cavity leads to broadband feed-through. (b) Electrical isolation between drive transducer and sense transistor is done by mechanically coupling two resonators.	170

6-7	SEM of mechanically coupled drive and sense resonators. Source and drain electrodes, and two additional floating electrodes are patterned to match the drive transducer. A 5-tether approach is implemented to allow for a larger heat sink due to the HEMT current, as well as for improved power handling and spurious mode reduction [13]. Trenches are patterned through GaN to provide stress relief and better isolation between drive/sense.	171
6-8	(a) 3D mode shape of strongly coupled resonators. (b) Gate of sense HEMT is placed at maximum strain. Source, drain and floating electrodes are patterned to match drive IDT.	171
6-9	Measured g_{em} of mechanically coupled RBT in Figure 6-7 shows $> 10\times$ reduction in broadband floor compared to previously reported results. Inset shows 180° phase shift corresponding to mechanical resonance. .	172
6-10	(a) DC behavior of embedded HEMT. (b) Dependence of g_{em} on drain voltage in the linear regime shows linear increase in acoustic transconductance, while floor remains mainly unchanged. (c) Dependence of g_{em} on gate voltage in the saturation regime shows optimal performance when the gate is set to -2 V.	173
6-11	SEM of mechanically coupled RBT, with coupling beam at maximum velocity point. The embedded HEMT has two fingers, with gate length of $3.7 \mu m$. Similar to the low-velocity case, trenches etched in GaN are used for stress relief and better isolation between drive/sense. An extra ground electrode is placed between the RF input and gate for better shielding.	174
6-12	Measured g_{em} for double-gate RBT shows an acoustic transconductance of $72 \mu S$, $> 2\times$ higher than previously reported GaN RBTs, with SNR > 50 . Inset shows DC IV characteristics of HEMT used for electromechanical transconductance.	175
6-13	Measured resonant frequency shift with drain current for low-velocity coupling device shows 0.2 % tuning capability.	175

7-1	Circuit micrograph of 1GHz monolithic Pierce oscillator with GaN Lamb-mode MEMS resonator [14].	181
7-2	Heterostructures with band structures that contain multiple potential wells can be realized (a). In the presence of an applied strain field (b), the barrier height between the two 2DEG regions will change, leading to variations in the tunneling probability between the two electron gases.	182
B-1	SEM of fabricated TLM structure used for extracting contact resistance of Ta-based Ohmic metal to the 2DEG.	195

List of Tables

1.1	Material properties of commonly encountered electromechanical materials.	37
2.1	Direct (current) analogy between the mechanical and electrical domain for a lumped MEMS resonator.	73
2.2	Material properties used to calculate intrinsic loss attenuation coefficient for bulk, wurtzite GaN.	84
4.1	2DEG properties for a typical MBE AlGa _N /Ga _N on silicon sample used in this work.	107
4.2	Comparison of Metal and 2DEG IDT Resonators.	124
5.1	Fitting parameters to the frequency response shown in Figure 5-12 . .	142
5.2	Fitting parameters to 1.9 GHz device shown in Figure 5-17.	152
6.1	Summary of mechanical performance of state-of-the art Ga _N RBTs shows 100× improvement in SNR in this work	177
A.1	Wurtzite Ga _N , Al _N and AlGa _N material properties used in simulation	186
A.2	Material properties of isotropic materials used in simulations.	187
B.1	Performance of different Ohmic metallizations as a function of anneal temperature.	196

Chapter 1

Introduction

1.1 Motivation

Ever since Guglielmo Marconi transmitted the first radio frequency (RF) signal over the Atlantic in 1901 (Figure 1-1), the demand for radio communications has been rapidly increasing. The past decades have seen a high usage of wireless capabilities, both for consumer and military applications. On the consumer side, the development of smart phones and wireless internet has been the primary driver for the development of radio hardware. At the same time, military and national security concerns have generated new paradigms in radio communications, including the notion of reconfigurable, frequency-hopping radios.

On the other hand, this rapid development of radio technology has enabled a plethora of applications such as inertial sensors for personal navigation, high definition video streaming and high speed image processing. This has led to the concept of Internet of Things, a network of ubiquitous, smart devices that are interconnected through a cloud. Devices to be incorporated in this Smart Grid range from implantable sensors and biochips, to inertial sensors for navigation, smart homes and cities, and field operation devices for rescue forces. In order to minimize the impact of these elements on the environment, ultra-compact, frequency-agile and power-efficient radios are needed. With exceptionally high quality factors (1000s at GHz frequencies) and small foot-prints ($10 - 100 \mu m^2$), acoustic Microelectromechanical systems

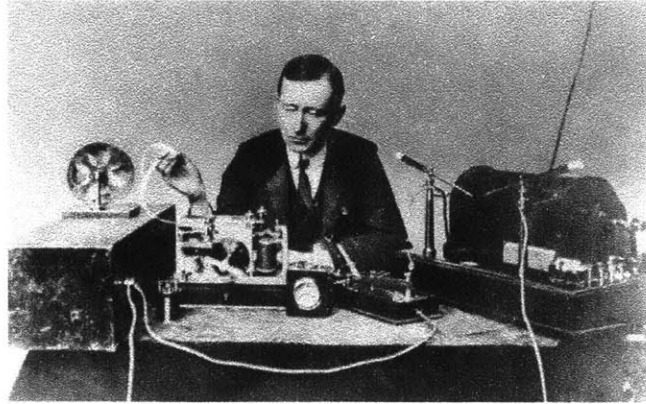


Figure 1-1: Guglielmo Marconi operating apparatus similar to that used by him to transmit the first wireless signal across the Atlantic Ocean, 1901.

(MEMS) resonators provide an attractive solution for realizing frequency sources and filters for compact, fully-integrated RF systems, as well as a wide spectrum of resonant sensors [15]. Additionally, MEMS resonators also have the capacity for monolithic integration with standard integrated circuits, which has the benefit of reduced size, weight, and power, improved parasitics, and reduced impedance matching constraints, particularly at high frequencies. A lot of effort has gone into the integration of silicon MEMS with CMOS [16], [17], leading to many low-power applications such as implantable transmitter-receivers (tranceivers) for prosthetics and wearable sensors [18]. However, for RF front-end operation, MEMS-based filters would require a more efficient transduction mechanism than the electrostatic one, such as the piezoelectric effect.

Additionally, this increase in the demand for wireless communications has turned the radio spectrum into a sparse resource. The main problem is the way in which radio spectrum is currently allocated. For example, in the United States, frequency bands are reserved for specific applications by the U.S. Federal Communications Commission (FCC). As a result, in some regions, the frequencies used by cellphones can be extremely congested, while large bands of the broadcast-television spectrum stand idle. One solution to that problem is the concept of “cognitive radio”, in which wireless devices would scan their environments for vacant frequencies and “hop” to these available bands for transmissions. This concept was first introduced by Mitola and

Maguire in 1999 [19]. Ever since, there have been various proposals for realizing cognitive radios, placing different emphases on hardware and software. In the hardware case, the essential component is a bank of filters that can isolate any frequency in a wide band. To achieve a cognitive, reconfigurable wireless system, we need new physics and devices to enable switchable devices and filters.

This thesis focuses on exploring new physics and transduction mechanisms in Gallium Nitride (GaN) MEMS resonators that would address the issues described above. We choose this platform due to several attractive features. First, as a wide band-gap semiconductor with large breakdown fields and saturation velocities, GaN has been increasingly used in high-power, high-frequency electronics and monolithic microwave integrated circuits (MMICs). At the same time, GaN also has excellent electromechanical properties, including high acoustic velocities and low elastic losses and a strong piezoelectric effect. These qualities make GaN ideal for RF MEMS resonators, and offers a platform for seamless integration of high performance RF MEMS resonators with high power, high frequency electronics. The novelty and high potential of this technology come from the presence of an inherent 2D electron gas (2DEG) present in this structure, which can lead to new acousto-electric capabilities for MEMS resonators. These include features such as the ability to use the 2DEG as an electrode for transduction in the first switchable piezoelectric resonator, as well as an active sensor of the mechanical vibrations, as the channel of a HEMT embedded in an acoustic cavity. These capabilities can lead to truly reconfigurable systems, for wide bandwidth wireless communications.

1.2 Electromechanical Devices in Wireless Communications

Many developments have happened on the front of radio hardware over the past decades leading to innovative solutions both at the component and system level, but the main principle of operation behind most modern radios nowadays still remains

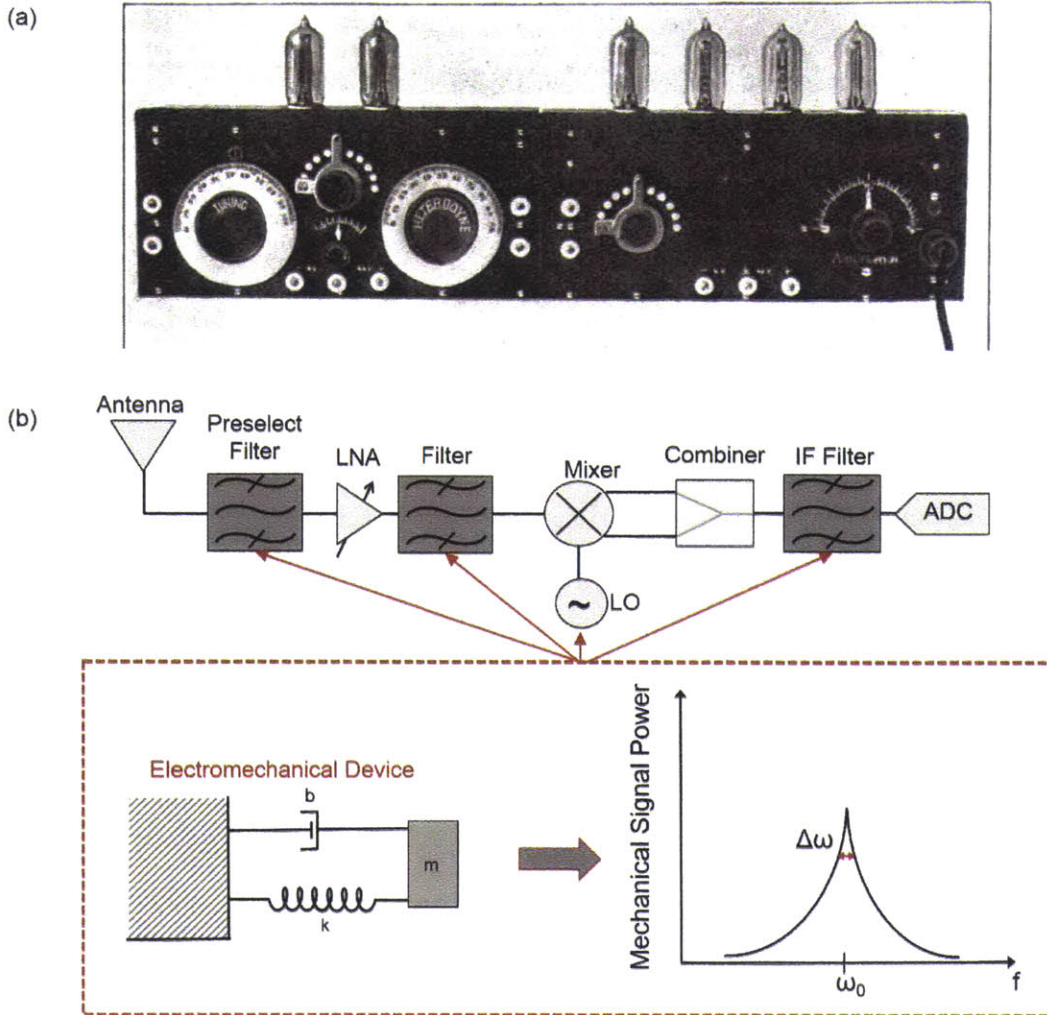


Figure 1-2: (a) Prototype superheterodyne receiver built at Armstrong's Signal Corps laboratory in Paris during World War I (source:wikipedia.com). (b) Example of front-end architecture of modern superheterodyne receiver. Electromechanical resonators such as SAW, BAW or MEMS Resonators can be used as both frequency sources and filters due to their sharp inherent frequency response.

the superheterodyne architecture (Figure 1-2 (a)). This was invented by US engineer Edwin Armstrong in 1918 during World War I and is based on the use of frequency mixing to convert a received signal to a fixed intermediate frequency (IF) which can be more conveniently processed than the original radio carrier frequency [20]. This leads to the trade-off between higher bandwidth selectivity and sensitivity and the cost, size and power associated with an additional frequency conversion stage. Figure 1-2 (b) shows a schematic of a possible front-end superheterodyne architecture of a radio. There are multiple frequency sources and filters that go into this system which are nowadays based on off-chip components, such as ceramic LC tanks or quartz resonators, which are bulky and power-hungry.

In this thesis we propose replacing some of the clocking and filtering components with integrated MEMS resonators. Due to their inherent sharp frequency response these devices can serve as both filters and frequency sources. High mechanical quality factors translate to low phase-noise for high-purity oscillators and excellent frequency selectivity for filter applications [21]. Additionally, we will show in this work that the platform developed here brings in new physics and transduction mechanisms that would eventually enable a novel class of reconfigurable radio systems. We start by looking at various examples of electromechanical devices that have been used for wireless communications, listing some of the advantages and disadvantages of each technology.

1.2.1 Quartz Resonators

Ever since the demonstration of the first quartz resonator in 1921 by Walter Cady [22], this has been the most commonly used technology for frequency sources and signal processing, due to its piezoelectric behavior, high quality factors, and excellent temperature stability. The frequency of operation of the quartz oscillator will depend on the crystal cut and orientation. In fact, there are very limited methods for micro-machining quartz, which limits these devices to off-chip, millimeter size components [23].

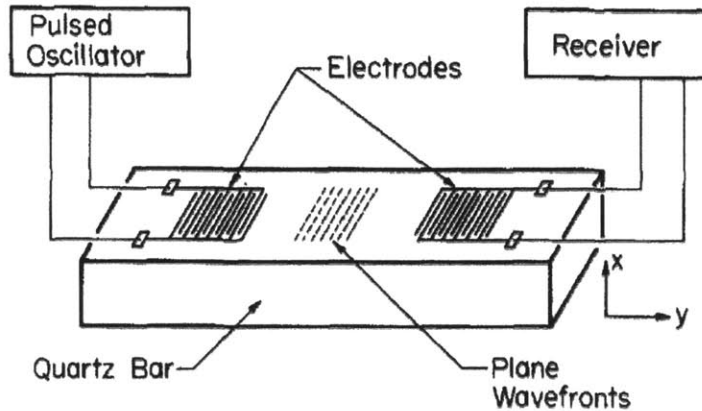


Figure 1-3: Original illustration of SAW Device demonstrated by White in 1965 [1].

1.2.2 Surface Acoustic Wave Devices

Surface acoustic wave (SAW) devices are based on Lord Rayleigh's proof in 1885 that waves can propagate at the surface of an semi-infinite medium. It took until 1965 for White [1] to demonstrate the transduction of SAW using an interdigital transducer on a piezoelectric medium, as shown in Figure 1-3. Nowadays, SAW devices are heavily used in Ultra-High-Frequency (UHF) filtering for wireless communications, for frequencies up to 2.5 GHz [24]. Since they don't require any post-processing and their fabrication is relatively simple, SAW can be integrated with IC's, especially with piezoelectric MMICs. However, due to high losses through the substrate, SAW devices need to be large to attain the low insertion losses required for operation, which places them on the order of millimeters.

1.2.3 Bulk Acoustic and Film Bar Acoustic Resonators

One way to address the need for miniaturization is by moving to Bulk Acoustic Wave (BAW) resonators, in which the waves propagate throughout the entire volume of the material and not just at the surface [2]. This type of wave is also stiffer, allowing higher frequencies of operation. While BAW devices can still approach millimeter sizes, they are typically smaller than their SAW counterparts. These devices are also IC-compatible and, additionally, BAW devices show better power handling and

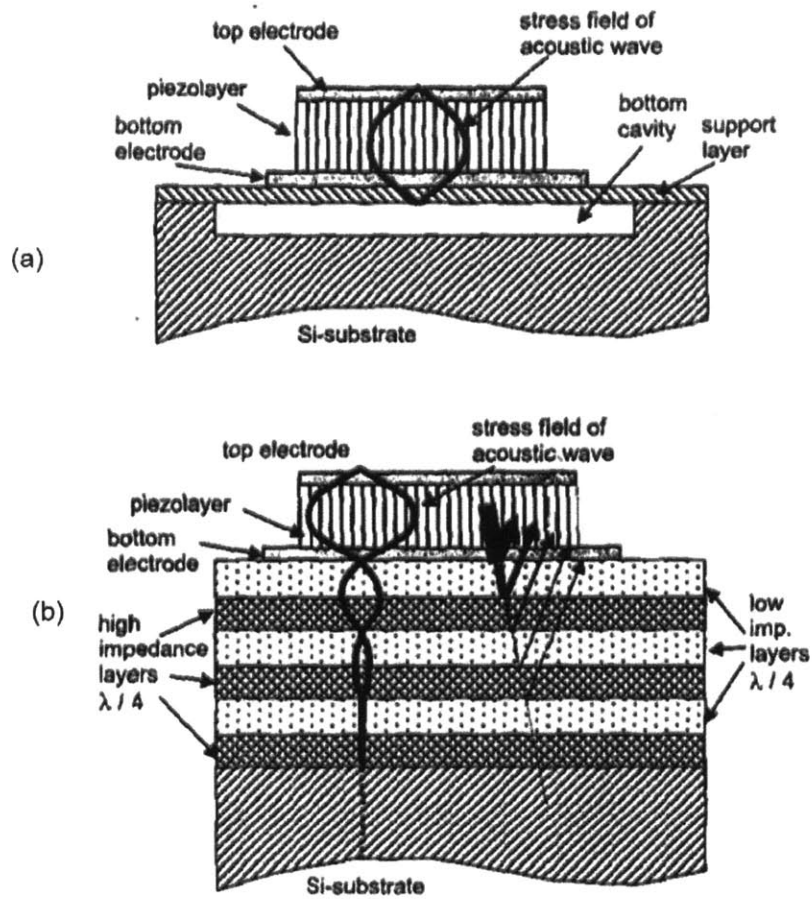


Figure 1-4: Two commonly encountered Bulk Acoustic Wave (BAW) devices as introduced in [2].

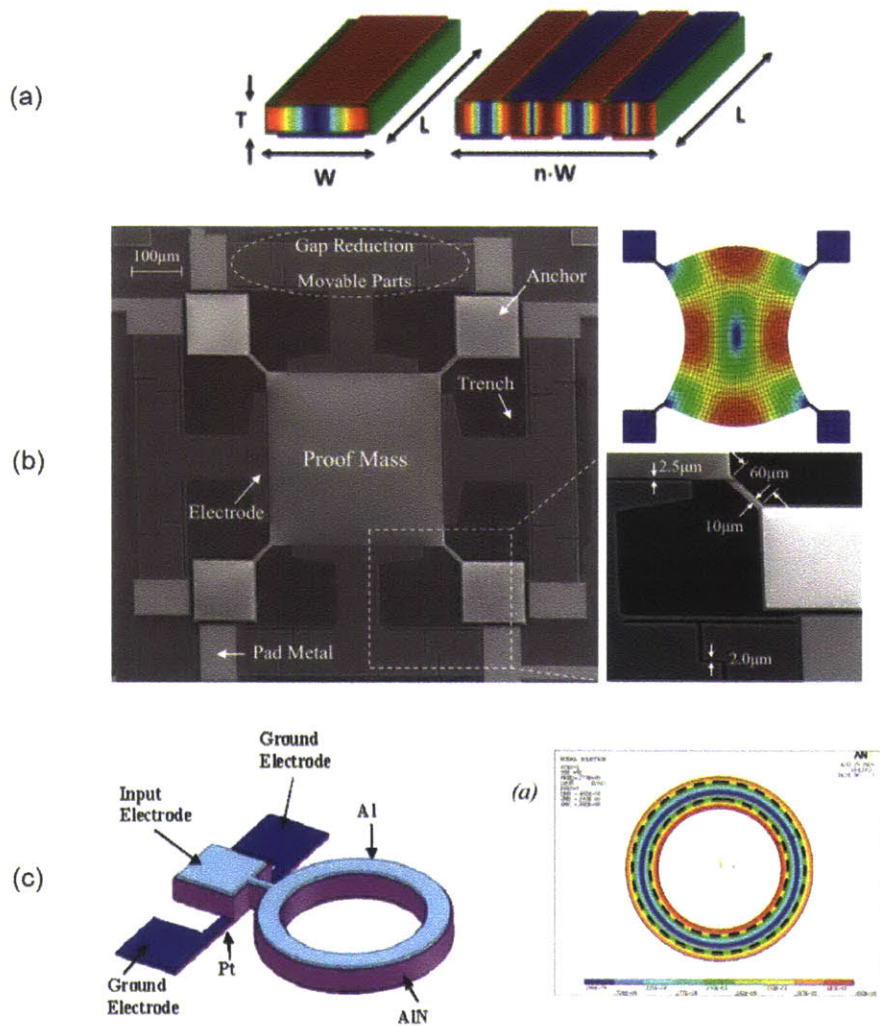


Figure 1-5: Examples of various contour mode MEMS resonators: (a) Longitudinal bar (Lamb-wave) [3], (b) Lame mode [4], and (c) ring-extensional mode [5].

temperature stability than the SAW devices. One commonly encountered type of BAW device is the Film Bulk Acoustic Resonator (FBAR), which consists of a thin suspended membrane, usually made of a piezoelectric material (Figure 1-4 (a)). In this case, the resonant dimension is the thickness of the film. The most popular material for FBAR is wurtzite Aluminum Nitride (AlN). Another BAW type of device is the Solidly Mounted Resonator (SMR), where the acoustic cavity is defined by a series of alternating layers that form Bragg mirrors, as shown in Figure 1-4 (b). In this case, the resonance frequency is also set by the thicknesses of the constituent layers. These technologies are heavily used for filtering in the cellular market. However, as the trends progress more towards smart, reconfigurable systems, we need ways of integrating multiple resonant frequencies on the same chip. BAW devices have their resonant frequency set by the thickness of the film, which limits the frequency range of operation for filters fabricated on the same substrate.

1.2.4 Contour Mode MEMS Resonators

To address the need for multiple frequencies on the same chip, researchers have started looking into alternate vibration modes. While we still want to take advantage of stiffer and higher quality bulk modes, we can now realize standing waves in the lateral or in-plane dimension of a suspended bar or cavity. These are known as contour mode resonators. The main benefit of these devices is that for a given film thickness, we can realize multiple frequencies on the same chip, via a single photolithographic step that patterns the lateral dimension of the cavity. Additionally, these resonators have small footprints ($\approx 10 - 100 \mu m^2$). Various research groups have explored contour mode resonators, both in silicon, using electrostatic transduction, and in piezoelectric materials such as AlN. Modes that satisfy the contour mode requirement range from simple longitudinal waves in a bar, to plate modes and extension of rings or disks, as shown in Figure 1-5. For example, in polysilicon, 6.2 GHz contour modes were measured in a longitudinal bar using solid-state electrostatic transduction [25]. In AlN, contour mode resonators were used realize closed-loop oscillators with frequencies as high as 3.5 GHz [3].

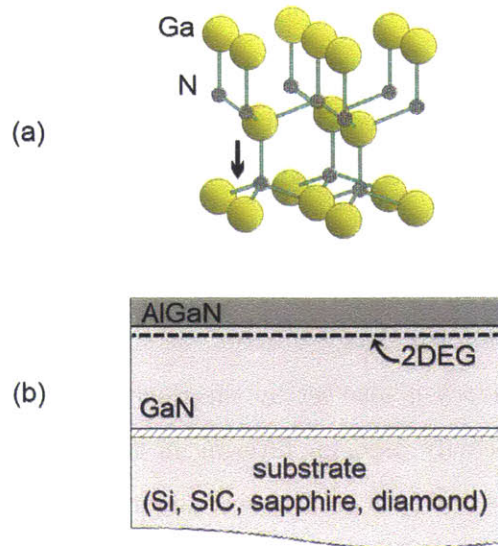


Figure 1-6: (a) Wurtzite crystal structure of GaN. (b) AlGaN/GaN heterostructure can be grown on a variety of substrates, including Si-111, SiC, diamond, and sapphire.

1.3 Gallium Nitride MEMS Resonators

1.3.1 GaN technology

Over the past two decades, Gallium Nitride technology has matured considerably, rendering it as the second most popular semiconductor after silicon due to a series of extraordinary properties.

As a wide bandgap semiconductor (3.4 eV), GaN is intensively used for solid-state lightning [26]. This high performance culminated in the 2014 Nobel Prize in Physics which was awarded jointly to Isamu Akasaki, Hiroshi Amano and Shuji Nakamura for the invention of GaN-based blue-diodes.

Additionally, the AlGaN/GaN heterostructure provides an inherent high charge density ($1 \times 10^{13} \text{ cm}^{-2}$), 2D electron gas (2DEG) as shown in Figure 1-6 (b). Contrary to other semiconductor-based 2DEG systems, such as gallium arsenide heterostructures, the sheet of charge in GaN is generated without the need for intentional doping, which leads to unprecedented electron velocities and mobilities, making it ideal for high frequency (>300 GHz) integrated circuits. As a result, GaN heterostructures have been increasingly used for Monolithic Microwave IC's (MMICs). Another im-

Table 1.1: Material properties of commonly encountered electromechanical materials.

Material	Elastic coefficient (GPa)	Acoustic velocity (m/s)	Piezoelectric coefficient (Cm^{-2})	$f \times Q$ (s^{-1})	k_{eff}^2 (%)	ref
<i>Si</i>	165	8415	<i>N/A</i>	2.5×10^{13}	<i>N/A</i>	[27]
<i>SiC</i>	605	13100	+0.2	3.5×10^{14}	0.08	[27], [28]
<i>GaAs</i>	118	2470	-0.16	<i>not measured</i>	0.04	[29]
<i>LiNbO₃</i>	60	3900	+3.65	7.7×10^{11}	16	[30]
<i>AlN</i>	390	11000	+1.55	1×10^{13}	5.6	[27]
<i>GaN</i>	398	8084	+0.65	2.5×10^{13}	2	[28], [27]

portant property of GaN is its high breakdown field, which makes it ideal for high power ($>10W/mm$) applications.

In addition to the extraordinary optoelectronic and RF performance, GaN also exhibits excellent electromechanical properties, such as high piezoelectric coefficients (electromechanical coupling k_T^2 up to 2% in FBARs), high acoustic velocities and low acoustic losses. Table 1.1 shows a comparison between some of the most relevant material properties for electromechanical applications of GaN with other commonly encountered materials. It can be seen that GaN has an acoustic velocity comparable to silicon as well as similar acoustic losses. GaN also has piezoelectric coefficients higher than GaAs and SiC. All of these qualities make it ideal for MEMS applications. Moreover, there have been many developments in the growth of GaN on various substrates, such as silicon carbide, sapphire and diamond [31]. Recently, researchers were able to grow high quality GaN on Si-(111), which has the potential of not only lowering the cost of GaN wafers, but also of opening the market for new applications, such as the heterogenous integration of GaN MMICs with silicon CMOS circuits [32]. For MEMS devices, the use of silicon substrates as sacrificial layers enables suspended GaN cantilevers and membranes [33], leading to a wide spectrum of applications, such as filters, clocks and sensors.

The most important element that distinguishes GaN from other piezoelectric ma-

materials is the ability to fabricate MEMS resonators integrated with the high gain electronics offered by this technology. This provides a direct way of extracting the electromechanical current and interfacing with the external world. Besides, the presence of the inherent 2DEG gives rise to new physics and transduction mechanisms that open many possibilities for reconfigurable systems and novel sensors. This is the major strength of this technology, and the main object of study of this thesis.

1.4 Thesis Contribution

Despite the increased use of GaN for high-frequency, high-power applications, the potential for harnessing its electromechanical properties for wireless communications has received very little attention so far. This thesis describes experimental procedures developed for realizing high-performance piezoelectric GaN MEMS resonators, integrated in a GaN MMIC process with only two modifications to the standard flow.

Withing this platform, we are able to study the transduction capabilities of the epitaxial structure, and we demonstrate ground-breaking performance in terms of mechanical quality factor of the resonance, as we achieve the highest $f \cdot Q$ products measured in GaN to date, as enabled by fabrication in a Au-free process.

Additionally, we demonstrate the first solid-state, switchable piezoelectric resonator, using the conductive 2D electron has as an electrode for transduction.

Finally, we show devices with record-breaking Signal-to-Noise ratio, by using active transistor sensing of the mechanical vibrations.

1.5 Thesis Outline

This dissertation spans 7 chapters. Chapter 1 portrays the need for MEMS resonators for timing and filter applications in wireless communications, highlighting the benefits of a GaN-MEMS platform.

In Chapter 2, the physics and modeling of MEMS resonators is presented, with and emphasis on piezoelectric transduction mechanisms.

Next, fabrication techniques used for realizing GaN MEMS in a HEMT-compatible process are presented in Chapter 3.

In Chapter 4 we highlight the unique transduction mechanisms enabled by the presence of the 2DEG, including the first switchable piezoelectric resonator, and a completely metal-free GaN resonator, useful for directly interrogating the material properties of the stack in the absence of electrode mass loading and damping.

Chapter 5 focuses on the optimization of contour mode resonators in a MMIC technology, with as little modification to the standard process as possible.

Chapter 6 discusses the benefits of using active HEMT sensing for detecting the mechanical vibrations.

In Chapter 7 we conclude and discuss future directions enabled by the platform developed here.

This thesis also contains two appendices. Appendix A contains information about the material properties of the GaN epitaxial structure, as well as other materials deposited during fabrication. Finally, Appendix B lists detailed fabrication procedures.

Chapter 2

Theory and Modelling of Piezoelectric MEMS Resonators

2.1 Resonance and the Harmonic Oscillator

The first step when talking about any type of resonator, MEMS resonators included, is an understanding of harmonic motion and resonance. This relatively elementary physics problem lies at the foundation of many studies and applications, ranging from filters and frequency sources in wireless communications [34, 35] to gravitational-wave detectors [36], ultra-precise clocking standards [37] and verification of quantum equivalence principles.

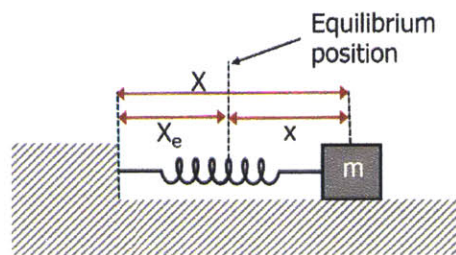


Figure 2-1: A model of the simple harmonic oscillator.

2.1.1 Simple Harmonic Oscillator

We start by considering a particle executing a periodic motion, in the absence of any forces. A simple representation of this case is a mass attached to a rigid wall by a spring, as shown in Figure 2-1. Following the derivation of Goldstein [38], we assume a conservative system, where the potential does not depend on any time derivatives of the position coordinate:

$$V = V(X). \quad (2.1)$$

This assumption is valid in most of the systems considered here. Then we can Taylor expand the potential about the equilibrium position, $X = X_e$:

$$V = V_0 + \left(\frac{\partial V}{\partial X}\right)_{X_e} (X - X_e) + \frac{1}{2} \left(\frac{\partial^2 V}{\partial X^2}\right)_{X_e} (X - X_e)^2 + \dots \quad (2.2)$$

At equilibrium, the sum of forces acting on the system must vanish, leaving the first derivative equal to zero. By setting the arbitrary potential level V_0 to zero and we ignore the higher order terms, as we are interested in situations with small displacements from equilibrium. The potential then becomes:

$$V = \frac{1}{2} \left(\frac{\partial^2 V}{\partial X^2}\right)_{X_e} x^2 = \frac{1}{2} kx^2. \quad (2.3)$$

The kinetic energy of the system can also be expanded in an equivalent Taylor series, and it can be shown [38], that for conservative systems, the kinetic energy is given by:

$$T = \frac{1}{2} m\dot{x}^2. \quad (2.4)$$

As a result, we can now write the Lagrangian:

$$L = T - V = \frac{1}{2} m\dot{x}^2 - \frac{1}{2} kx^2, \quad (2.5)$$

and, by using Lagrange's equations:

$$\frac{d}{dt} \left(\frac{\partial L}{\partial \dot{x}}\right) - \left(\frac{\partial L}{\partial x}\right) = 0, \quad (2.6)$$

we obtain the equation of motion:

$$m\ddot{x} + kx = 0, \quad (2.7)$$

which is the familiar equation describing the motion of a mass on a spring.

As expected, one solution to this differential equation is:

$$x(t) = x_0 \sin(\omega_0 t + \phi_0) \quad (2.8)$$

$$\omega_0 = \sqrt{\frac{k}{m}}, \quad (2.9)$$

where x_0 , ω_0 , and ϕ_0 are the amplitude, angular frequency and phase of the system.

2.1.2 Damped Harmonic Oscillator

In reality, all practical systems exhibit some degree of loss. To model this, we can consider an additional viscous force acting on the mass in Figure 2-1 [39]. For simplicity, we assume a linear drag force that is proportional to the velocity. Then the equation of motion becomes:

$$m\ddot{x} + c\dot{x} + kx = 0. \quad (2.10)$$

The damping factor or dissipation rate γ is defined as [40]:

$$\gamma = \frac{c}{2m}. \quad (2.11)$$

One solution to this differential equation is given by:

$$x(t) = x_1 e^{-(\gamma-q)t} + x_2 e^{-(\gamma+q)t}, \quad (2.12)$$

where

$$q = \sqrt{\gamma^2 - \omega_0^2}. \quad (2.13)$$

Depending on the relative size of the dissipation rate compared to the natural fre-

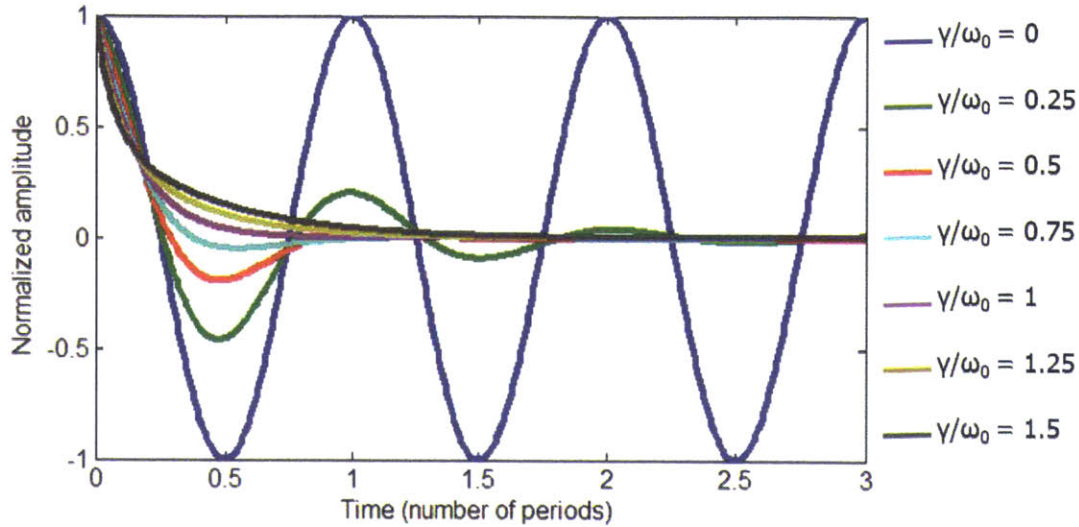


Figure 2-2: Normalized amplitude of the damped harmonic oscillator for different values of the dissipation rate.

quency of the system, there are three regimes:

1. q real > 0 : Overdamping

In this case, both exponents in Equation 2.12 are real, leading to an exponential decay of the displacement. Then a mass that is given an initial displacement and released return to its initial position without oscillating as a result of damping.

2. q real $= 0$: Critical damping

The solution reduces to a single exponential factor, as the two amplitude coefficients are not independent anymore. Similar to the first case, a mass displaced in these conditions will return to equilibrium without having the chance to oscillate.

3. q imaginary: Underdamping

In this situation, the factor q becomes imaginary, so the resulting motion is periodic with decaying amplitude. The displaced mass will oscillate for a few periods and then come to a stop. It can be shown that the solution to this case becomes:

$$x(t) = e^{-\gamma t}(A \cos(\omega_d t + \phi_0)), \quad (2.14)$$

where the damped angular frequency is given by

$$\omega_d = \sqrt{\gamma^2 - \omega_0^2}. \quad (2.15)$$

Figure 2-2 shows a plot of these different cases. The undamped simple harmonic oscillator case corresponds to the $\gamma = 0$ case. In practice, the resonators considered in this thesis satisfy the underdamped condition described above.

In all the cases above, the total energy stored in the system at a time t is given by the sum of the kinetic and potential energy. Then, for the case of the underdamped oscillator, this becomes:

$$E(t) = \frac{1}{2}mA^2\omega_0^2e^{-t/\tau}. \quad (2.16)$$

Here, τ is the relaxation time defined by

$$\tau = \frac{1}{2\gamma}. \quad (2.17)$$

As expected, the energy stored in the oscillator decays exponentially with the time constant τ . Given the loss mechanism in this system, the rate of change of total energy in the system is given by:

$$\frac{dE}{dt} = m\ddot{x}\dot{x} + kx\dot{x} = -c\dot{x}^2. \quad (2.18)$$

We can now introduce define the quality factor of the damped oscillator, as the energy stored in the system divided by the energy dissipated per cycle:

$$Q = 2\pi \frac{E_{stored}}{E_{dissipated}}. \quad (2.19)$$

By substituting Equation 2.14 into Equation 2.18 and integrating the energy dissipation rate over one period T , we can show that the energy dissipated during one cycle is

$$\Delta E = \left(\frac{1}{2}mA^2\omega_0^2e^{-t/\tau} \right) \frac{T}{\tau}. \quad (2.20)$$

We finally obtain an expression for the quality factor of the underdamped harmonic oscillator:

$$Q = \omega_d \tau = \frac{\omega_d}{2\gamma}. \quad (2.21)$$

2.1.3 Driven, Damped Harmonic Oscillator: Resonance

The last element of theory needed to describe a resonator is including a periodic driving force and analyzing the response of the system as a function of the drive frequency. In this situation, the equation of motion becomes:

$$m\ddot{x} + c\dot{x} + kx = F_0 \cos(\omega t). \quad (2.22)$$

The resulting motion is a superposition of a transient solution at the natural frequency that decays with a time constant τ as described in 2.1.2, and a forced oscillation at the driving frequency, ω . This latter case is the steady-state solution and is given by:

$$x(t) = Ae^{i(\omega t - \phi)}. \quad (2.23)$$

The amplitude, A , and phase ϕ are defined as

$$A(\omega) = \frac{F_0/m}{[(\omega_0^2 - \omega^2)^2 + 4\gamma^2\omega^2]} \quad (2.24)$$

and

$$\tan\phi = \frac{2\gamma\omega}{\omega_0^2 - \omega^2}, \quad (2.25)$$

respectively. When the forcing frequency approaches the natural frequency of the system, the amplitude of oscillations reaches a maximum, which is known as the resonance condition. In a damped, driven system, the resonance frequency is not exactly equal to the natural frequency. Instead, it can be found by differentiating the amplitude with respect to angular frequency and setting the result to zero:

$$\omega_r^2 = \omega_d^2 - \gamma^2. \quad (2.26)$$

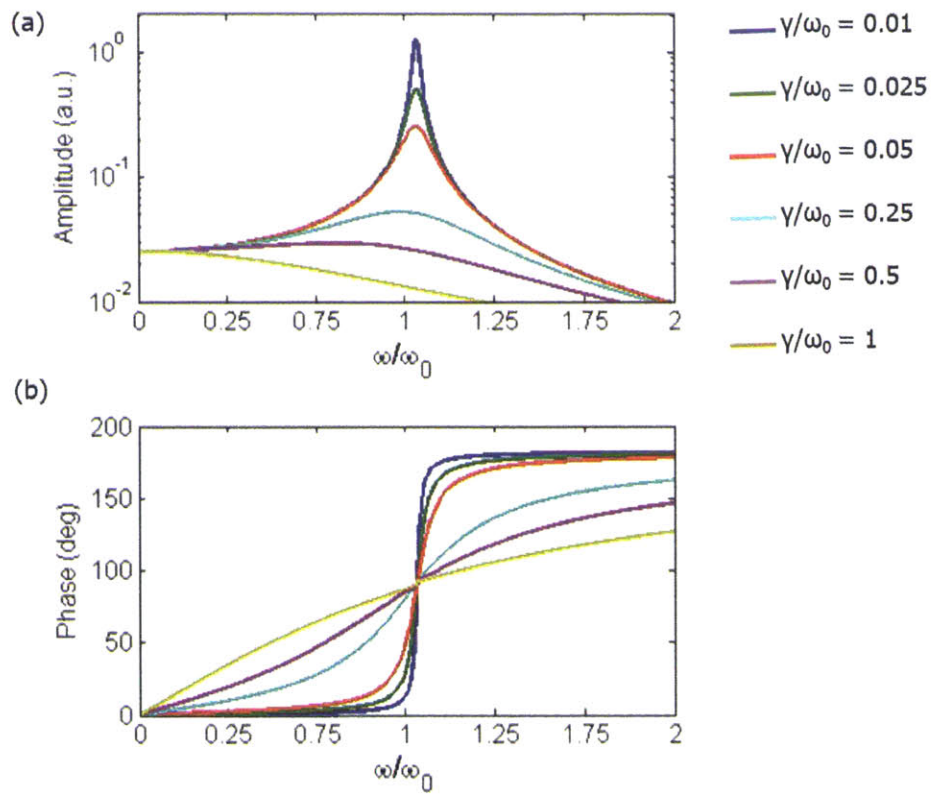


Figure 2-3: Amplitude (a) and phase (b) of the driven, damped harmonic oscillator for different values of the dissipation rate.

Only in the case when the damping factor γ approaches zero, the natural frequency, damped frequency and resonance frequency are all equal. Figure 2-3 shows calculated amplitude and phase for a driven harmonic oscillator, for different values of the dissipation rate γ . When the dissipation is small, the response is a sharp peak, and it's accompanied by a phase shift of 180° . The physical cause of this phase shift can be understood by considering two limiting cases when referring to the simple representation of a mass on a spring that is now forced at ω . In the low frequency limit, when $\omega < \omega_0$, we expect the inertia of the mass to be quite small, and mainly be dominated by the stiffness of the spring which is moving slowly and in phase with the driving motion. For the $\omega > \omega_0$ case, the spring looks less stiff, with the mass now moving faster and out of phase with the driving force. In this case the inertia of the mass dominates. A similar behavior can be seen in electrical LC oscillators, and the equivalence between the spring-mass and LC systems is further discussed in 2.4.

As the damping is increased, the peak broadens and the phase shift becomes less pronounced. When $\gamma > \omega_0/\sqrt{2}$, no amplitude resonance occurs. The quality factor introduced in the previous section is measure of the sharpness of the resonant response. For weak damping only, 2γ is approximately equal to the Full Width at Half Maximum of the resonance, $\Delta\omega$, and Q becomes:

$$Q = \frac{\omega_0}{2\gamma} = \frac{\omega_0}{\Delta\omega}. \quad (2.27)$$

2.2 Constitutive Relations for Waves Propagating in Elastic Media

We now want to look at a more specific case of harmonic oscillators, acoustic resonators, so we need to define the main quantities of interest in elastic theory, and the constitutive relations that connect them. The purpose of this section is a brief introduction of the main laws and notations. For more in depth proofs and derivations one could refer to the the suggested in the text.

2.2.1 Deformation and Strain

We start by defining the strain in the case of small displacements as [41]:

$$S_{ij}(\mathbf{r}, t) = \frac{1}{2} \left(\frac{\partial u_i(\mathbf{r}, t)}{\partial r_j} + \frac{\partial u_j(\mathbf{r}, t)}{\partial r_i} \right), \quad (2.28)$$

where \mathbf{r} is the position vector given by:

$$\mathbf{r} = \hat{\mathbf{x}}x + \hat{\mathbf{y}}y + \hat{\mathbf{z}}z. \quad (2.29)$$

To simplify the solutions to problems in acoustics, we introduce a reduced definition of the strain, based on the fact that most of the cases of interest are symmetric. This symmetry implies that each component of the strain can be specified by one subscript instead of two. So we define the following mapping:

$$\mathbf{S} = \begin{bmatrix} S_{xx} & S_{xy} & S_{xz} \\ S_{yx} & S_{yy} & S_{yz} \\ S_{zx} & S_{zy} & S_{zz} \end{bmatrix} = \begin{bmatrix} S_1 & \frac{1}{2}S_6 & \frac{1}{2}S_5 \\ \frac{1}{2}S_6 & S_2 & \frac{1}{2}S_4 \\ \frac{1}{2}S_5 & \frac{1}{2}S_4 & S_3 \end{bmatrix}. \quad (2.30)$$

The cyclical order of indexes used here follows the Voigt notation, which is standard for problems in acoustics, especially when considering additional phenomena, such as piezoelectricity [42]. In this case we obtain a simplified six-element column matrix strain which will be used in the rest of this thesis:

$$\mathbf{S} = \begin{bmatrix} S_1 \\ S_2 \\ S_3 \\ S_4 \\ S_5 \\ S_6 \end{bmatrix}. \quad (2.31)$$

The first three components of the strain are called normal strains, while the last three are called shear strains.

2.2.2 Stress and the Equation of Motion

Stress is defined as a force acting between particles inside an acoustic medium. When the stress is symmetric, the same abbreviated notation as in Subsection 2.2.1 can be used to simplify the stress matrix. However, for reasons that become obvious in later derivations, the factor of $\frac{1}{2}$ gets dropped from the definition of stress:

$$\mathbf{T} = \begin{bmatrix} T_{xx} & T_{xy} & T_{xz} \\ T_{yx} & T_{yy} & T_{yz} \\ T_{zx} & T_{zy} & T_{zz} \end{bmatrix} = \begin{bmatrix} T_1 & T_6 & T_5 \\ T_6 & T_2 & T_4 \\ T_5 & T_4 & T_3 \end{bmatrix}. \quad (2.32)$$

For the rest of this thesis, the stress matrix will be given by:

$$\mathbf{T} = \begin{bmatrix} T_1 \\ T_2 \\ T_3 \\ T_4 \\ T_5 \\ T_6 \end{bmatrix}. \quad (2.33)$$

In the presence of an applied traction force at the boundary of the medium Newton's Law states that

$$\int_{\delta S} \mathbf{T} \cdot \hat{\mathbf{n}} dS + \int_{\delta V} \mathbf{F} dV = \int_{\delta V} \rho \frac{\partial^2 \mathbf{u}}{\partial t^2} dV. \quad (2.34)$$

In the limit of $\delta V \rightarrow 0$, this can be simplified using the Divergence Theorem to:

$$\nabla \cdot \mathbf{T} = \rho \frac{\partial^2 \mathbf{u}}{\partial t^2}. \quad (2.35)$$

It is important to mention that in the case of symmetry, the divergence operator can

also be simplified using the abbreviated form

$$\nabla \cdot = \begin{bmatrix} \frac{\partial}{\partial x} & 0 & 0 & 0 & \frac{\partial}{\partial z} & \frac{\partial}{\partial y} \\ 0 & \frac{\partial}{\partial y} & 0 & \frac{\partial}{\partial z} & 0 & \frac{\partial}{\partial x} \\ 0 & 0 & \frac{\partial}{\partial z} & \frac{\partial}{\partial y} & \frac{\partial}{\partial x} & 0 \end{bmatrix}. \quad (2.36)$$

2.2.3 Constitutive Relations: Hooke's Law

Next, we want to relate the elastic forces acting on particles inside an elastic medium to the induced displacements. In the case of small displacements and strains, we expect this to satisfy Hooke's law, which is an experimentally verified linear relationship between the elastic restoring force acting on a spring, and the resulting displacement. In the case of acoustics, the equivalent "spring constant" will have a matrix form. This is known as the stiffness matrix and is defined by:

$$\begin{aligned} T_{ij} &= c_{ijkl} S_{kl}, \\ i, j, k, l &= x, y, z. \end{aligned} \quad (2.37)$$

Alternatively, this relationship can be expressed as:

$$\begin{aligned} S_{ij} &= s_{ijkl} T_{kl}, \\ i, j, k, l &= x, y, z, \end{aligned} \quad (2.38)$$

where s_{ijkl} is known as the compliance matrix.

Going back to the assumption of symmetry, it can be shown that

$$c_{ijkl} = c_{jikl} = c_{ijlk} = c_{jilk}, \quad (2.39)$$

which allows us to reduce the stiffness matrix to a 6 by 6 matrix. We can then write the constitutive relations as:

$$\mathbf{T} = \mathbf{c} : \mathbf{S} \quad (2.40)$$

and

$$\mathbf{S} = \mathbf{s} : \mathbf{T}. \quad (2.41)$$

Here, the Stress and Strain tensors are in the one-column matrix introduced above.

In reality, each crystal symmetry will impose further conditions, leading to even more simplifications of the elastic matrix. For example two of the most commonly encountered crystal symmetries are the cubic and hexagonal groups. The cubic one includes zinc-blende solids, such as silicon or Gallium Arsenide, while the hexagonal one is found in wurtzite crystals such as Gallium Nitride and Aluminum Nitride. The elastic matrix corresponding to these classes of symmetry are given by [41]

$$C_{cubic} = \begin{bmatrix} c_{11} & c_{12} & c_{12} & 0 & 0 & 0 \\ c_{12} & c_{11} & c_{12} & 0 & 0 & 0 \\ c_{12} & c_{12} & c_{11} & 0 & 0 & 0 \\ 0 & 0 & 0 & c_{44} & 0 & 0 \\ 0 & 0 & 0 & 0 & c_{44} & 0 \\ 0 & 0 & 0 & 0 & 0 & c_{44} \end{bmatrix}, \quad (2.42)$$

and

$$C_{hexagonal} = \begin{bmatrix} c_{11} & c_{12} & c_{13} & 0 & 0 & 0 \\ c_{12} & c_{11} & c_{13} & 0 & 0 & 0 \\ c_{13} & c_{13} & c_{33} & 0 & 0 & 0 \\ 0 & 0 & 0 & c_{44} & 0 & 0 \\ 0 & 0 & 0 & 0 & c_{44} & 0 \\ 0 & 0 & 0 & 0 & 0 & c_{66} \end{bmatrix}, \quad (2.43)$$

respectively. In the case of the hexagonal structure, the last elastic constant is not an independent parameter, but rather given by $(c_{11} - c_{12})/2$.

2.2.4 Wave equation

For problems involving wave propagation in solids, it is useful to manipulate the field equations in symbolic form and obtain a wave equation that can be then solved. This

approach is equivalent to the treatment of electromagnetic waves.

In the case of acoustics, the field equations are given by:

$$\nabla \cdot \mathbf{T} = \rho \frac{\partial \mathbf{v}}{\partial t} - \mathbf{F} \quad (2.44)$$

$$\nabla_s \mathbf{v} = \mathbf{s} : \frac{\partial \mathbf{T}}{\partial t}, \quad (2.45)$$

where F is an applied external force, and

$$\nabla_s = \begin{bmatrix} \frac{\partial}{\partial x} & 0 & 0 \\ 0 & \frac{\partial}{\partial y} & 0 \\ 0 & 0 & \frac{\partial}{\partial z} \\ 0 & \frac{\partial}{\partial z} & \frac{\partial}{\partial y} \\ \frac{\partial}{\partial z} & 0 & \frac{\partial}{\partial x} \\ \frac{\partial}{\partial y} & \frac{\partial}{\partial x} & 0 \end{bmatrix}. \quad (2.46)$$

We can now differentiate Equation 2.45 with respect to time and operate with $c\nabla \cdot$ on Equation 2.45. By eliminating the stress tensor, we now arrive to the Wave Equation:

$$\nabla \cdot (c : \nabla_s \mathbf{v}) = \rho \frac{\partial^2 \mathbf{v}}{\partial t^2} - \frac{\partial \mathbf{F}}{\partial t}. \quad (2.47)$$

We next consider the case of a uniform plane wave propagating in a source-free region, with $F = 0$. The direction of propagation is given by the vector

$$\hat{\mathbf{l}} = \hat{x}l_x + \hat{y}l_y + \hat{z}l_z. \quad (2.48)$$

The solution to the wave equation will then be proportional to $e^{i(\omega t - k\hat{\mathbf{l}} \cdot \mathbf{r})}$ and the wave equation reduces to

$$[k^2 \Gamma_{ij} - \rho \omega^2 \delta_{ij}] [v_{ij}] = 0, \quad (2.49)$$

where Γ_{ij} is the Christoffel matrix, given by

$$\Gamma_{ij} = l_{iK} c_{KLL} l_{Lj}. \quad (2.50)$$

The matrices l_{iK} and l_{Lj} are given by

$$l_{iK} = \begin{bmatrix} l_x & 0 & 0 & 0 & l_z & l_y \\ 0 & l_y & 0 & l_z & 0 & l_x \\ 0 & 0 & l_z & l_y & l_x & 0 \end{bmatrix}, \quad (2.51)$$

and

$$l_{Lj} = \begin{bmatrix} l_x & 0 & 0 \\ 0 & l_y & 0 \\ 0 & 0 & l_z \\ 0 & l_z & l_y \\ l_z & 0 & l_x \\ l_y & l_x & 0 \end{bmatrix}, \quad (2.52)$$

respectively.

To find the dispersion relation we can then set the characteristic determinant equal to zero:

$$\Omega(\omega, k_x, k_y, k_z) = |k^2 \Gamma_{ij}(l_x, l_y, l_z) - \rho \omega^2 \delta_{ij}| = 0. \quad (2.53)$$

2.2.5 Lamb Mode Resonators

One family of acoustic waves that we focus on significantly in this thesis is the symmetric branch of Lamb modes, since their frequency depends mainly on the in-plane dimension of the cavity. Additionally, the phase velocities of these modes in standard semiconductor films such as Si, GaAs, GaN, AlN are high with moderate coupling coefficients (up to 2.5 %), which leads to low motional impedance resonators. This implies that low insertion loss resonators, spanning multiple frequencies can be realized on the same chip simultaneously, which has high value for both studying various physical phenomena and for realizing reconfigurable, cognitive RF systems. In this thesis we demonstrate multiple Lamb-mode resonators, with frequencies ranging from 500 MHz to 2 GHz, achieving quality factors higher than 8000 at 2 GHz.

The theory behind these modes was first developed by Horace Lamb in 1917, to describe the propagation of guided waves in thin plates [43]. Figure 2-4 (a) shows the original setup of the problem, where a plate of thickness $2d$ is considered infinite in both in-plane directions. The system of coordinates is then chosen with the origin on the median plane of the plate. Assuming a wave propagating in the x direction, we are interested in solutions with no displacement in the y direction. Then we can assume periodic solutions to the wave equation (Equation 2.49) of the form:

$$u = u_0 f_x(z) e^{i(\omega t - k_x x)} \quad (2.54)$$

$$w = w_0 f_z(z) e^{i(\omega t - k_x x)} \quad (2.55)$$

In the case of guided waves through a plate with free top and bottom surfaces all stresses the appropriate boundary conditions become:

$$T_{zz} = 0, \quad (2.56)$$

$$T_{xz} = 0. \quad (2.57)$$

These boundary conditions will give rise to two characteristic equations:

$$\frac{\tan(\beta d)}{\tan(\alpha d)} = -\frac{4\alpha\beta k^2}{(k^2 - \beta^2)^2}, \quad (2.58)$$

$$\frac{\tan(\beta d)}{\tan(\alpha d)} = -\frac{4\alpha\beta k^2}{k^2 - \beta^2)^2}. \quad (2.59)$$

Here α and β are given by

$$\alpha^2 = \frac{\omega^2}{v_l^2} - k^2, \quad (2.60)$$

$$\beta^2 = \frac{\omega^2}{v_s^2} - k^2, \quad (2.61)$$

where v_l and v_s are the longitudinal and shear velocities, respectively.

The first set of solutions corresponds to waves whose displacements symmetric with respect to the $z = 0$ plane, while the second one will generate antisymmetric

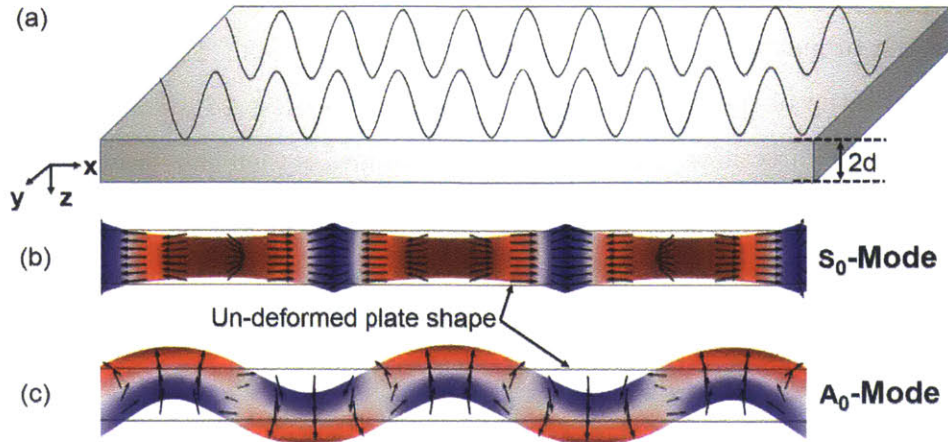


Figure 2-4: (a) Guided waves are propagating in an infinite plate of thickness $2d$ in the x -direction. The system of coordinates is placed with the center on the median plane of the plate. (b) Cross-section of infinite plane shows the zeroth order symmetric Lamb mode (S_0) propagating in the x -direction, for a normalized wavelength $\lambda/2d = 4.3$. In (c), the mode shape of the zeroth order antisymmetric mode (A_0) is shown for a normalized wavelength $\lambda/2d = 6$. In both cases, the superimposed arrows represent the displacement fields, while the color maps the strain fields.

displacement fields. The first symmetric solution, S_0 is illustrated in Figure 2-4 (b). The color maps the strain fields, while the arrows represent the displacement field. Similarly, the first antisymmetric mode, A_0 is shown in Figure 2-4 (c).

2.3 Transduction Mechanisms

Having discussed some of the most important equations describing acoustics in solids, the next step is to look at ways in which energy can be transferred between the electrical and mechanical domains, which is known as transduction in the field of MEMS. Some of the most typical transduction mechanisms used in MEMS are illustrated in Figure 2-5, with an emphasis on techniques that are compatible with major semiconductor baseline processes, such as CMOS or III-V MMICs. Note that the field of MEMS can include other domains besides electrical and mechanical, such as thermal, fluidic, etc.

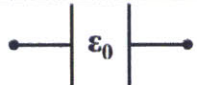
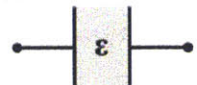




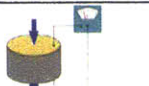
	Drive	Sense	
Capacitive – air gap	✓	✓	
Capacitive – solid dielectric	✓	✓	
Capacitive – solid-state	✓	✓	
Thermal	✓	x	
Piezoresistive	x	✓	
Transistor	x	✓	
Piezoelectric	✓	✓	

Figure 2-5: Common types of transduction mechanisms that are compatible with major semiconductor technologies.

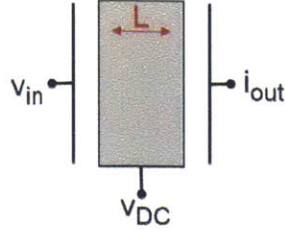


Figure 2-6: Electrostatic transduction of a longitudinal resonant bar (top-view) using two air-gap capacitors.

2.3.1 Capacitive Transduction

Capacitive transduction is one of the most commonly used mechanisms for resonant and non-resonant MEMS. This mechanism uses an electrostatic force to convert an electrical signal into mechanical vibrations. Conversely, mechanical strain will be sensed as a change in capacitance due to the physical change in the distance between the two plates, which is what gives it its name. As shown in Figure 2-5, this capacitor can be defined either between two plates separated by an air-gap, or in a solid-state case, where air is not replaced by a dielectric. There are multiple applications of this method, especially in the realm of sensors [44].

Consider the simple bar resonator illustrated in Figure 2-6. We use two air-gap capacitors to drive and sense vibrations in this structure. We apply a DC bias to the body of the resonator, and a driving AC voltage to the left transducer. Then we can calculate the resulting drive force by

$$F_{cap} = \frac{dU_{cap}}{dx}, \quad (2.62)$$

where U_{cap} is the energy stored in the capacitor and is equal to $\frac{1}{2}CV^2$. Then the driving force becomes

$$\begin{aligned} F_{cap} &= \frac{1}{2}V^2 \frac{\partial C}{\partial x}, \\ &= \frac{1}{2} (V_{DC} + v_{in}e^{i\omega t}) \frac{\partial}{\partial x} \left(\frac{\epsilon_0 A_{cap}}{g+x} \right). \end{aligned} \quad (2.63)$$

Here, A_{cap} is the area of the capacitor plate, g is the initial width of the gap, and x is the change in distance between the two plates. For small displacements we can expand the above expression about the equilibrium gap value, obtaining:

$$F_{cap} \approx \frac{\epsilon_0 A_{cap}}{g^2} (V_{DC}^2 + 2V_{DC}v_{in}e^{i\omega t} + v_{in}^2 e^{i2\omega t}). \quad (2.64)$$

We immediately note that the first term does not contribute to a frequency dependent term, and the last term becomes negligible compared to the second one, when $v_{in} < v_{DC}$. As a result, the relevant component of the drive force at frequency ω becomes:

$$F_{cap,\omega} = \frac{2V_{DC}v_{in}\epsilon_0 A_{cap}}{g^2}. \quad (2.65)$$

One can already notice that this transduction mechanism is intrinsically nonlinear, which could lead to limiting situations such as gap closing of the transducers [45].

2.3.2 Piezoelectric Transduction

An alternative to the electrostatic transduction is to use the piezoelectric effect to transfer energy from the electrical to the mechanical domain. As we will see later, this is a more efficient transduction mechanisms than the capacitive one. Moreover, piezoelectricity is a linear effect, as opposed to the capacitive case. Discovered in 1880 by the Curie brothers, the piezoelectric effect has enabled many applications, ranging from quartz clocks [22], surface acoustic wave filters for radio communications [24], to sensors and actuators [46] as well as energy harvesters [47].

The direct piezoelectric effect consists in the appearance of bound electrical charges at the surfaces of a strained medium. This induced charge depends linearly on the applied strain, so it will change sign if this is reversed. Additionally, an applied electric field across a piezoelectric material will lead to deformation, which is known as the converse piezoelectric effect.

Piezoelectric Constitutive Relations

To account for this linear relationship between strain and charge, the constitutive relations introduced in Subsection 2.2.3 must be modified to include an additional term. Moreover, in the case of a piezoelectric material, the electrical displacement field must also contain a stress-dependent term. The piezoelectric constitutive relations can then be written as:

$$\mathbf{D} = \epsilon^\top \cdot \mathbf{E} + d : \mathbf{T} \quad (2.66)$$

$$\mathbf{S} = \underline{d} \cdot \mathbf{E} + s^E : \mathbf{T}, \quad (2.67)$$

where \underline{d} is the piezoelectric strain matrix, a third rank tensor that will depend on the crystal symmetry of the material. The superscripts T and E have been added to the dielectric and compliance matrices, respectively, to denote the fact that those constants represent properties under fixed stress and electric fields, respectively. This is of significant importance for piezoelectric material, where stress and strain are related linearly.

If we again make the assumption that the strain is symmetric, we can simplify \underline{d} using that $\underline{d}_{ijk} = \underline{d}_{jik}$, leading to the abbreviated constitutive relations:

$$\mathbf{D}_i = \epsilon_{ij}^\top \cdot \mathbf{E}_j + d_{iJ} : \mathbf{T}_J \quad (2.68)$$

$$\mathbf{S}_I = \underline{d}_{Ij} \cdot \mathbf{E}_j + s_{IJ}^E : \mathbf{T}_J. \quad (2.69)$$

The simplified piezoelectric tensors are now given by

$$[d_{iJ}] = \begin{bmatrix} d_{x1} & d_{x2} & d_{x3} & d_{x4} & d_{x5} & d_{x6} \\ d_{y1} & d_{y2} & d_{y3} & d_{y4} & d_{y5} & d_{y6} \\ d_{z1} & d_{z2} & d_{z3} & d_{z4} & d_{z5} & d_{z6} \end{bmatrix}, \quad (2.70)$$

and

$$\underline{d}_{Ij} = \begin{bmatrix} d_{1x} & d_{1y} & d_{1z} \\ d_{2x} & d_{2y} & d_{2z} \\ d_{3x} & d_{3y} & d_{3z} \\ d_{4x} & d_{4y} & d_{4z} \\ d_{5x} & d_{5y} & d_{5z} \\ d_{6x} & d_{6y} & d_{6z} \end{bmatrix}, \quad (2.71)$$

respectively.

Alternatively, the piezoelectric constitutive relations can be expressed in the stress-charge form:

$$\mathbf{D} = \epsilon^S \cdot \mathbf{E} + e : \mathbf{S} \quad (2.72)$$

$$\mathbf{T} = -\underline{e} \cdot \mathbf{E} + c^E : \mathbf{S}. \quad (2.73)$$

In the case of the wurtzite crystal structure, the piezoelectric matrix is given by

$$[e] = \begin{bmatrix} 0 & 0 & 0 & 0 & e_{51} & 0 \\ 0 & 0 & 0 & e_{51} & 0 & 0 \\ e_{31} & e_{31} & e_{33} & 0 & 0 & 0 \end{bmatrix}. \quad (2.74)$$

2.3.3 Commonly Used Piezoelectric Transducers

There are various ways in which we can transfer energy between the electrical and mechanical domain in a piezoelectric solid. One of the most common one is typically encountered in Surface Acoustic Wave devices (SAW), and it involves using an interdigital transducer (IDT) to launch the waves [1]. These transducers are formed by interlocking two arrays of comb-shaped electrodes as shown in Figure 2-7 (a). One electrode set is grounded, while the other one is set to an AC voltage, which will lead to a periodically distributed electrical field. Depending on the crystal symmetry of the substrate, these fields will couple piezoelectrically to periodic strain fields, and launch acoustic waves. On the sense side, when the half wavelength of the traveling

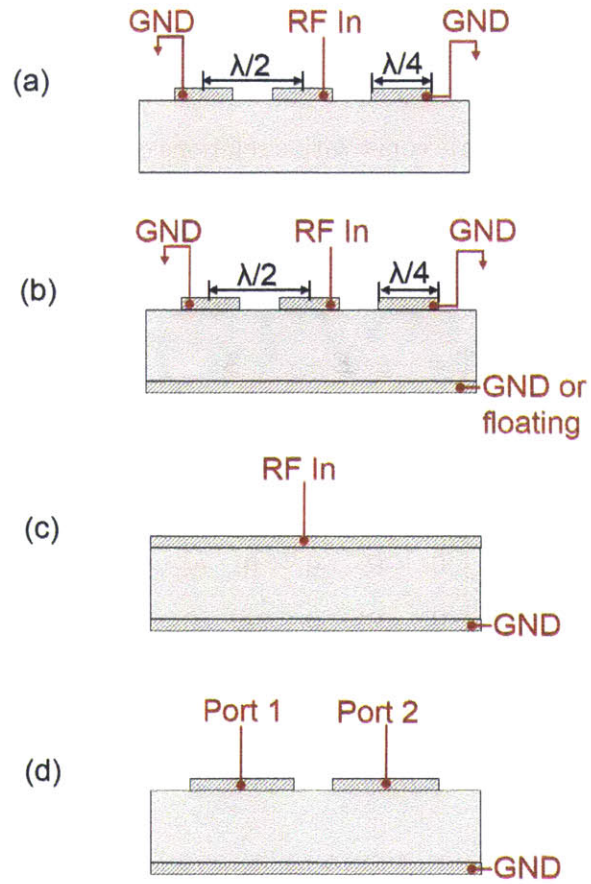


Figure 2-7: Common types of transducers used in piezoelectric acoustic devices. (a) Interdigital transducer. (b) Interdigital transducer with a grounded or floating electrode. (c) Fully electroded transducer. (d) 2 Port transducer with bottom electrode.

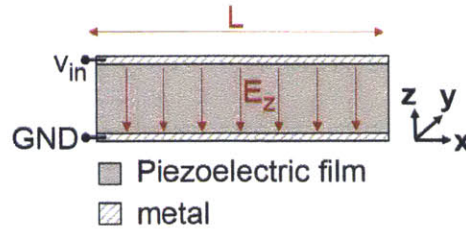


Figure 2-8: Piezoelectric transduction of a longitudinal resonant bar (side-view) using a fully electroded piezoelectric film.

wave equals the period of the transducer, the piezoelectric charge generated will lead to an overall output current.

This type of transducer is also used in the case of MEMS devices, where the piezoelectric film is released from the substrate. For example, IDTs are the most common way of driving and sensing Lamb-wave resonators. In the case of MEMS resonators, we can also deposit a bottom electrode, which can be grounded or floating. This will impede the fields from exiting at the bottom of the resonator, leading to a more efficient coupling.

Another type of transducer that is commonly used is a fully electroded one, where the piezoelectric film is sandwiched between two blanket electrodes (Figure 2-7 (c)). This is an efficient way of driving thickness extensional modes, in devices such as Film Bulk Acoustic Resonators (FBAR). Alternatively, we can use a 2-Port version of this transducer (Figure 2-7 (d)).

2.3.4 Comparison Between Capacitive and Piezoelectric Transduction

To compare piezoelectric and capacitive transduction, we revisit the example of a longitudinally vibrating bar, but now we use piezoelectric transduction, as illustrated in Figure 2-8. This shows the side view of a piezoelectric film, sandwiched between two metal electrodes. We assume that the piezoelectric film is a hexagonal crystal (GaN, AlN). A small AC electric field is applied across the film, between the two metal electrodes.

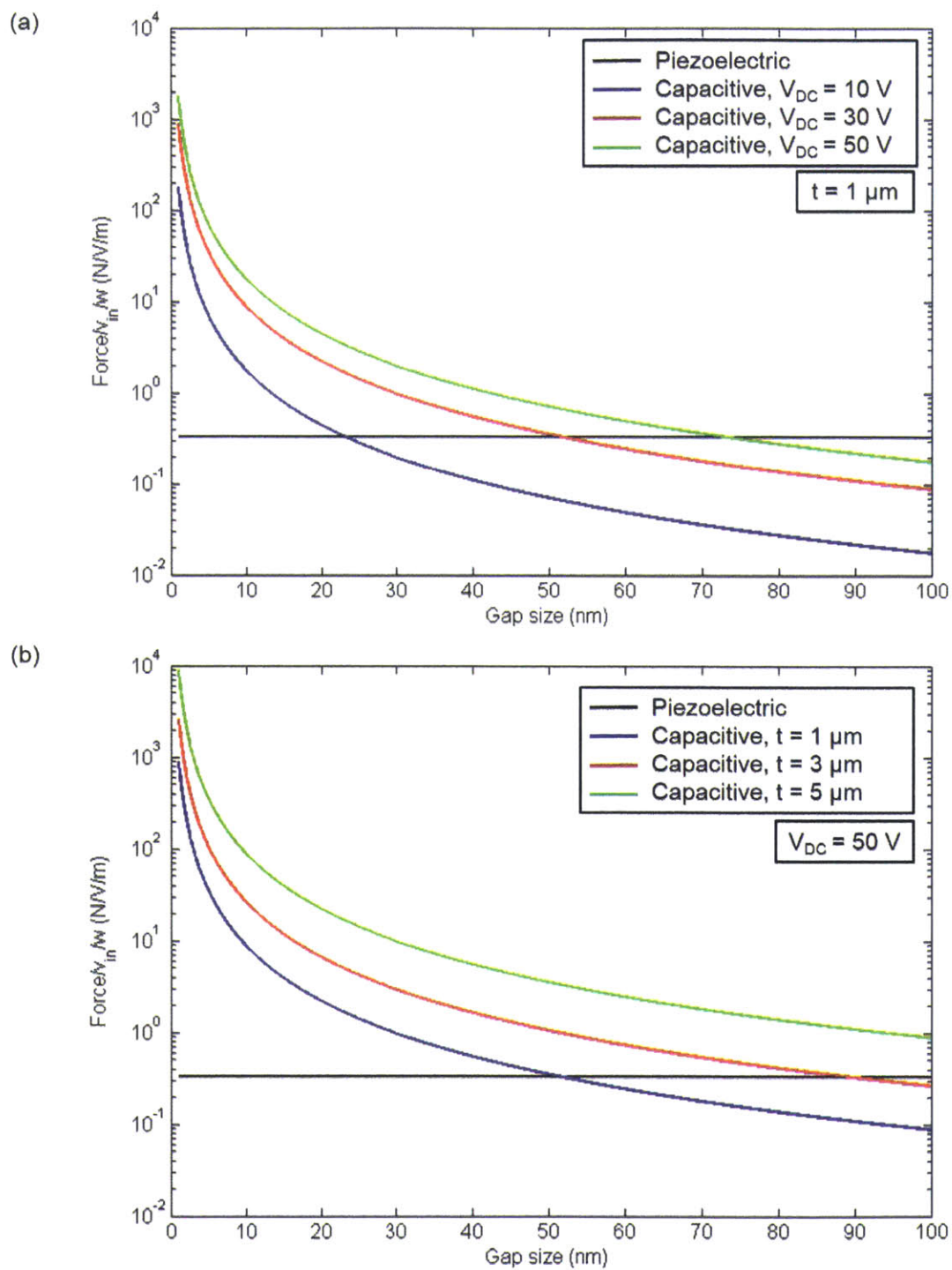


Figure 2-9: Comparison between piezoelectric and electrostatic drive force for different (a) DC bias conditions and (b) different film thicknesses in the case of a longitudinal bar.

We can then use Equation 2.73 to write the constitutive relations for this problem, assuming wurtzite crystal symmetry:

$$D_3 = \epsilon_{33}E_3 + e_{31}S_1 \quad (2.75)$$

$$T_1 = -e_{31}E_3 + c_{11}S_1. \quad (2.76)$$

For simplicity we can assume that the bar is clamped at both ends, which allows us to set the strain to zero. Then we obtain that the resulting drive force is

$$F_{piezo} = e_{31}v_{in}w, \quad (2.77)$$

where w is the width of the bar.

We can now compare the normalized drive force per device width per volt for the two cases, capacitive and piezoelectric. We use the piezoelectric coefficient of wurtzite Gallium Nitride. Figure 2-9 shows the comparison between the drive force per volt per device width for capacitive and piezoelectric. In the case of the piezoelectric drive, the induced force is proportional to the coefficient e_{31} without any additional geometric dependence. On the other hand, the electrostatic force depends on both the gap size and thickness of the resonator, as well as the applied DC bias. Figure 2-9 (a) shows the induced capacitive drive force for as a function of gap size, for three different values of applied DC bias. The thickness of the device is held constant, at $1\mu m$. It can be seen that even for a DV bias of 50 Volts, the piezoelectric transduction is more efficient than the electrostatic one. In (b), increasing the device width brings the required gap size down, but we still require gap sizes of the order of a couple of nanometers. In practice, scaling the film thickness will also limit the achievable frequency range (Section 2.2.5).

Additionally, the quadratic dependence on the gap size can lead to significant nonlinearities, and low yield due to fabrication variability. Piezoelectric devices would require no air-gap, leading to a linear, more efficient and robust transduction.

2.3.5 Electromechanical Coupling Efficiency

The previous section compared the efficiency of the piezoelectric drive force to the electrostatic one. However, in practice, we care about the overall transduction efficiency, from electrical to mechanical and back to the electrical domain. This section introduces the concept of electromechanical coupling efficiency.

Intrinsic Electromechanical Coupling Coefficient

One figure of merit used to quantify the inherent piezoelectric strength of an acoustic wave propagating through a given substrate is the electromechanical coupling efficiency, k^2 . Consider a wave propagating through a piezoelectric medium. Then from Section 2.3.2, we know that the constitutive relations can be written as:

$$\mathbf{D}_i = \epsilon_{ij}^\top \cdot \mathbf{E}_j + d_{iJ} : \mathbf{T}_J \quad (2.78)$$

$$\mathbf{S}_I = \underline{d}_{Ij} \cdot \mathbf{E}_j + s_{IJ}^E : \mathbf{T}_J. \quad (2.79)$$

We can now write the total energy contained in the acoustic and electric fields, respectively [48]:

$$\frac{1}{2} \sum_p S_p T_p = \frac{1}{2} \sum_{pq} s_{pq}^E T_p T_q + \frac{1}{2} \sum_{pq} s_{pq}^E T_p T_q \quad (2.80)$$

$$= U_1 + U_{12},$$

$$\frac{1}{2} \sum_i E_i D_i = \frac{1}{2} \sum_{iq} d_{iq} E_i T_q + \frac{1}{2} \sum_{ij} \epsilon_{ij} E_i E_j \quad (2.81)$$

$$= U_{12} + U_2.$$

Here, U_1 is the elastic energy density, U_2 is the electrical one, while U_{12} corresponds to the piezoelectric energy density. Then the electromechanical coupling factor is defined as:

$$k = \sqrt{\frac{U_{12}^2}{U_1 U_2}}, \quad (2.82)$$

while the transduction efficiency is defines as

$$k^2 = \frac{U_{12}^2}{U_1 U_2}. \quad (2.83)$$

This parameter, k , is also known as the intrinsic coupling coefficient, and it will depend on different values of the elastic, dielectric and piezoelectric matrices, for different modes of interest. For example, if we are assuming a case where we use an electric field in the z direction to launch longitudinal waves in the x direction, similar to the case shown Figure 2-8, we get

$$k^2 = k_{31}^2 = \frac{d_{31}^2}{\epsilon_{33}^T s_{11}^E}. \quad (2.84)$$

Since the piezoelectric coupling modifies the potential energy contained in the fields, this will lead to a change in the effective stiffness of the medium, as seen by the wave. The constitutive equations (see Section 2.3.2) can be rewritten as an equivalent Hooke's law [49]:

$$T = c_{eq} S, \quad (2.85)$$

where

$$c_{eq} = c \left(1 + \frac{e^2}{c\epsilon} \right). \quad (2.86)$$

Then we recover the electromechanical transduction efficiency k^2 :

$$k^2 = \frac{e^2}{c\epsilon}. \quad (2.87)$$

The actual components of the piezoelectric, dielectric and stiffness matrices used here will depend on the excited mode.

A change in effective stiffness is equivalent to a change in the phase velocity of the wave. As a result, the intrinsic electromechanical coupling coefficient can be approximated by computing the difference between the phase velocity of the wave propagation under two distinct surface electrical boundary conditions: free (open-circuit) and metallized (short-circuit). This method was originally developed for

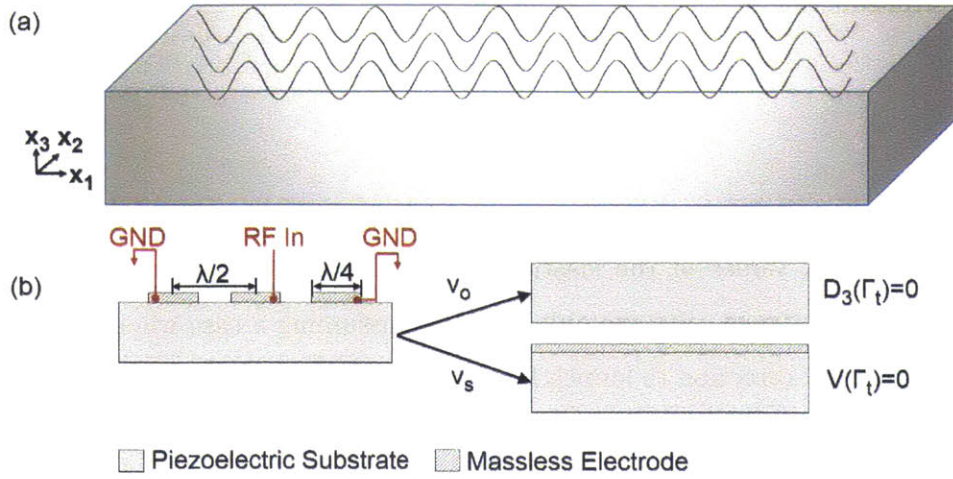


Figure 2-10: (a) Surface acoustic waves are propagating in the x_1 -direction through an infinite piezoelectric substrate. The system of coordinates is placed with the center on the median plane of the plate. (b) Setup for extracting the electromechanical coupling efficiency, k^2 , by computing the difference between the phase velocity when the top surface is set to zero charge (v_0) with the velocity under top surface shorting conditions (v_s).

characterizing the efficiency of SAW propagating in piezoelectric media [50, 51] and is illustrated in Figure 2-10. However, we can use very similar approach to characterize transduction efficiency in MEMS resonators.

It can be shown that the intrinsic coupling efficiency for a piezoelectric substrate is given by [51]

$$k^2 = 2\left(1 + \frac{\epsilon_0}{\epsilon_p}\right)\left(\frac{v_0 - v_s}{v_0}\right)\left(1 - \frac{v_0 - v_s}{v_0}\right)^{-1}, \quad (2.88)$$

where v_0 is the phase velocity under open-circuit (free) boundary conditions, and v_s is the phase velocity in the shorted case.

In the case of most piezoelectric materials of interest for this work, Equation 2.88 can be reduced to:

$$k^2 = 2\frac{v_0 - v_s}{v_0}. \quad (2.89)$$

2.4 Lumped Modeling of MEMS Resonators

This section derives a model for representing the behavior of MEMS resonators in the electrical domain only, using equivalent circuit elements that correctly describe the phenomenology of the device. This approach has two main goals. First, by reducing the set of complex continuum mechanics equations to a lumped model which only communicates with the outside world via terminals, we can easily use these devices as components of systems. Second, extracting a standardized set of parameters across multiple devices allows us to easily compare the performance of different resonators, even if the physics governing these systems at the microscopic level might be different. An excellent example for this second benefit is the comparison between a longitudinal bar resonator that is driven capacitively, and one that is transduced via the piezoelectric effect. There are two parts to this method. The first step is to take the distributed constitutive relations describing the device of interest, and derive equivalent lumped parameters in the mechanical domain, as shown in Figure 2-11. We have encountered a first example of a lumped mechanical system in Section 2.1, where a simple harmonic oscillator was modeled as mass connected to a spring. We use energy arguments to transform the solutions to the distributed differential equations into lumped equivalent components. The next step is to find electrical analogues that would lead to the same differential equations, and resonance condition. We choose to represent this as a high-Q LC Network. This is mainly motivated by the primary applications of MEMS resonators, creating narrow bandwidth frequency responses, for both frequency sources and filters.

2.4.1 Lumped Mechanical Components

We first discuss the equivalent mechanical lumped parameters of a distributed system, such as a MEMS resonator. For simplicity, we illustrate this method using a 1D example, the longitudinal clamped-bar that was introduced in Section 2.3.2. We

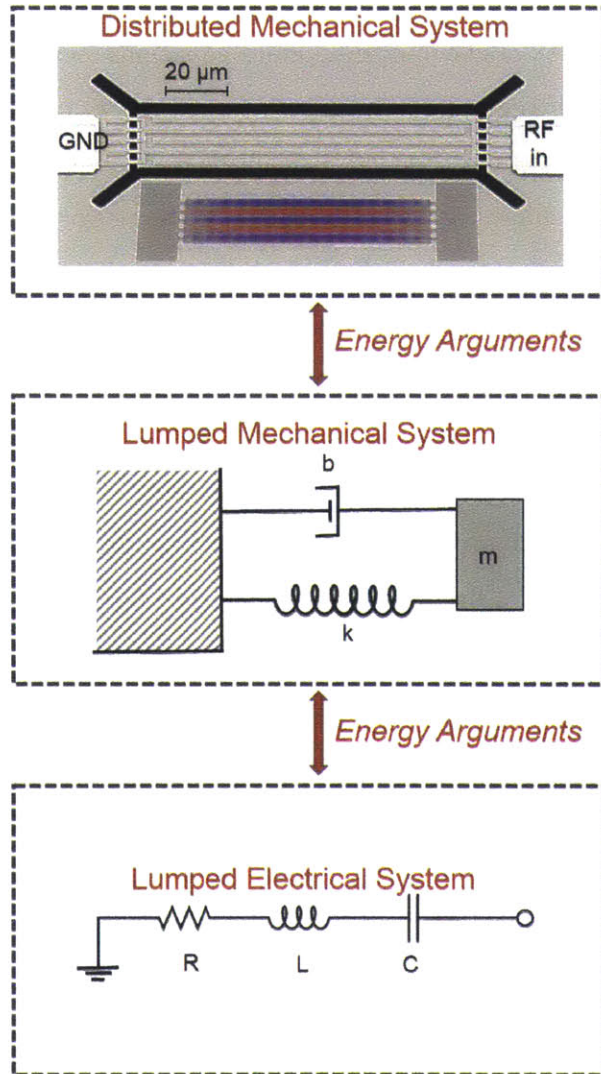


Figure 2-11: Methodology for transforming a distributed MEMS resonator model to a lumped equivalent circuit in the electrical domain.

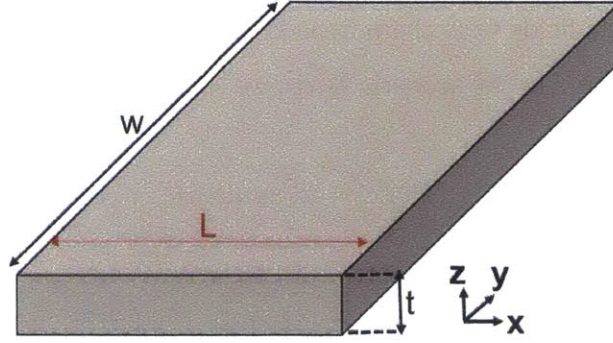


Figure 2-12: Methodology for transforming a distributed MEMS resonator model to a lumped equivalent circuit in the electrical domain.

assume displacement fields in the x direction only, given by

$$u(x) = u_{x0} \sin\left(\frac{\pi x}{L}\right) e^{i\omega t}. \quad (2.90)$$

For a self-consistent model, we want the kinetic energy of the lumped system to be equal to the total kinetic energy of the distributed mode:

$$\frac{1}{2} m_{eq} \dot{X}_L^2 = \frac{1}{2} \int_0^L \rho w t \dot{u}(x)^2 dx, \quad (2.91)$$

where m_{eq} is the equivalent mass of the lumped system, and ρ , w and t are the density, width and thickness of the bar. Here, \dot{X}_L^2 is taken to be the velocity of the lumped system, which we define as the maximum velocity of the distributed bar. For the mode shape introduced above, this will happen when $x = L$. We can then integrate Equation 2.4.1 and solve for the equivalent mass:

$$m_{eq} = \frac{\rho L w t}{2} = \frac{m}{2}. \quad (2.92)$$

So we conclude that the longitudinal vibrations in the bar contain the same kinetic energy as an equivalent particle of half the mass of the bar, moving at the maximum speed achieved in the bar.

Next, we want to derive an equivalent stiffness so we equate the potential energy

stored in the acoustic fields with the potential energy stored in a spring. To compute the elastic energy stored in the acoustic fields, we write the work done by the restoring force:

$$Fu(x) = T_1 w t u(x). \quad (2.93)$$

We can now use Hooke's law (Equation 2.40) to write

$$Fu(x) = c_{11} w t \frac{du(x)}{dx} u(x). \quad (2.94)$$

We then equate the total elastic energy stored in the bar with the potential energy of the lumped system:

$$\frac{1}{2} k_{eq} X_L^2 = \frac{1}{2} \int_0^L c_{11} w t \frac{du(x)^2}{dx^2} dx, \quad (2.95)$$

which gives

$$k_{eq} = \frac{\pi^2 c_{11} w t}{8 L} = \frac{\pi}{8} k. \quad (2.96)$$

Here, k is the stiffness of the bar in the presence of an axial load.

The last element that needs to be accounted for is the damping experienced by these waves. As we will see later in Section 2.5, there are multiple sources of loss in a resonator, ranging from intrinsic dissipation mechanisms, to design-dependent loss, such as radiation of energy through the anchoring beams. We combine all of these sources of loss into a viscous damping term, b . From Section 2.1.2, we can write this damping coefficient as:

$$b = \frac{km}{Q} = \frac{\sqrt{km}}{Q}, \quad (2.97)$$

where Q is the quality factor of the resonance. Then, using Equations 2.96 and 2.92, we obtain the equivalent lumped damping coefficient:

$$b_{eq} = \frac{\pi}{4} b. \quad (2.98)$$

Table 2.1: Direct (current) analogy between the mechanical and electrical domain for a lumped MEMS resonator.

Mechanical Quantity		Electrical Analogue	
Force	F	Voltage	V
Velocity	\dot{u}	Current	I
Mass	m_{eq}	Inductance	L_m
Compliance	$1/k_{eq}$	Capacitance	C_m
Damping	b_{eq}	Resistance	R_m

2.4.2 Lumped Electrical Components

We have seen in the previous section that we can represent a specific mode shape by a lumped spring-mass-damper system. Now we want to take this a step further, and find an equivalence between this mechanical lumped model and an electrical counterpart. As discussed above, it is useful to think of a MEMS resonator in terms of RLC network. This analogy is illustrated in Figure 2-13. The correspondence between the two domains can be drawn by looking at the differential equations governing each case:

$$m\ddot{x}(t) + b\dot{x}(t) + kx(t) = Fe^{i\omega t} \quad (2.99)$$

$$L\frac{di(t)}{dt} + Ri + \frac{1}{C} \int idt = Ve^{i\omega t}. \quad (2.100)$$

There are two main conventions for mapping the mechanical to electrical domain [45]. One convention is known as the $e \rightarrow V$ and it implies assigning effort, or pressure to voltage. The other convention is known as $f \rightarrow V$ and it is based on the equivalence of flow (velocity) to voltage. We choose to map the domains according to the first representation, based on the equivalence between the force in the mechanical domain and the voltage in the electrical one. These are known as "across" variables, while displacement and current are designated as "through" variables. This way of mapping is also known as the direct (current) analogy and is shown in Table 2.1.

We can now derive expressions for the equivalent lumped elements in the electrical

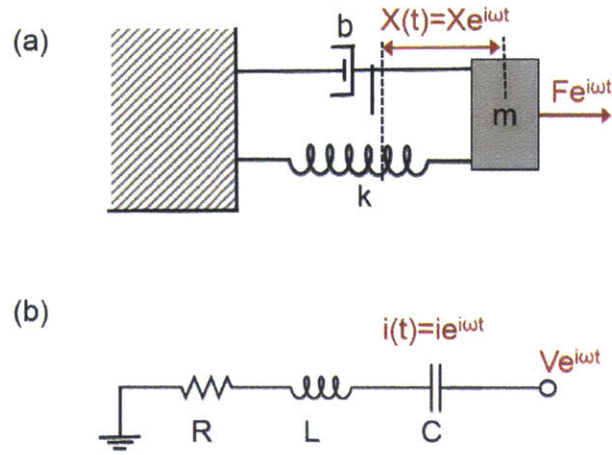


Figure 2-13: Electromechanical analogue between spring-mass-damper in the mechanical domain and RLC network in the electrical one.

domain by equating the kinetic and potential energies stored in the two domains. First, from the equality of the kinetic energy we get

$$\frac{1}{2}m_{eq}\dot{X}_L^2 = \frac{1}{2}L_m I^2, \quad (2.101)$$

and from the potential energy expression we obtain

$$\frac{1}{2}k_{eq}X_L^2 = \frac{1}{2}C_m V^2. \quad (2.102)$$

Next, we introduce the transduction factor

$$\Gamma = \frac{F}{V} = \frac{I}{\dot{u}}. \quad (2.103)$$

Then the lumped equivalent inductance and capacitance are given by:

$$L_m = \frac{m_{eq}}{\Gamma^2}, \quad (2.104)$$

and

$$C_m = \frac{\Gamma^2}{k_{eq}}, \quad (2.105)$$

respectively. The equivalent motional resistance, R_m is given by:

$$R_m = \frac{\sqrt{L/C}}{Q} = \frac{b_{eq}}{\Gamma^2}. \quad (2.106)$$

While the expressions for R_m , C_m and L_m derived above are general, in the end they will depend to the transduction factor Γ , which is different for each type of transduction. For example, revisiting the comparison between the piezoelectric and capacitive transduction of a longitudinal bar shown in Section 2.3.4, we can now write the transduction factors as

$$\Gamma_{cap} = \frac{\epsilon_0 v_{DC} w t}{g^2} \quad (2.107)$$

$$\Gamma_{piezo} = e_{31} w. \quad (2.108)$$

2.4.3 Modified Butterworth van Dyke Model

We have already derived a model for representing the mechanical resonance in the electrical domain. In reality, a resonator will also have additional components, such as the physical capacitance of the drive electrodes. Moreover, to account for losses associated with the electrode fingers, or the leakage through the GaN film we use a version of the Modified Butterworth Model (MBVD) [52], shown in Figure 2-14. The characteristics of the mechanical resonance are lumped into a series RLC branch (shown in blue). The capacitance C_0 is a physical capacitance associated with the electric fields formed between the two pairs of interdigitated fingers. An additional resistance, R_0 , is placed in parallel with the mechanical branch to model conductive and dielectric losses through the GaN film. Finally, the series resistance and inductance of the electrodes are R_s and L_s , respectively.

The frequency response generated by this circuit is shown in Figure 2-15, where the parallel and anti-parallel resonance frequencies, f_s and f_p , respectively, are given

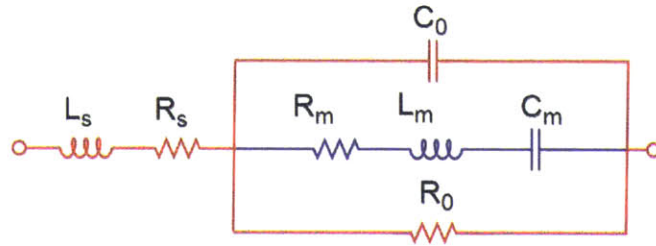


Figure 2-14: Equivalent circuit for modeling MEMS resonator.

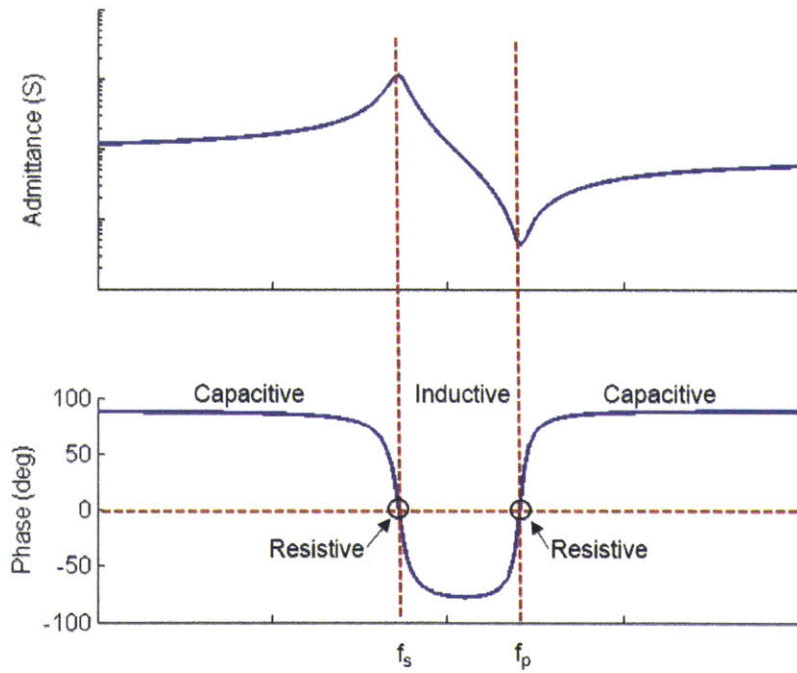


Figure 2-15: Frequency response of MBVD model.

by [52]

$$f_s = \frac{1}{2\pi} \sqrt{\frac{1}{L_m C_m}}, \quad (2.109)$$

$$f_p = \frac{1}{2\pi} \sqrt{\frac{1}{L_m C_m} \left(1 + \frac{C_m}{C_0}\right)}. \quad (2.110)$$

respectively.

Effective Electromechanical Coupling Coefficient

For the circuit shown above, we can quantify the ratio of elastic energy to electric energy stored inside the resonator by considering the ratio C_m/C_0 . Then the effective transduction efficiency is defined as [52], [42]:

$$k_{eff}^2 = 1 - \frac{f_s^2}{f_p^2}. \quad (2.111)$$

Then the relevant figure of merit is given by

$$FOM = \frac{k_{eff}^2 Q_L}{1 - k_{eff}^2}, \quad (2.112)$$

where Q_L is the electrically loaded quality factor of the resonator, calculated by

$$Q_L = \frac{R_m Q_m}{R_m + R_s}. \quad (2.113)$$

2.5 Dissipation Mechanisms in Acoustic Resonators

As we saw in Section 2.4, the lumped spring-mass-damper system is characterized by an equivalent viscous damping coefficient, b , which sums the contributions of all the loss mechanisms present in the resonator. While this approach is extremely useful for benchmarking and modeling, we want to gain understanding of what are the physical mechanisms that lead to energy dissipation and how we can minimize them. This section provides a summary of some of the most prominent loss mechanisms in MEMS resonators. We start by first discussing the design-dependent factors, such as

air damping, spurious mode coupling, anchor loss and surface effects. Then we move to discussing losses associated with intrinsic material properties, such as thermoelastic damping, phonon-electron interactions and phonon-phonon scattering. It can be shown that the overall quality factor of a resonance is given by:

$$\frac{1}{Q} = \sum_i \frac{1}{Q_i}, \quad (2.114)$$

where Q_i are the Q values corresponding to the different loss mechanisms present.

2.5.1 Air Damping

Air Damping refers to losses due to the friction between the resonator and the surrounding gas. More specifically, as the resonator moves, it will create sound waves in the surrounding air, leading to power dissipation. In many cases, MEMS resonators will be packaged in a low-pressure encapsulated environment, which means that the surrounding air is rarefied, corresponding to situations where the mean free path of the gas molecules is less than the wavelength of sound in air. We then need to treat the air molecules as non-interacting particles. The energy lost by the resonator can now be seen as momentum transfer to the surrounding molecules and it will be proportional to the number density and mean velocity of air molecules:

$$E_{dissipated} \propto n \cdot \bar{v} \propto \frac{P}{k_B T} \sqrt{\frac{8k_B T}{\pi m}} \propto \frac{P}{k_B T}, \quad (2.115)$$

where P is the ambient pressure, k_B is Boltzmann's constant and T the temperature.

While Equation 2.115 is true for most cases, the constant of proportionality will depend on the kind of waves that are excited, and the frequency of operation. Stiffer modes, with smaller displacements will generally lead to less energy transfer, making air damping less significant for high-frequency bulk modes.

2.5.2 Surface Losses

Surface losses arise as a result of abrupt differences between the properties of the bulk of a mechanical cavity and the ones encountered at edges. These can be caused by crystal defects in the semiconductor, such as micro-cracks and roughness due to processing, or layers of adsorbed molecules of gases, water and left-over polymers from processing. Metal electrode loading can also be considered as part of surface dissipation, as the acoustic mismatch between the semiconductor and the metal can lead to severe wave scattering. As there has been a huge push towards the miniaturization of MEMS resonators, the ratio of surface to volume of the cavities has increased, making these surface effects become more relevant.

The loss-mechanism associated with these defects can be thought of an imperfect boundary condition, which leads to inhomogeneous heating, generating a flow of phonons to re-equilibrate the system. When the wavelength of the propagating wave is larger than the defect domains, this homogenization happens in a time

$$\tau_T^* = \frac{a^2}{D_T}, \quad (2.116)$$

where D_T is the thermal diffusion coefficient and a is the size of the defect domain. While there have been many attempts to model surface losses [53], there is still no unified theory that can correctly fit all the data.

2.5.3 Losses due to Mode Coupling

Due to the connection between strains in different crystal directions, given by the non-zero coefficients of the elasticity matrix, c_{ij} , different vibration modes will be coupled. This means that if we input energy into a particular mode, using an optimized transducer, some energy can leak to another mode that would not be efficiently transduced otherwise. This becomes of significant importance when the modes are really close in frequency.

2.5.4 Loss due to Dissipation through Anchoring Beams

Energy radiated to the surrounding substrate is the dominant dissipation mechanisms in MEMS resonators, and has been subject to many studies. Over the past years, researchers have developed various solutions to reduce these losses. The main approach is to design suspension beams that are placed at nodal points and also have an equivalent length corresponding to a quarter wavelength of the mode of interest, therefore insuring minimal displacement at the point of contact with the substrate. For high frequency modes bulk, where the thickness of the beam becomes comparable with its lateral dimensions, this becomes extremely challenging, as there will be many modes coupling. Additional solutions involve the use of etched trenches on the substrate side for increased reflection [54], and the use of a Phononic crystal with a bandgap centered around the frequency of interest [55].

2.5.5 Thermoelastic Damping

Thermoelastic damping takes place due to inhomogeneous volume compression regions due to the propagation of the wave, which will lead to temperature gradients and therefore a heat flow. As a result, some of the elastic energy gets converted into thermal energy. For most of the frequencies of interest, the attenuation due to thermoelastic damping can be written as [40]:

$$\alpha^{TED} = \frac{\kappa T \beta^2 \rho}{18 C_V^2 s} \omega^2. \quad (2.117)$$

Table 2.2 provides a description of the parameters and corresponding values for wurtzite GaN that can be used to calculate α^{TED} .

2.5.6 Phonon-Phonon Scattering

This fundamental scattering mechanism is caused by the anharmonicity of the crystal lattice. As a sound wave travels through a crystal, the elastic phonons will interact with the thermal phonons. There are two regimes of interest. First, when the wave-

length is larger than the mean free path of the thermal phonons, we can think of the wave as a local perturbation of the phonon population. This is known as the Akhiezer regime, and it was first formulated in 1938 [56]. The attenuation in this case is given by

$$\alpha^{PP} = \frac{C_v T \gamma^2 \tau}{2\rho s^3} \left(\frac{\omega^2}{1 + \omega^2 \tau^2} \right), \quad \omega\tau < 1. \quad (2.118)$$

The second regime deals with cases when the wavelength is smaller than the mean free-path of the thermal lattice phonons. This is known as the Landau-Rumer regime [57] and it leads to an attenuation given by

$$\alpha^{PP} = \frac{\pi^5 \gamma^2 k_B^4 T^4}{30\rho s^6 \hbar^3} \omega, \quad \omega\tau > 1. \quad (2.119)$$

Table 2.2 lists the parameters of interest and their corresponding values for wurtzite GaN. To compute the phonon lifetime we assume a 1D model for the thermal conductivity in a solid [58]:

$$\kappa = \frac{1}{3} C_V s l, \quad (2.120)$$

where κ is the thermal conductivity, C_V is the heat capacity and s and l are the mean velocity and mean free-path, respectively. Defining the phonon relaxation time as $\tau \equiv l/s$ we get

$$\tau = \frac{3\kappa}{C_V s^2}. \quad (2.121)$$

2.5.7 Phonon-Electron Scattering

The last intrinsic dissipation discussed here is based on interactions between the traveling elastic wave and the free electrons present in the solid. This mechanism is more pronounced in metals, but it can have a great impact on highly doped semiconductors or solids with strong electromechanical interactions, such as piezoelectrics [59]. There are two types of losses associated with phonon-electron interactions [60]. First, losses associated with the deformation potential of an electron are encountered in all types of semiconductors. This is due to the fact that the energy of a free electron will

depend on the applied strain:

$$U = \Xi S, \quad (2.122)$$

where U is the potential energy of the electron, Ξ is the deformation potential constant, and S is the strain. In the case of an position-dependent strain field, this leads to an electric field

$$E = -\frac{dU}{dx}. \quad (2.123)$$

As a result, some of the energy stored in the elastic fields gets transferred to the free electrons. It can then be shown that the attenuation coefficient due to the deformation potential is:

$$\alpha^{DP} = \frac{N\Xi^2}{9s^4k_B T\rho} \frac{\omega^2\tau_R}{1 + \omega^2\tau_R^2} \quad (2.124)$$

Here, τ_R is the intervalley relaxation time.

Generally, losses associated with deformation potential are negligible in semiconductors with low doping levels like in the case of RF GaN substrates.

Instead, we take a look at the second loss mechanism related to phonon-electron interactions. This is related to the piezoelectric nature of the material. Consider a sinusoidal wave propagating through a piezoelectric substrate. The resulting strain fields will give rise to alternating regions of positive and negative electric fields that will travel at the speed of sound. Free electrons will bunch in the regions of minimum potential energy. As the wave progresses, electrons tend to lag behind, so they need to be accelerated to follow the wave motion. This energy comes from the acoustic field and can be computed by considering by the average power transferred from the wave to the electrons:

$$\bar{P} = \langle N(x) \mathbf{E}(x) \cdot \mathbf{s} \rangle. \quad (2.125)$$

Then the attenuation coefficient is given by

$$\alpha^{PE} = \frac{k^2}{2s} \frac{\omega_c}{1 + \left(\frac{\omega_c}{\omega} + \frac{\omega}{\omega_D}\right)^2}, \quad (2.126)$$

where k is the electromechanical coupling coefficient, s is the sound velocity and ω_c

and ω_D are the and the Debye frequencies, respectively, given by:

$$\omega_c = \frac{\sigma}{\epsilon_r \epsilon_0}, \quad (2.127)$$

$$\omega_D = \frac{s^2 q_e}{\mu k_B T}. \quad (2.128)$$

Here, σ is the conductivity of the sample that depends on the level of doping and mobility of free carriers assumed.

One really important aspect of this interaction between the acoustic fields and the free carriers in a piezoelectric medium is that the damping effect can be reversed by applying a DC electric field. This will accelerate the free electrons to a drift velocity proportional to the strength of the applied field. If the drift velocity is larger than the velocity with the wave progresses, the free carriers will give away some of their kinetic energy to the acoustic wave. This is called acousto-electric amplification, and it has been observed for the first time in piezoelectric Cadmium Selenide [61].

2.5.8 Intrinsic Loss in Gallium Nitride

This section looks at what are the relative values of the attenuation due to all the intrinsic mechanisms described above for the special case of wurtzite Gallium Nitride. All the parameters used in this study are listed in Table 2.2. Figure 2-16 shows the calculated attenuation coefficients corresponding to the three intrinsic damping mechanisms: thermoelastic damping (TED), phonon-phonon scattering (phonon-phonon) and phonon-electron interactions (phonon-electron). The phonon-electron curve was calculated with a free electron density of $5 \times 10^{15} \text{cm}^{-3}$. In practice, the density of free carriers in an unintentionally doped GaN sample can vary from $1 \times 10^{13} \text{cm}^{-3}$ to $1 \times 10^{16} \text{cm}^{-3}$. We note that for the frequencies of interest, the attenuation set by thermoelastic damping is lower than the other two contributions. We also note that the phonon-electron damping can be reduced by using samples with a low number of free carriers. What this implies is that the ultimate damping limit would be set by the phonon-phonon scattering limit.

Table 2.2: Material properties used to calculate intrinsic loss attenuation coefficient for bulk, wurtzite GaN.

Quantity	Symbol	Value	Units	Reference
Mass density	ρ	6150	kg/m^3	[28]
Specific heat	C_s	490	$J/kg - K$	[28]
Electron mobility	μ	200	$cm^2/V - s$	[28]
Free electron density	N	5×10^{15}	cm^{-3}	—
Piezoelectric coupling efficiency	k^2	0.02	—	[28]
Dielectric constant	ϵ_r	8.9	—	[28]
Phonon relaxation time	τ	2.02×10^{-12}	s	—
Thermal conductivity	κ	130	$W/m - K$	[28]
Coefficient of linear expansion	β	5.6×10^{-6}	K^{-1}	[28]
Acoustic velocity	s	7960	m/s	[28]
Gruneisen parameter	γ	1.18	—	[62]

Figure 2-17 (a) shows the calculated phonon-phonon attenuation coefficient for the 5 main wave types supported by the GaN crystal structure. In (b), the $f \cdot Q$ product is shown, which is a convenient way of benchmarking the performance of the resonators. Note that while we have expressions for the two limiting cases, the Akhieser and Landau-Rumer regimes, the behavior due to scattering is unknown in the intermediate regime, which is represented by dashed lines. Additionally, the corner frequency and the magnitude of the attenuation coefficient could vary from sample to sample, as the number of crystal dislocations will affect the phonon lifetimes of the specimen.

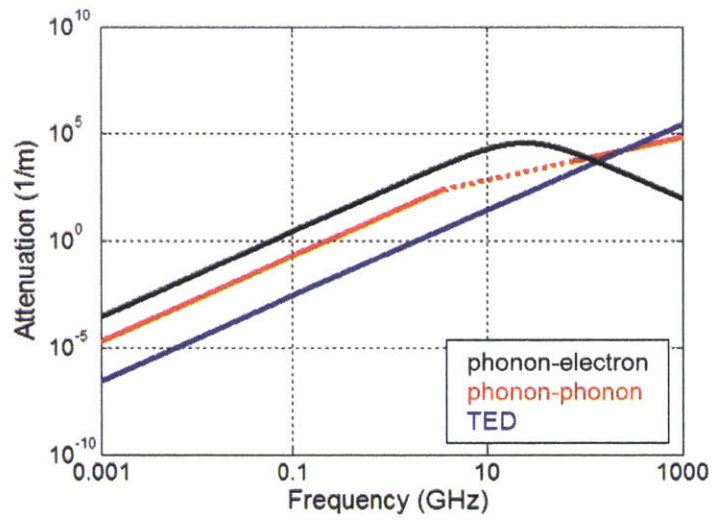


Figure 2-16: Calculated attenuation coefficients corresponding to the three intrinsic damping mechanisms: thermoelastic damping (TED), phonon-phonon scattering (phonon-phonon) and phonon-electron interactions (phonon-electron). The parameters used in this calculation are listed in Table 2.2.

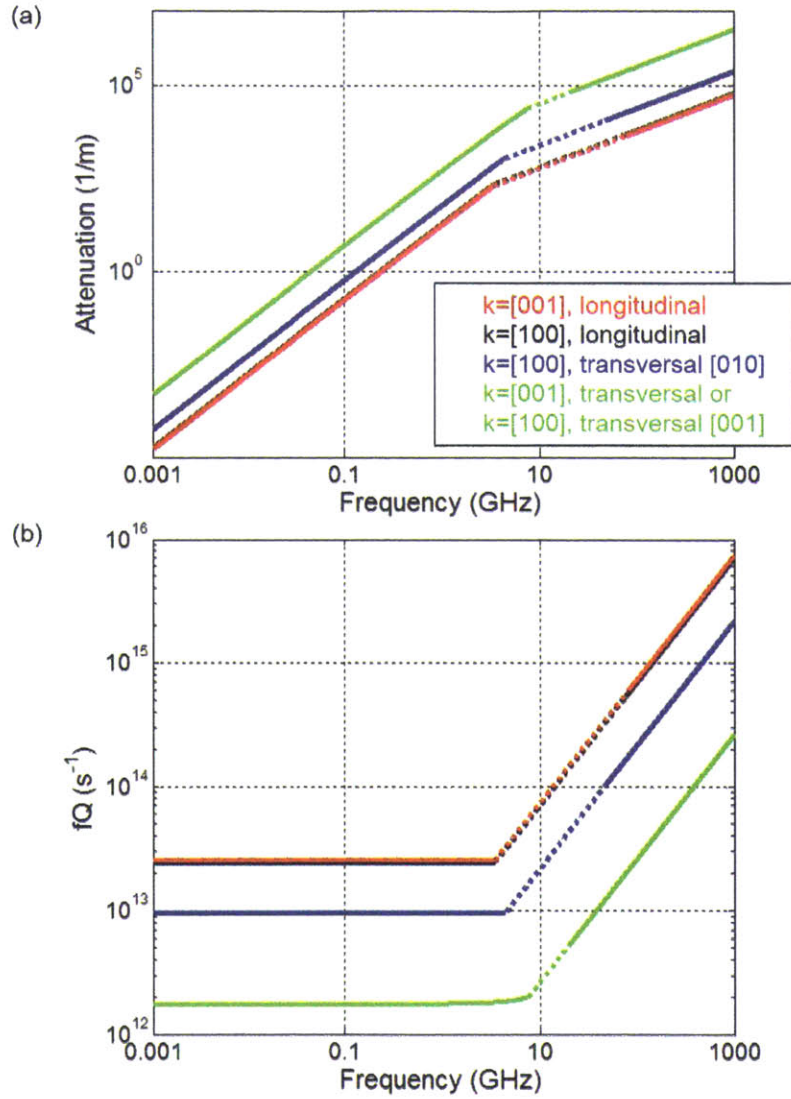


Figure 2-17: Calculated (a) attenuation coefficients and (b) $f \cdot Q$ product corresponding to phonon-phonon scattering in GaN, for the 5 main wave types supported by this crystal symmetry. The parameters used in this calculation are listed in Table 2.2.

Chapter 3

Fabrication and Characterization

3.1 GaN Growth and Characterization

Over the past few year, there have been many developments in the growth of GaN on various substrates, such as silicon carbide, sapphire and diamond [31]. The main driver for this technology has been the optoelectronic market, with GaN being heavily used for diodes, culminating with the awarding of the 2014 Nobel Prize in Physics for the discovery of the blue laser. The next market in order of relevance for this material is the high power, high-frequency electronics, with GaN becoming a strong candidate for Monolithic Microwave Integrated Circuit (MMICs), due to its high breakdown fields and high saturation velocities.

There are multiple growth techniques used to produce high quality GaN for the above applications but two of the most used ones are Molecular Beam Epitaxy (MBE) and Metallorganic Chemical Vapor Deposition (MOCVD) [63].

Recently, researchers were able to grow high quality GaN on Si-(111), which has the potential of not only lowering the cost of GaN wafers, but also of opening the market for new applications, such as the heterogenous integration of GaN MMICs with silicon CMOS circuits [32]. For MEMS devices, the use of silicon substrates as sacrificial layers enables suspended GaN cantilevers and membranes [33], leading to a wide spectrum of applications as discussed in Chapter 1.

In this study, we focus on MBE-grown GaN on a Silicon substrate, for an easy

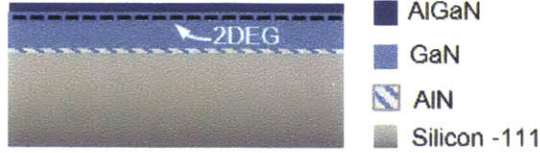


Figure 3-1: Structure of MBE-grown GaN on Silicon used in this work.

release of the MEMS. MBE was chosen over MOCVD growth due to reduced process temperatures, leading to lower residual stresses [63]. The growth is performed by Raytheon [64]. Figure 3-1. shows the epitaxy of the structure used in this thesis, a 24% $AlGaN$ ($25nm$)/ GaN ($1.7\mu m$), including a thin AlN nucleation layer. The role of this seed layer is to both avoid chemical reactions between the Gallium atoms and to provide a transition from the crystal lattice constant of the silicon substrate to the GaN film.

3.1.1 XRD

The crystal quality of GaN grown on silicon can be characterized via X-ray Diffraction (XRD) [65]. Figure 3-2 shows a characteristic coupled scan measurement of one the GaN on silicon samples used in this work. The narrow Full Width at Half Maximum of the peak corresponding to GaN implies good crystal quality over a long range.

3.1.2 Nanoindentation

Since we are interested in harnessing the mechanical properties of the MMIC stack to make high performance MEMS resonators, we performed nanoindentation experiments at MIT with a Hysitron Triboindenter using a Berkovich diamond tip, using the method described in [66]. A characteristic load-displacement scan of the epitaxial structure used in this thesis can be seen in Figure 3-3. Then the Young's modulus and Poisson ratio were extracted to be 264.95 GPa and 0.18, respectively. These values are comparable to other previously reported values for GaN on silicon substrates [67], [68].

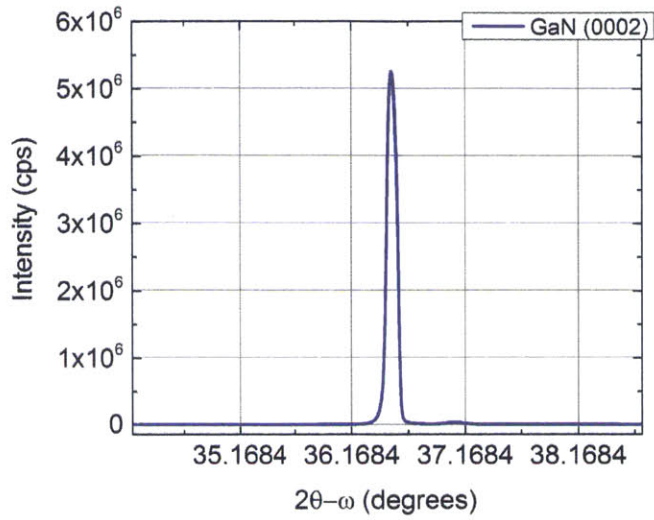


Figure 3-2: XRD spectroscopy of MBE GaN on silicon sample representative of the materials used in this thesis.

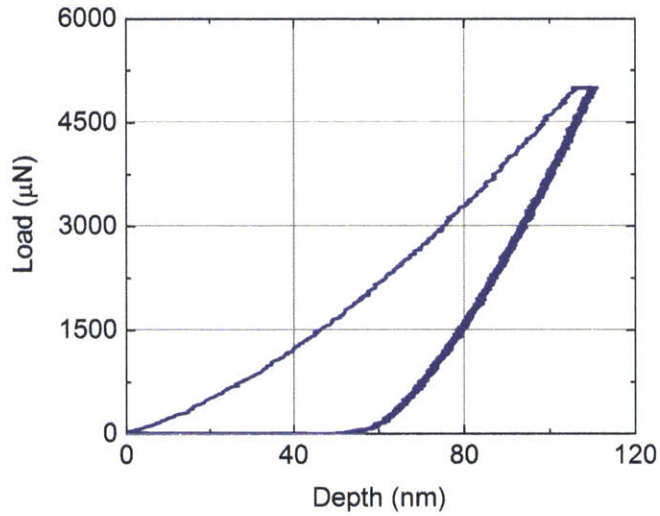


Figure 3-3: XRD spectroscopy of MBE GaN on silicon sample representative of the materials used in this thesis.

3.2 GaN Resonators in MMIC Technology

There are two main fabrication processes developed for the devices demonstrated in this thesis. These processes were both developed with the goal of realizing high-performance resonators integrated with HEMTs, with as little modification as possible to the MMIC technology. As a result, they are both variations of HEMT processes, with two additional steps for realizing the integrated MEMS. The first version uses a metalization scheme that includes Au, which was originally used for realizing low contact resistance Ohmic contacts to the 2DEG, as well as for lowering the series resistance of the gates. The second process is a variation of an Au-free HEMT process. Moreover, this first version was developed for transducers that use the 2DEG as a bottom electrode (Chapter 4), while the second version target devices where the 2DEG is removed from the acoustic cavity, to allow the electric fields to penetrate throughout the entire GaN volume (Chapter 5).

3.2.1 Au-based fabrication

The fabrication of the resonators is based on a HEMT process, with only two modifications to the standard MMIC flow, as shown in Figure 3-4. More details regarding the specific photolithography and etch recipes can be found in Appendix B.

The starting structure is 17 by 17 mm piece from a 4 inch GaN on silicon wafer (Figure 3-4 (a)). SEM images of the device during the main fabrication steps can be seen in Figures 3-5 to 3-8. The fabrication process starts with a shallow mesa etch of the AlGa_N which is used to remove the 2DEG from everywhere except for the active device area, where HEMTs or piezoelectric transducers will be formed (Figure 3-4 (b)). This is done in a Plasmaquest ECR etcher, using a BCl_3/Cl_2 chemistry. In reality, to make sure that the 2DEG is completely removed between different device islands, we overetch into the GaN. The overall step height is approximately 70-80 nm, and is typically characterized with Atomic Force Microscopy (AFM).

The next step in this process is the first modification to the standard HEMT process, a deep etch through the entire GaN film, stopping on Silicon (Figure 3-

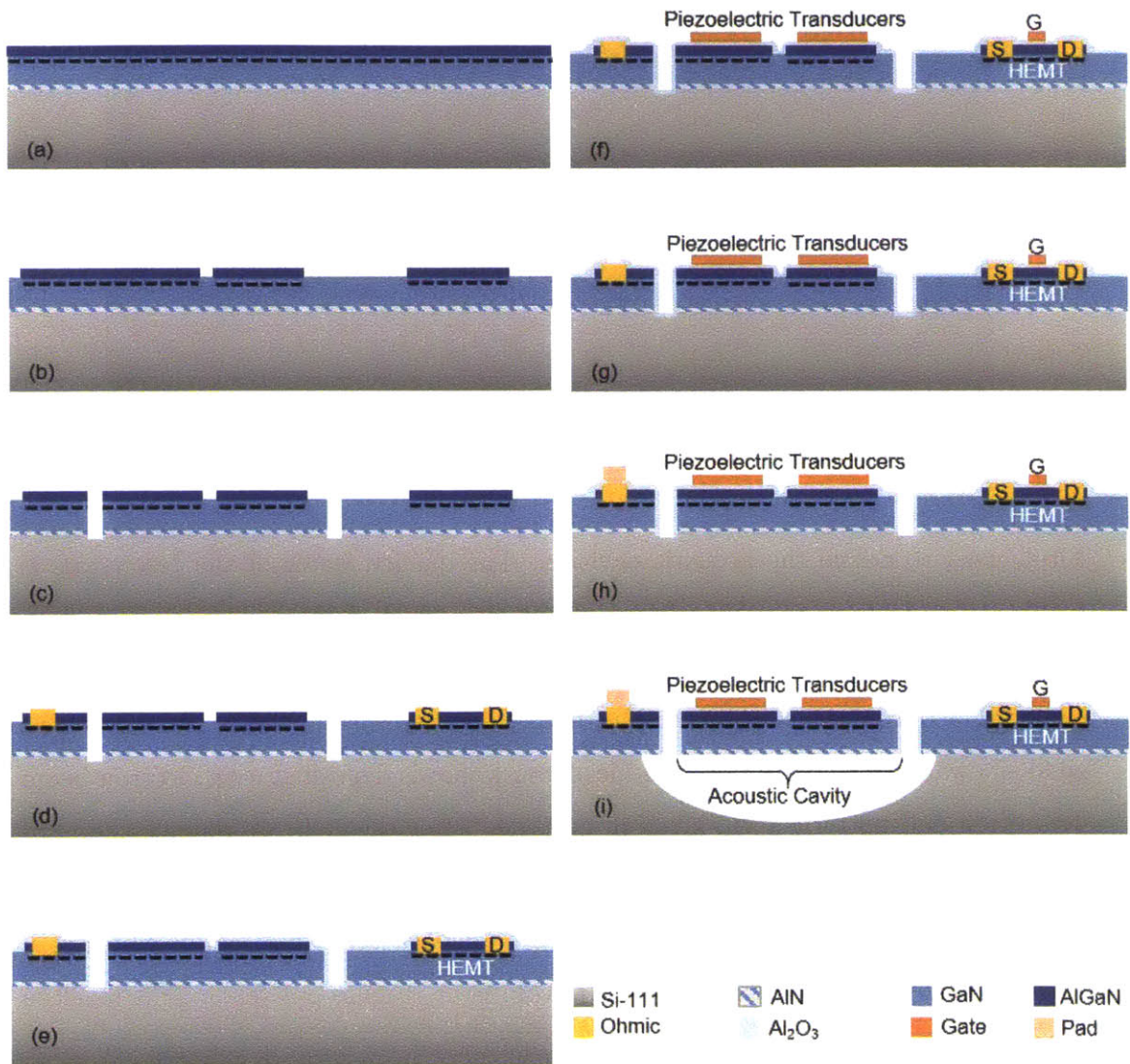


Figure 3-4: Fabrication process of GaN MEMS resonators in standard HEMT process with only two additional steps.

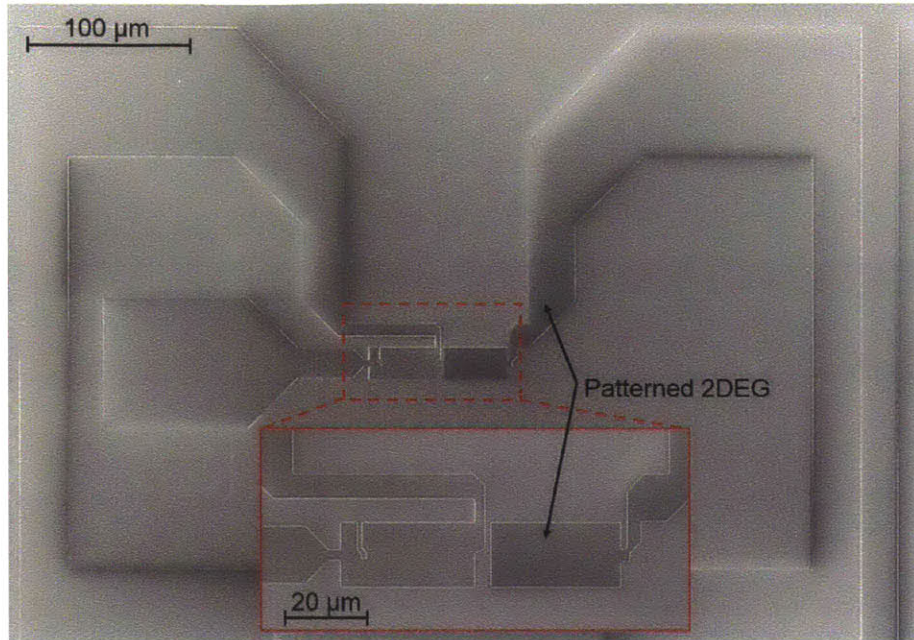


Figure 3-5: SEM image of resonator after the mesa etch step is finalized.

4 (c), used to define the acoustic cavities. The quality factor of the resonators is highly dependent on the smoothness of the side walls of the cavity (Section 2.5). As a result, we use an Inductively Coupled Plasma (ICP) etcher, with a Cl_2 based recipe. The optimization of this etch is further discussed in Appendix ?? To achieve a good sidewall profile, we use a hard nickel mask that is deposited with electron beam deposition and patterned via liftoff in acetone. After the etch, we remove the hard nickel mask in a wet nickel etchant solution, which does not affect the GaN.

Once the acoustic cavities are patterned, we deposit the ohmic metals which consist of Ti (20nm)/Al(100nm)/Ni(25nm)/Au(50nm) (Figure 3-4 (d)). This stack is deposited using ebeam deposition and then patterned via liftoff in acetone. To drive the metal through and form the ohmic contact we anneal the sample using a Rapid Thermal Anneal (RTA) tool, for 30 seconds at 870° . This step is used not only for accessing the channel of the HEMTs, but also for making contact to the 2DEG regions that will serve as bottom electrodes in piezoelectric transducers.

One requirement for MMIC technology is a high ON/OFF ratio for the HEMT current, which implies low gate leakage currents. A possible way to address this is by

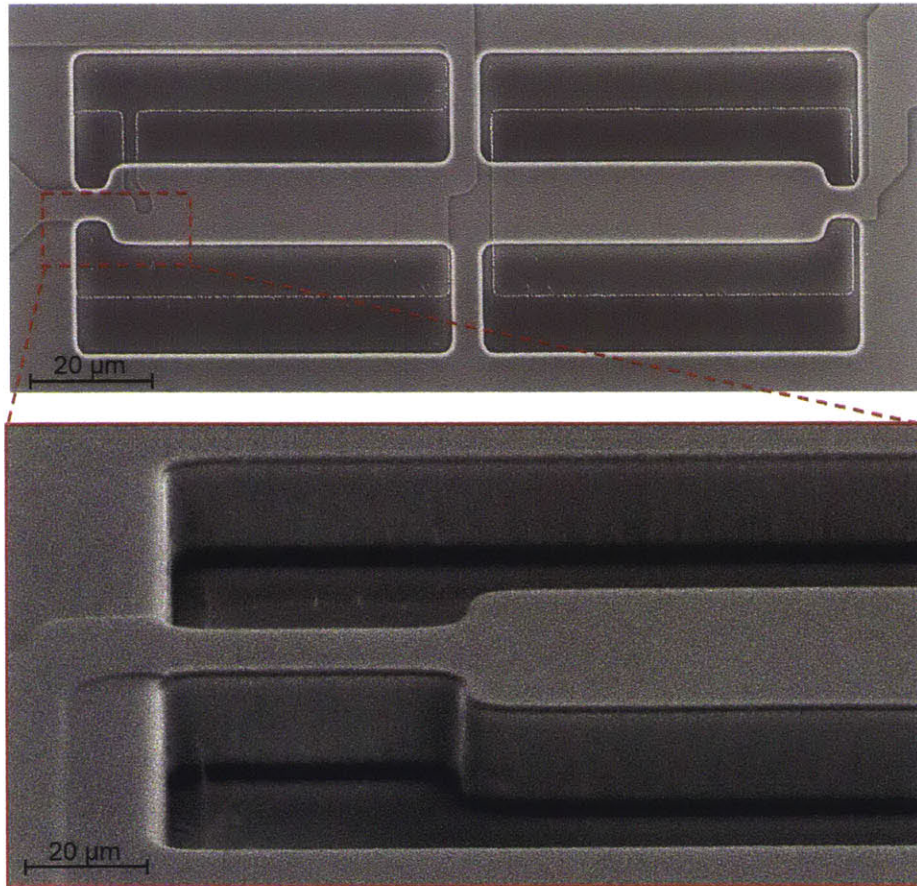


Figure 3-6: SEM image of resonator after the deep GaN etch is used to pattern the acoustic cavities.

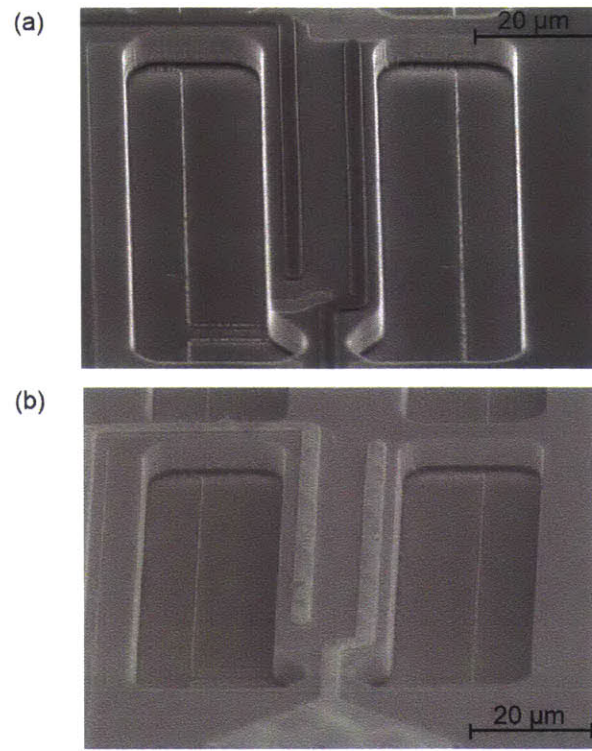


Figure 3-7: SEM image of resonator after the ohmic metal deposition (a) before and (b) after anneal at 870°C for 30 sec.

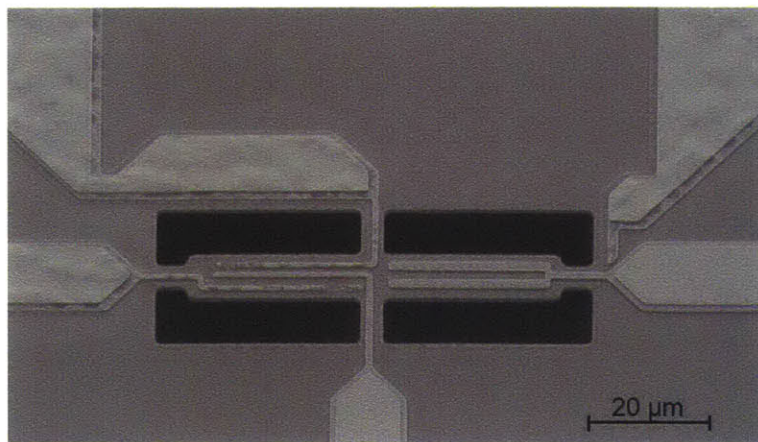


Figure 3-8: Released resonator.

including a thin gate dielectric (cite). We use a 17 nm Al_2O_3 that was deposited via Atomic Layer Deposition (ALD) shown in (Figure 3-4 (e)). This insures both a highly conformal layer, as well as really high quality and low density of pinholes, necessary for low leakage. The gate metal is then deposited via electron beam deposition and patterned through lift-off in acetone. At this point in the process, both the HEMTs and piezoelectric transducers are completed, as the gate metal of the HEMT serves as a top electrode in the transducer (Figure 3-4 (f)).

Next, we need to access the ohmic contacts that are covered by the gate dielectric, so we etch vias through the Al_2O_3 . We use a photoresist mask and then dip the sample in Buffered Hydrofluoric Acid (BOE) (Figure 3-4 (g)). Next, we deposit a thick metal typically 300 nm of Au, that will serve as interconnects and pads for landing the probes. This is done with an ebeam deposition tool, and then patterned though liftoff in acetone.

The final step is the second modification to the HEMT process, an isotropic silicon etch that releases the acoustic cavities. We use a photoresist mask to protect the surface of the devices, and only expose the trenches formed on the sides of the resonators. We then use XeF_2 , which will only etch the silicon and not attack the GaN layer (Figure 3-4 (i)).

3.2.2 Au-free HEMT Technology

Over the past few years, there have been numerous efforts to bring GaN MMIC technology into CMOS foundries, with the prospect of heterogeneous integration showing high potential for new systems and applications. As a result, eliminating Au from the HEMT process for CMOS compatibility [69] became a priority. For MEMS, Au-free electrodes also have the benefit of higher quality factors, as Au is a dense metal that will mass load the acoustic cavities and it also exhibits high losses through phonon-electron scattering (Section 2.5). This is the first implementation of GaN MEMS resonators in an Au-free HEMT process flow, leading to resonators with $f \cdot Q$ products as high as 1.5×10^{13} , which is not only the highest value demonstrated in GaN resonators to date, but also approaching the fundamental theoretical limit set

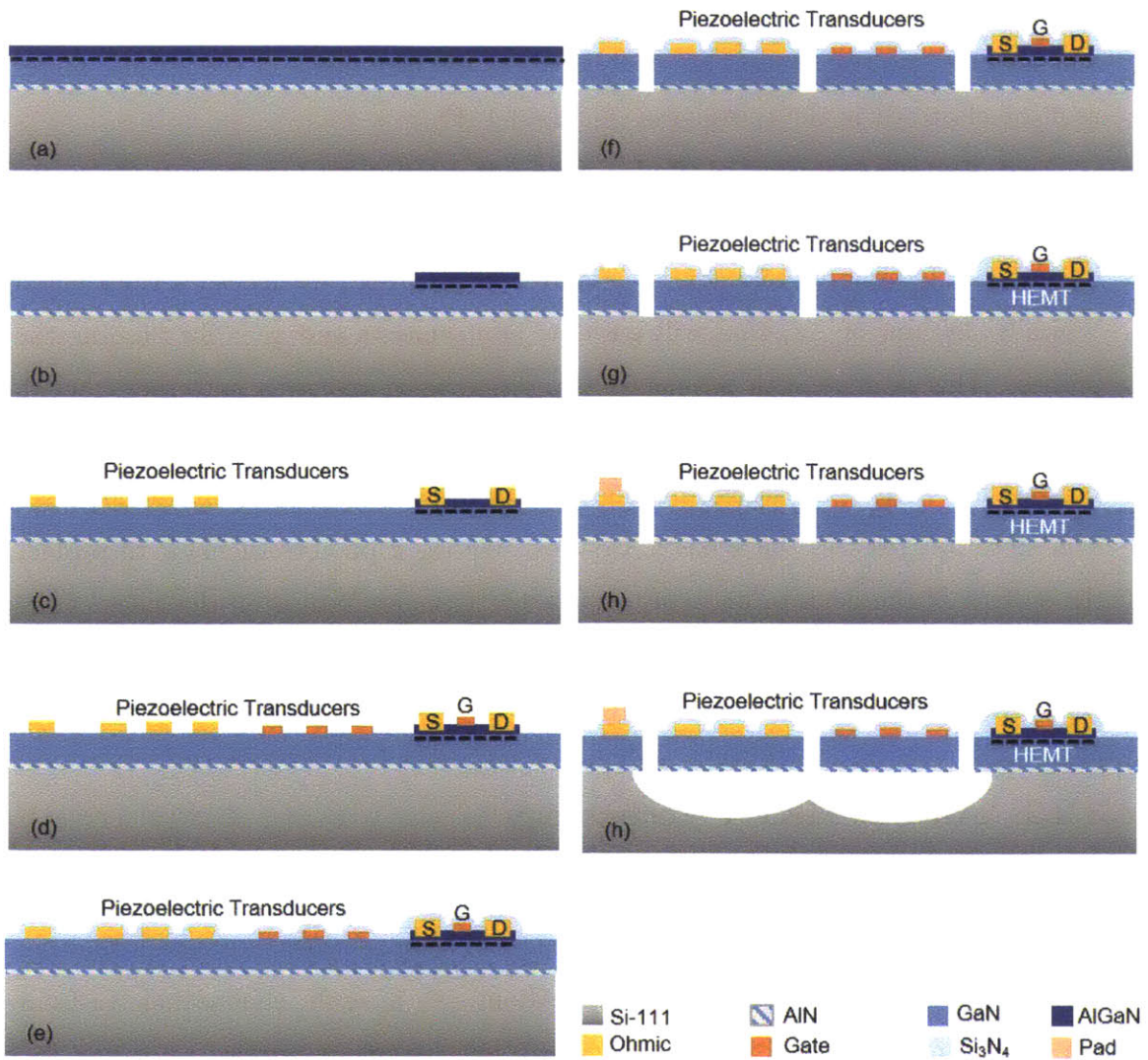


Figure 3-9: Fabrication of GaN MEMS resonators in Au-free HEMT process with only two additional steps.

by phonon-phonon scattering (Chapter 5).

The process flow is similar to the Au-based one described in Subsection 3.2.1. We start with a shallow shallow mesa etch of the AlGaN which is used to remove the 2DEG from everywhere except for the active device area, where HEMTs or piezoelectric transducers will be formed (Figure 3-9 (b)).

One difference between this approach and the process described above is that we proceed with the metalization first and passivate the surface of the active devices, and then pattern the acoustic cavity. This ensures that the surface of the devices is protected earlier in the process, exposing the 2DEG to less damage during the subsequent process steps. The ohmic contact (5 nm Ta/100 nm/20 nm Ta) gets deposited in an ebeam deposition tool and then patterned via lift-off in acetone. We then anneal the sample in a Rapid Thermal Anneal tool for 10 min at 600°. The first thing to note here is that the anneal temperature is much lower than in the Au-based ohmic contact. In fact the two types of contacts are characterized by different physics, as the high temperature anneal leads to direct contact between the 2DEG and the metal at the edge of the contact, while the lower temperature approach is based on a low tunneling barrier underneath the entire contact [70]. Appendix B shows results from the different anneal times and temperatures used during the optimization of the Ta-based ohmic. This lower anneal time leads to better contact surface morphology, edge acuity and definition, which are all requirements for scaling of the HEMT channel [71]. In the case of the MEMS, smoother contacts will eventually lead to less surface scattering and more uniform mass loading, which means higher quality factors. Figure 3-10 shows the difference between the Au-based metalization and the Ta-based one.

Next step is the gate metal deposition and patterning, which is done via ebeam deposition and then liftoff in acetone (Figure 3-9 (d)). The metal of choice here is Nickel (100 nm), motivated by the high work function of this material [72].

Another difference between this process and the previous version is that we are now replacing the gate dielectric deposition with a passivation layer, 200 nm of Si_3N_4 (Figure 3-9 (e)). The purpose of this step is to terminate the dangling bonds at the top surface of the AlGaN layer, which are responsible for traps that lead to the slow

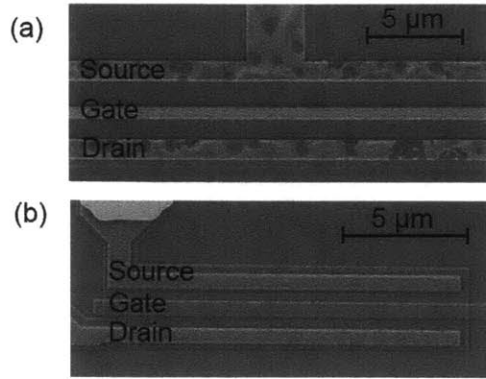


Figure 3-10: SEM images of HEMTs fabricated in a standard Au-based process (a) and in a Au-free process (b).

current degradation [73].

Another purpose of this passivation layer is to protect the metal layers during the GaN deep etch for patterning the acoustic cavities (Figure 3-9 (f).) We can now deposit and pattern a Nickel hard mask as in the previous version of the process, and etch through GaN. After the etch, the nickel mask is removed in a wet etchant. The nitride passivation layer protects the metal gate and ohmic contacts underneath.

The next steps are identical to the first version of the process. We open vias through the passivation layer to make contact to the ohmic and gate metals, using a CF_4 plasma (Figure 3-9 (g)). We then deposit a thick metal pad that is used for landing the probes (Figure 3-9 (h)). While in practice this could be any low-resistance metal, we use 50nm Ti/300 nm Au. Since this metal layer does not get deposited inside the actual cavities, it does not affect the mechanical performance of the resonators. For an eventual integration with CMOS, this layer would have to be replaced with a different one, such as Aluminum or Copper [69].

3.3 Characterization

3.3.1 RF Measurements

Devices are measured in a Cascade probe station, equipped with sensors for recording ambient pressure and temperature values. We use an Agilent Parametric Analyzer to

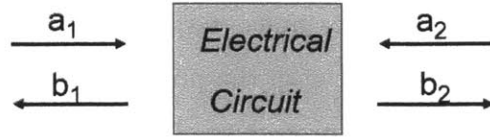


Figure 3-11: S-Parameter Approach for characterizing the response of a 2-Port device. The complex electrical circuit is treated as a "black box" with the terminals acting as the only connection to the external world.

extract the Scattering Parameters (S-Parameters). S-Parameters were first introduced by Vitold Belevitch in 1945 [74]. The electrical parasitics of the cables and probe tips are deembedded using a standard Through-Reflect-Line self-calibration technique. This method treats a complex electric circuit as a "black box", which only interacts with the external world through terminals named "ports". The response of this system is then given by the Scattering matrix, which is defined in terms of the incident and reflected power at the n th port, a_n and b_n , respectively:

$$\mathbf{b} = \mathbf{S}\mathbf{a}. \quad (3.1)$$

Then the S-matrix contains n by n elements, where n is the number of ports. For example, in the case of a 2 Port device as shown in Figure 3-11, the S-matrix is given by:

$$\begin{bmatrix} b_1 \\ b_2 \end{bmatrix} = \begin{bmatrix} S_{11} & S_{12} \\ S_{21} & S_{22} \end{bmatrix} \begin{bmatrix} a_1 \\ a_2 \end{bmatrix}. \quad (3.2)$$

3.3.2 De-embedding

To isolate the characteristics of the device from the capacitive loading associated with the large probe pads, we use a de-embedding algorithm, as described in [75]. We fabricate "Open" devices side by side with the device under test. These are structures where the active device has been removed, and only the pads are present. We measure the S-parameters of the open device and then convert them to Impedance parameters (Z-Parameters). We can then subtract the Z-Parameters of the open structure from

the ones corresponding to the device under test, which is equivalent to eliminating the parasitic capacitance associated with the probe pads used for landing. All data sets shown in this thesis follow this procedure.

3.3.3 Operation in Ambient Conditions

Robust devices require a complete characterization as a function of ambient conditions, such as external temperature and pressure. Both the resonant frequency and the quality factor will be affected by these conditions. Section 2.5 discusses the various damping mechanisms that affect the performance of the resonators, and their dependence on external parameters.

Temperature

Temperature is one of the most crucial parameters to consider when designing resonators for filter and timing applications. Radio applications require the devices to be robust in harsh environments, over a wide range of temperatures. In the case of frequency sources, the specification for the frequency shifts over a temperature range of $-25^{\circ}C$ to $80^{\circ}C$ is less than 50 parts per million (ppm). The response of a resonator to temperature is dependent on both design and choice of resonant modes, as well as on the intrinsic material properties. It is useful to define the Temperature Coefficient of Frequency (TCF) as

$$TCF = \frac{1}{f} \frac{\partial f}{\partial T} = -\frac{1}{L} \frac{\partial L}{\partial T} + \frac{1}{2} \frac{1}{c} \frac{\partial c}{\partial T} - \frac{1}{2} \frac{1}{\rho} \frac{\partial \rho}{\partial T}, \quad (3.3)$$

where L is the length of the resonant dimension of the cavity, c is the relevant elastic constant, and ρ is the density.

Gallium Nitride has a similar temperature coefficient to silicon and Aluminum Nitride. The normalized temperature coefficient of longitudinal and shear velocities were measured to be -12.6 ppm/deg and -6.0 ppm/deg , respectively [76].

3.3.4 Power Handling

A critical requirement for use in broadband radio communications is power handling. One figure of merit for characterizing this is the Third Order Intercept Point, or IP_3 . For a frequency filter with a bandwidth centered at ω_0 , we are concerned with situations when nonlinearities allow two strong out-of-band interfering signals, spaced from ω_0 by $\Delta\omega$ and $2\Delta\omega$ in-band component back at ω_0 , loading the power spectrum at ω_0 [35], as shown in Figure 3-12 (a). These nonlinearities, can be of mechanical nature, i.e. higher order stiffness elements, or piezoelectric nature, as the static piezoelectric coefficients will depend on the strain present in the material. Additionally, under operation, there will be heat generated in the resonator that leads to thermal expansion and modification of the elastic constants. Nonlinear behavior has been studied in other piezoelectric bulk mode resonators, such as AlN [77], [78].

This virtual Third Intercept Point by plotting the output versus input power for the linear case, as well as for the nonlinear product as shown in Figure 3-12 (b). In practice we extract the linear power by exciting at listening at the same frequency, the mechanical resonance frequency. Then, to measure the nonlinear signal, we pick two frequency tones, at $\omega_0 - 2\Delta\omega$ and $\omega_0 - \Delta\omega$, respectively, and then look at the combined output at ω [79].

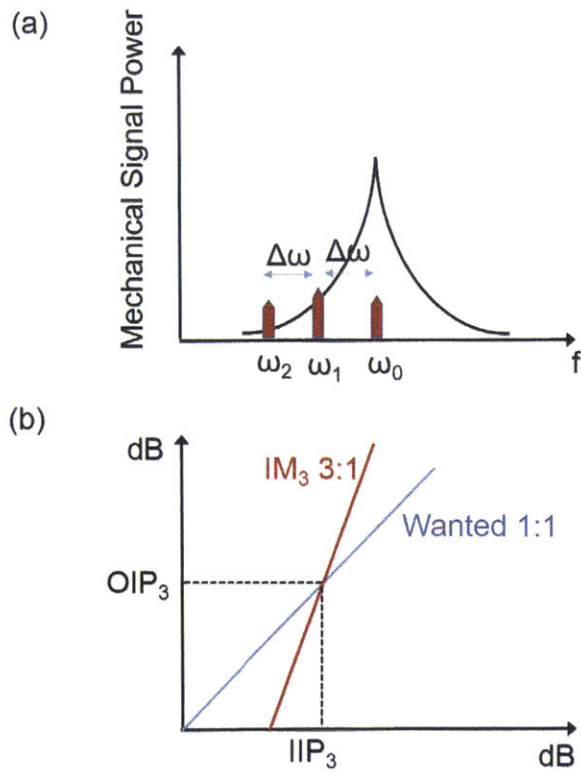


Figure 3-12: Nonlinearity measurement approach. Two strong interfering signals spaced by $2\Delta\omega$ and $\Delta\omega$ will lead to a combined output at the resonant frequency (a). In (b) the Third Order Intercept is defined as the intersection point between the fundamental and nonlinear power outputs.

Chapter 4

2D Electron Gas-Based Transduction

This chapter highlights the unique transduction properties of the GaN HEMT stack, enabled by the presence of a two-dimensional electron gas (2DEG). This high density, high mobility sheet of charge can be used as an electrode for transduction, or to shield electric fields and turn off the acoustic resonance. These properties allowed us to demonstrate the first switchable solid-state piezoelectric resonator [7], as well as the first metal-free GaN resonator [10]. Additionally, the 2DEG in the channel of a HEMT can serve as an active sensor of mechanical vibrations, which will be discussed in Chapter 6. These capabilities can enable truly reconfigurable wireless systems for high frequency communications.

4.1 Motivation

The past decades have seen an increased demand for wireless capabilities, both for consumer and military applications. As a result, the radio spectrum has become increasingly overcrowded, leading to a new paradigm for wireless communications, the concept of reconfigurable or cognitive radio. This would enable a user to scan the radio spectrum and switch to a less crowded frequency channel. Piezoelectric MEMS resonators show a high potential for realizing integrated ultra-compact, frequency-agile and power-efficient radios for these "frequency-hopping" radios.

The most commonly used architecture for the front-end of a channel select radio

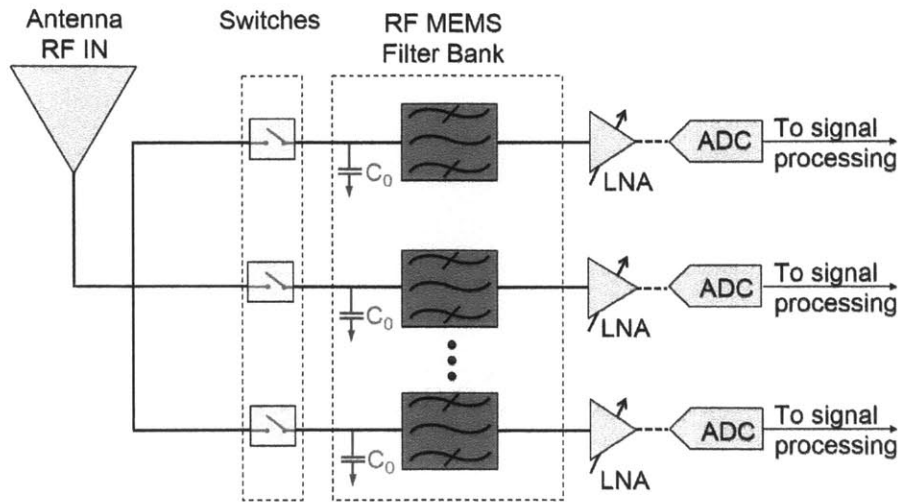


Figure 4-1: Example of possible architecture of the front-end of a radio component using MEMS resonators as filters.

using MEMS resonators is shown in Figure 4-1. An antenna receives the RF signal that is then passed on to a filter bank made of MEMS resonators. For broadband operation, we would like this filter bank to encompass as many channels as possible. In order to reconfigure the system, we need to be able to selectively switch the channels on and off. This is typically done with in-line switches, either solid-state or electromechanical. However, each switch introduces losses, which can be as high as 1 dB in some cases. This will deteriorate the overall noise figure of the wireless system and ultimately limit the total number of channels that can be incorporated.

Piezoelectric resonators realized in GaN MMIC technology benefit from unique acousto-electric properties which allow us to demonstrate switchable resonators with a simple DC bias out-of-line of the RF signal, without the need for in-line switches. There are two approaches to realizing switchable transducers with the help of a conductive electron gas. First, we can use this charge to screen the driving electric fields in the OFF state, and deplete it for actuation in the ON state. Second, we can use the 2DEG as an electrode for transduction in the ON state, and deplete it when we want to turn OFF transduction. These two approaches are discussed in Sections 4.3 and 4.4, respectively.

Finally, we want to interrogate the electromechanical properties of existing epi-

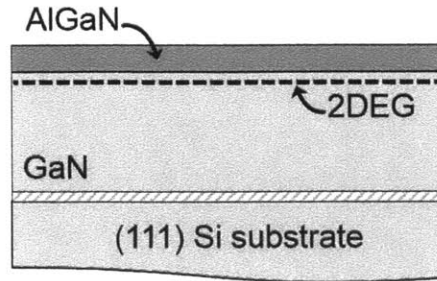


Figure 4-2: AlGaN/GaN heterostructure, grown epitaxially on a silicon substrate, using a thin AlN nucleation layer.

taxial structures to determine what are some of the growth parameters that could be optimized to obtain better resonator performance. We can directly investigate these properties by realizing metal-free resonators, with the help of 2DEG IDTs. This allows us to decouple the electromechanical performance of the semiconductor stack from the additional loss caused by the metal electrodes typically used in piezoelectric resonators. This will be discussed in Section 4.5.

4.2 2D Electron Gases in AlGaN/GaN

We first take a closer look at the properties and source of 2DEG in GaN. The standard GaN-on-silicon cross-section used in this work is shown in Figure 4-2. A thin layer of Aluminum Gallium Nitride is used as a barrier. Contrary to other HEMT technologies such as Gallium Arsenide, where the 2DEG is formed via intentional doping, here the electrons are generated by donor-like surface states, mainly from the top surface of AlGaN [80].

The concentration of 2DEG in the channel can be controlled with an applied voltage using a Schottky contact and it follows the linear charge control approximation. Figure 4-3 illustrates this approach. In the absence of an applied external field, all the charge contributions must be balanced out. These are shown in Figure 4-3 (b). Here σ_P^- and σ_P^- are polarization charges due to the strong piezoelectric fields in the structure, so they will cancel out by definition. Then what is left is the ionized charge due to donor-like surface states, σ_{sur}^+ , and the confined 2DEG. Since the charge is confined

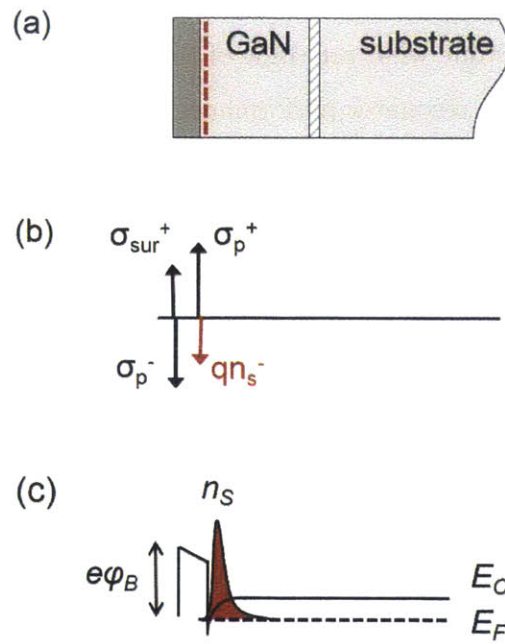


Figure 4-3: (a) Cross-section of AlGaN/GaN heterostructure. (b) Different charge distributions that contribute to the formation of the 2DEG. (c) Energy band diagram, showing confinement of the 2DEG in a potential well at the interface of GaN with AlGaN.

Table 4.1: 2DEG properties for a typical MBE AlGa_N/Ga_N on silicon sample used in this work.

Al content	25	%
AlGa _N thickness	24	nm
Mobility	1.58×10^2	cm^2/Vs
Sheet resistivity	440	Ω/\square

at the interface of Ga_N and AlGa_N, we assume a 1D model:

$$qn_s = C(V_{GS} - V_{th}), \quad (4.1)$$

where q is the elementary charge, n_s is the 2DEG charge density and C is the gate capacitance per unit area and V_{th} is the potential necessary to deplete the 2DEG. If the 2DEG is confined at Δd below the surface, the capacitance is given by

$$C = \frac{\epsilon}{d_{AlGaN} + \Delta d}. \quad (4.2)$$

Here ϵ is the effective dielectric constant between the 2DEG and the top Schottky metal, so it will be mostly given by the dielectric constant of AlGa_N.

The band structure of the AlGa_N/Ga_N heterojunction is shown in Figure 4-3 (c). Then the threshold voltage is given by

$$V_{th} = \phi_B - \frac{\sigma_p \cdot d_{AlGaN}}{\epsilon} - \frac{\Delta E_c}{q} \quad (4.3)$$

and the resulting 2DEG charge density will be given by

$$qn_s = \frac{\epsilon}{d_{AlGaN} + \Delta d} \left(V_{GS} - \phi_B + \frac{\sigma_p \cdot d_{AlGaN}}{\epsilon} + \frac{\Delta E_c}{q} \right). \quad (4.4)$$

Since the 2DEG is formed without the need for intentional doping, there are no additional Coulomb scattering mechanisms, so the mobility of this sheet of charge can achieve really high values. Table 4.1 lists the charge density and mobility for a typical sample used in this work.

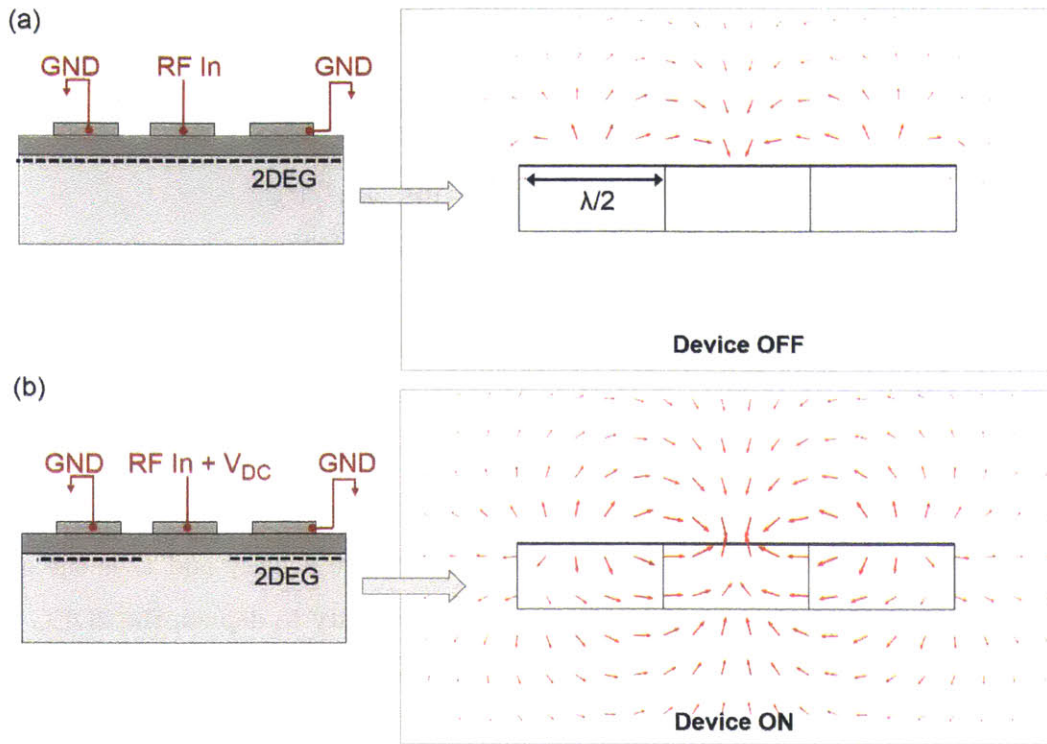


Figure 4-4: Switching of piezoelectric resonators through screening of the electric fields. In (a), the 2DEG under the IDT prevents the electric fields from penetrating the volume of the GaN. By applying a DC bias between the two finger sets in the IDT the 2DEG bunches and gets depleted from under one of the electrode pairs, allowing the fields to penetrate and launch acoustic waves.

4.3 Switchable Piezoelectric Transduction through Screening of the Acoustic Fields

4.3.1 Principle of Operation

As we have seen in the above section, the 2DEG at the interface of AlGaIn with GaN is conductive enough to shield electric fields and keep them from penetrating into the substrate. The ability to control the density of this 2DEG with an applied DC bias opens up the possibility of realizing reconfigurable resonators.

Figure 4-4 illustrates the switching of the resonators through screening of the electric fields. We form an interdigital transducer (IDT) by using the gate metal in a HEMT process, which is discussed in more detail in Section 3.2.2. This transducer

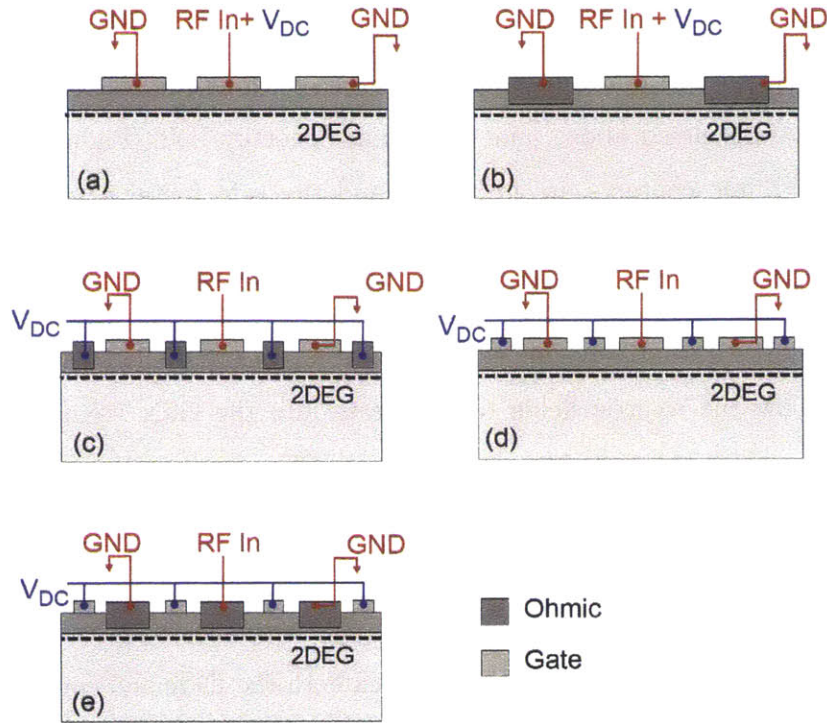


Figure 4-5: Different combination of transducers that can be switched off through the screening of the fields. (a) Schottky-Schottky IDT. (b) Schottky-Ohmic IDT. (c) Schottky IDT with Ohmic control gates. (d) Ohmic IDT with Schottky control gates. (e) Schottky IDT with Schottky control gates.

is formed over the AlGa_N layer, which means that the 2DEG will be present under the transducer, shielding the electric fields in the OFF state. It can be seen in Figure 4-4 (a) that the electric fields are only formed through the air, above the transducer. To turn the device ON, we can apply a DC bias between the two finger sets, which will lead to bunching of the free charge, and the fields will then penetrate through the piezoelectric GaN film, leading to transduction.

This principle has been implemented in Surface Acoustic Wave devices (SAW), where they have been able to demonstrate more than 30 dB suppression of the resonant peak when going from the ON to the OFF states [81].

There are multiple possible configurations of such switchable transducers, as shown in Figure 4-5. These can be classified into two categories: IDTs where the DC bias used for switching is applied to the same electrodes as the RF signal [82], and IDTs

where the DC biasing is applied to separate control gates that are not used to carry any RF signal [83]. The first kind includes devices such as the Schottky metal IDT (Figure 4-5 (a)) discussed above, and an Ohmic-Schottky IDT (Figure 4-5 (b)). In this case the Ohmic contacts are grounded and the gate metal carries the RF in signal, plus a negative DC bias. When the applied DC bias is below the threshold voltage, the 2DEG will be depleted allowing the electric fields to penetrate through the GaN volume. Alternatively, one can use control gates to deplete the surrounding charge and allow the electric fields to penetrate into the GaN volume. This can be realized by using the Schottky metal as an IDT and the Ohmic as a control gate (Figure 4-5 (c)), in which case the DC bias on the control gate needs to be positive. The other configuration uses the Ohmic metal as an IDT and the control gates patterned in Schottky metal (Figure 4-5(d)), with the DC bias needing to be negative. Another possible configuration is when both the IDTs and control gates are made of Schottky metal. Then the applied biases can be either negative or positive, and the free electrons will be bunching, allowing the electric fields to penetrate.

4.3.2 Results

Figure 4-6 (a) shows the SEM image of a fabricated switchable piezoelectric resonator that uses a gate metal IDT. This was fabricated in a Au-free HEMT process, with only two modifications to the standard flow, as discussed in Section 3.2.2. This is a 2-Port device, where we use one IDT embedded in the left side of the cavity to drive acoustic vibrations, and an identical one to sense the waves at resonance. Then the measurement of interest is S_{21} , which is shown in Figure 4-6 (b), for various DC biases applied to the electrode fingers that carry the RF signal. These measurements were taken in vacuum, with an input power of -10 dBm. The measurements are taken with identical DC biasing conditions on both drive and sense transducers. As expected, when the DC bias is 0, the electric fields will be shielded and the transduction will be minimal. As we increase the DC bias, more electrons will bunch away and get depleted from the ground fingers, allowing for stronger transduction. We note that a large jump in the stopband rejection can be seen when going from

4V to 6 V. This is because the threshold potential for this structure is approximately $V_{th} = -4.5 V$, so the 6 V potential difference between the two finger sets will lead to a large depletion region. As expected, the change in stop band rejection will saturate as we go to higher voltages. The $V_{DC} = 6 V$ measurement shows a filter response, with a central frequency of 0.9935 GHz and a fractional bandwidth of approximately 0.9%. The mode shapes of the two resonances that generate this passband response are shown in Figure 4-7. These are symmetric Lamb waves (S_0) that were introduced in Chapter 2. The lower frequency peak corresponds to a mode that is excited uniformly throughout the entire width of the cavity (Figure 4-7 (a)), while the higher frequency mode involves standing waves in the width dimension as well (Figure 4-7 (b)). It can be noted that as we sweep the DC bias conditions we not only change the stop-band rejection, but also the central frequency of the filter and the bandwidth. One explanation behind this phenomenon is the dependence of the elastic constants on strains through the material. As we apply large electric fields through the substrate, these will couple piezoelectrically to strain fields and affect the elastic coefficients.

We also explored the other approach, where the RF signal and the DC biases are applied to different electrodes. Figure 4-8 (a) shows the SEM image of a gate IDT, where serpentine control gates made out of Schottky metal are used to vary the concentration of the 2DEG.

4.3.3 Discussion

We can understand the behavior of both types of devices measured above by looking at a simplified equivalent circuit for a 2 port resonator, shown in Figure 4-9. This model is based on the discussion from Section 2.4.3, where the mechanical resonance was lumped into a series RLC branch. Here, C_0 represents the input capacitance of each of the two transducers, while C_{ft} and R_{ft} are the feed-through capacitance and resistance between the two ports.

For both simple IDT devices and control gate ones, the overall signal floor decreases with the depletion of the 2DEG, which is mainly due to a modification of the feed-through parasitics as the 2DEG concentration changes. This makes this imple-

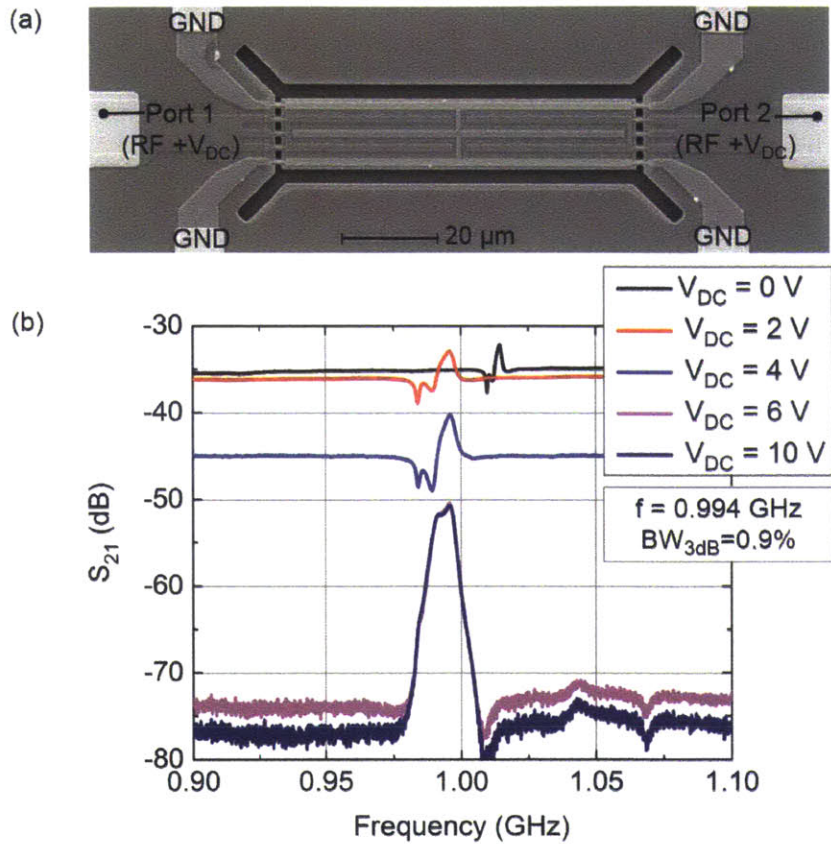


Figure 4-6: (a) SEM image of a switchable piezoelectric resonator with gate IDT. (b) Measured frequency response for different DC biasing conditions applied to the RF signal electrode.

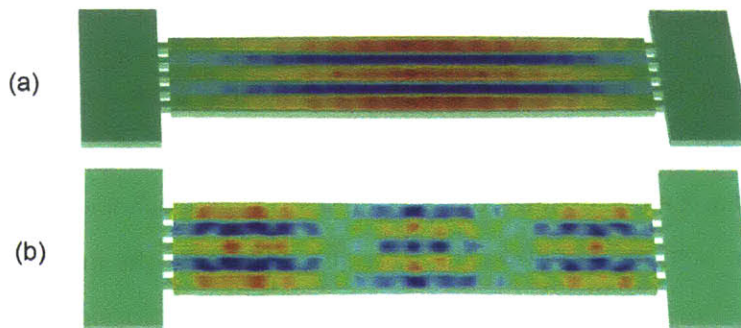


Figure 4-7: Driven Finite element analysis of the 2-Port resonator shown in Figure 4-6. (a) S_0 Lamb mode is excited uniformly through the entire width of the resonant cavity. (b) Standing waves get formed in the width dimension as well, giving rise to harmonics of the S_0 Lamb mode.

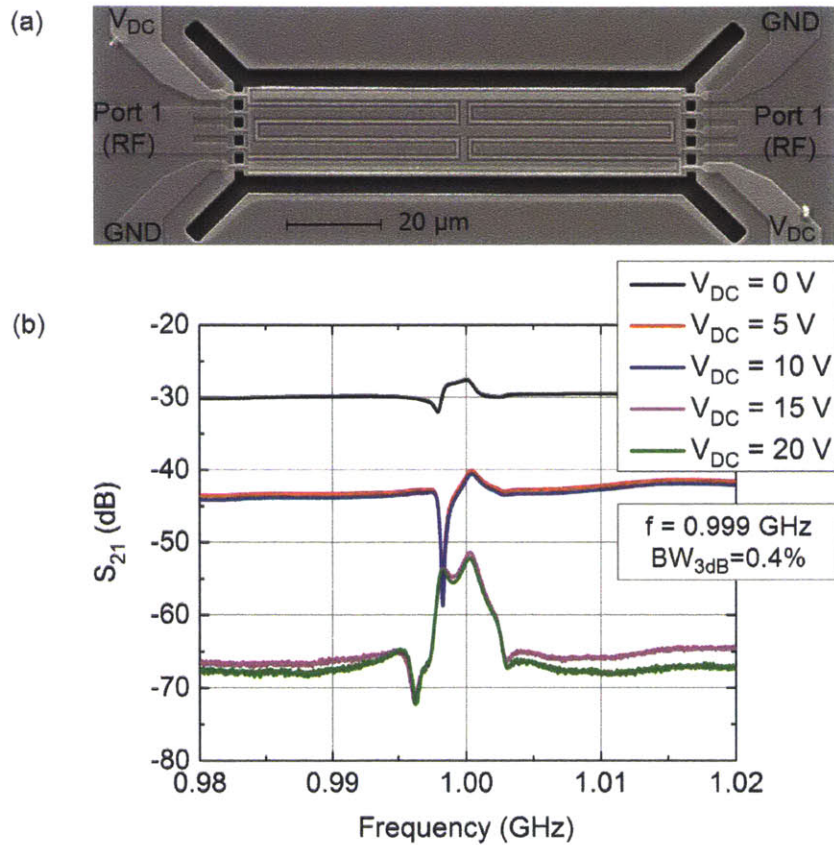


Figure 4-8: (a) SEM image of a switchable piezoelectric resonator with gate IDT and Schottky control gates. (b) Measured frequency response for different DC biasing conditions applied to the control gate.

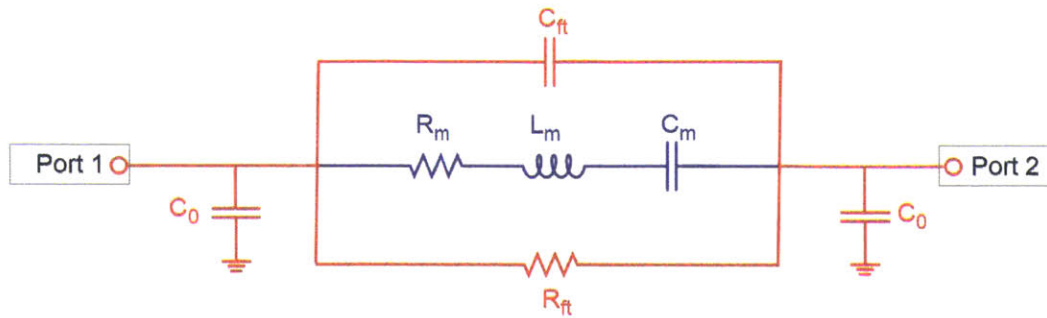


Figure 4-9: Equivalent electrical model for a 2-Port resonator, showing the lumped mechanical branch (blue) and the electrical parasitics (red).

mentation unfeasible for real operation, especially for filter applications. In reality, we would like to have a constant floor, and peak that increases when the 2DEG is depleted. One way to implement this is to better electrically isolate the drive and sense transducers. For example, in SAW devices [82], the input and output transducers are separated by millimeter-long paths, which prevents this bias-dependent floor from happening. One approach that we could take is to embed the drive and sense transducers in separate but mechanically coupled cavities. This approach has been shown to reduce direct electrical feedthrough in the case of active HEMT sensing and it will be further discussed in Chapter 6.

Another important point to make is that the depletion of the 2DEG will also increase the capacitance in the OFF state. In other words, this configuration has large input capacitance in the OFF state and reduced capacitance in the ON state. In practice, for broad-band reconfigurable systems such as the one introduced in Figure 4-1, we would like to be able to reduce the capacitance of one channel when it is not in use. This is what would allow us to have as many channels as possible.

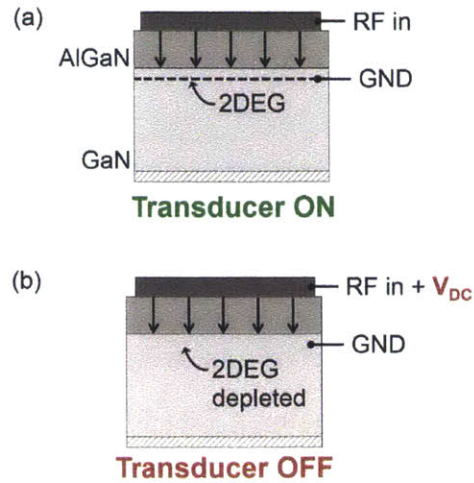


Figure 4-10: Principle of operation of switchable piezoelectric transducer through the depletion of the 2DEG electrode.

4.4 Switchable Piezoelectric Transduction through Depletion of the 2DEG Electrodes

4.4.1 Motivation

The other approach to using the 2DEG for switchable piezoelectric resonators involves patterning it into an actual electrode for transduction. The main motivation for choosing this approach over the one described above is the ability to realize devices with small capacitance in the OFF state, which would allow us to embed more channels in the filter bank for reconfigurable wireless systems.

4.4.2 Principle of Operation

The switchable piezoelectric transducer presented in this work implements a 2DEG electrode as one of two electrodes needed to drive acoustic waves in a resonant AlGaN/GaN stack [84]. 2DEG electrodes have previously been demonstrated as interdigitated transducers in a SAW AlGaN/GaN filter [85] as well as for piezoelectric actuation of AlGaN/GaN heterostructures [86].

To drive acoustic waves in the structure, an AC electric field is applied across

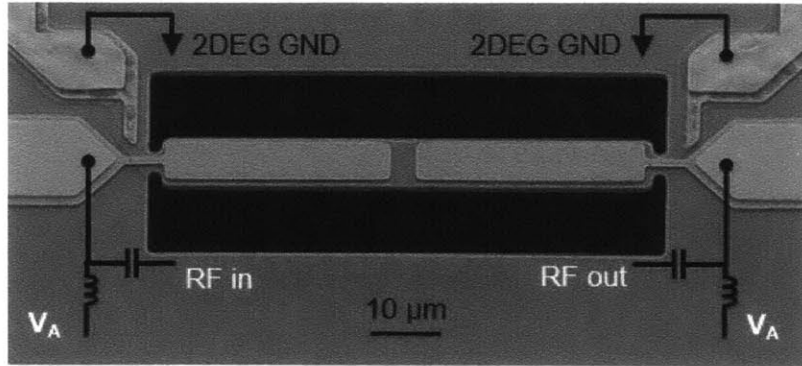


Figure 4-11: SEM of switchable resonator, a $7.3 \times 70 \mu m$ bar with symmetric electrode configuration for drive and sense.

the AlGa_N, between the 2DEG electrode and a Schottky metal contact (Figure 4-10 (a)). By applying a negative bias voltage to the metal electrode above the AlGa_N, the 2DEG can be depleted away (Figure 4-10 (b)). This is the same principle used to switch the conduction channel in AlGa_N/Ga_N High Electron Mobility Transistors (HEMTs). When implemented in an acoustic resonator, the removal of this bottom electrode suppresses electromechanical transduction and serves to reduce the capacitance of the drive transducer by $> 10 \times$ [87].

4.4.3 Results

We fabricate switchable resonators in a HEMT process with only two modifications to the standard process, following the methodology presented in more detail in Section 3.2.1. One such device is shown in Figure 4-11 with symmetric drive and sense transducers. The ohmic contact to the 2DEG electrodes is made outside of the resonant cavity, and then the conductive 2DEG path is routed through the suspension beams.

The measured frequency response of the 2-port piezoelectric resonator shown in Figure 4-11 is presented in Figure 4-12. This device was measured in air in an RF probe station, and de-embedded using an open structure fabricated on the same chip as described in Section 3.3. Two bending modes are detected at 243 MHz and 246 MHz, with Q of 608 and 910, respectively. The insets in Fig. 4 show COMSOL simulations of the displacement fields of these resonant modes. These are antisymmetric

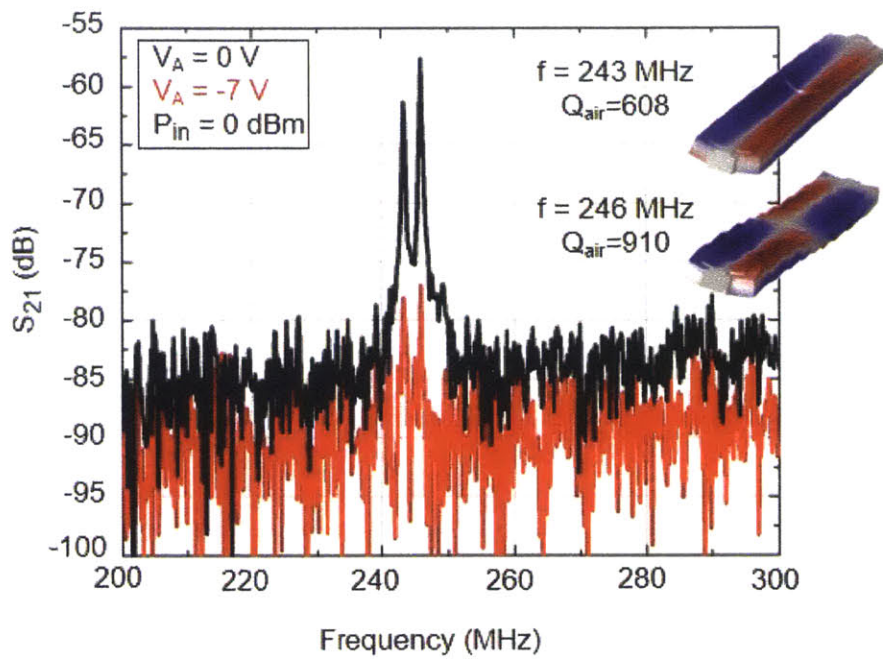


Figure 4-12: Measured frequency response of passive resonator in air, showing 19 dB suppression of the signal when transducer is switched off ($V_{DC} = -7 \text{ V}$).

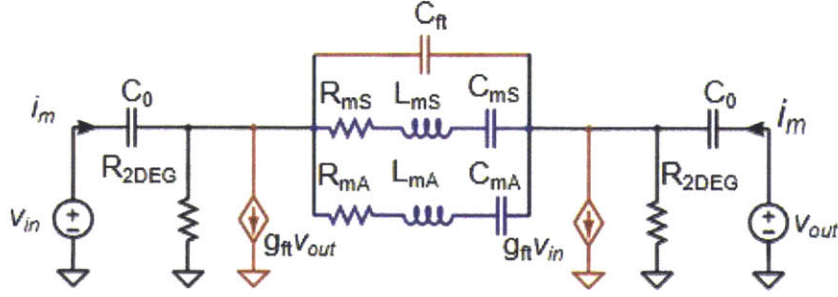


Figure 4-13: Equivalent electrical model for a 2-Port switchable resonator using 2DEG bottom electrodes.

A_0 Lamb modes (see Chapter 2). Applying $V_{DC} = -7$ V to the drive transducer depletes the 2DEG and suppresses the resonance signal by more than 19 dB. This also serves to reduce the drive capacitance C_0 by $13\times$, in close agreement with experimental measurements on AlGaIn/GaN Schottky diodes [87]. For this measurement, the sense transducer remains on to demonstrate the effect of drive suppression alone, but can also be switched off for better isolation.

The small signal equivalent circuit of this resonator is shown in Figure 4-13. The mechanical domain can be modeled by two RLC branches in parallel, corresponding to the symmetric and antisymmetric mechanical modes. The extracted drive capacitance C_0 and the lumped resistance of the 2DEG electrode R_{2DEG} are 390 fF and 3.8 k Ω , respectively. Fitting measured data to the full small signal model in Figure 4-13, R_m of 117.5 k Ω and mechanical Q of 650 are extracted for the symmetric mode, and R_m of 71.3 k Ω and Q of 940 for the asymmetric mode. There are two main contributions to the feed-through signal, including a capacitive contribution of the fringing electrical fields through the substrate, C_{ft} , and a transconductance, g_{ft} . This second contribution can be understood as a modulation of the 2DEG at one port due to a signal applied at the other port. When resonators are scaled for multi-GHz operation, the out-of-band rejection of the transmitted signal is compromised by the increased feed-through floor.

4.4.4 Discussion

This switchable transducer reduces capacitive loading by an order of magnitude when the resonator is not in use, showing high potential for building block for configurable RF filtering in existing MMIC technology. For additional isolation, the sense transducer of these 2-port devices can also be switched.

However, we note that the insertion loss achieved in this devices is too high for operation in an actual system. The first thing to note is that contrary to the approach shown in Section 4.3, these resonators use only the thin AlGa_N layer to transduce waves through the entire volume of the Ga_N stack, which is very inefficient.

Additionally, the MMIC stack has not been optimized for electromechanical operation, so the overall performance of the epitaxial structure might not be what expected from the bulk behavior, both in terms of piezoelectric coefficients and crystalline defects that could lead to lower Q s. The next section discusses ways in which we can directly interrogate the material properties of the epitaxial structure, in the absence of mass loading from the metal electrodes.

Finally, the HEMT process used to fabricate the resonators (Section 3.2.1) uses Au-based electrodes, which will lead to loading and damping of the modes. In Chapter 5 we take a closer look at the performance of Ga_N resonators in a Au-free process, obtaining mechanical quality factors as high as 8000 at 2 GHz, leading to the highest $f \cdot Q$ products measured in Ga_N resonators to date.

4.5 Metal-Free Piezoelectric Resonators

4.5.1 Motivation

The Ga_N MMIC stack has been optimized for the RF and optoelectronic market, with very limited attention to the great potential of harnessing the electromechanical benefits of Ga_N. Although there are various methods for growing crystalline Ga_N, the two most popular techniques are molecular beam epitaxy (MBE) and metalorganic chemical vapor deposition (MOCVD) [63]. Silicon is the obvious choice for growth

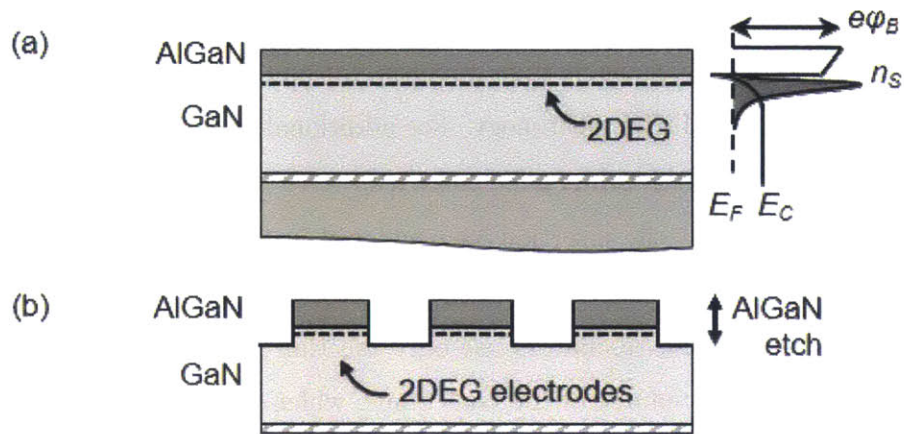


Figure 4-14: 2DEG IDT resonators are realized starting from the AlGaIn/GaN heterostructure (a) by patterning 2DEG electrodes are patterned via a shallow AlGaIn etch (b).

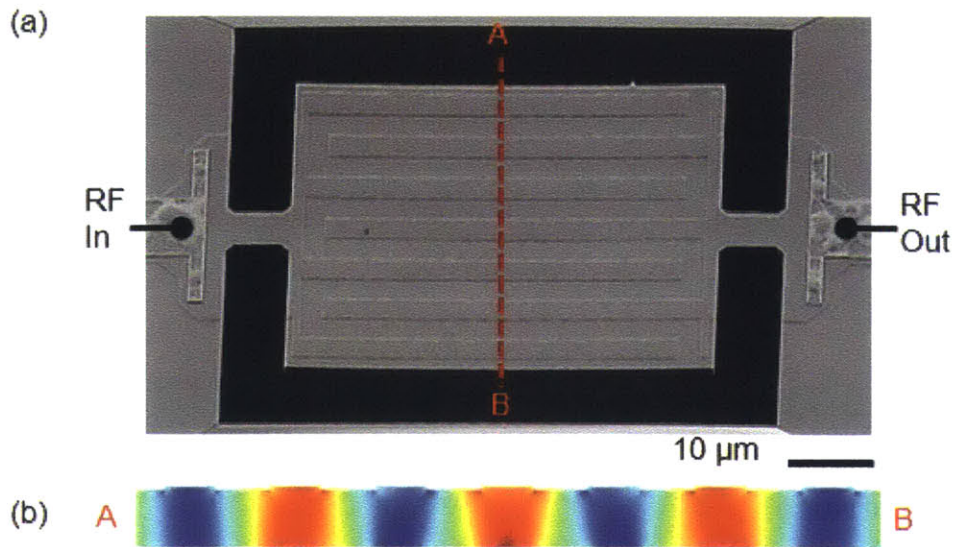


Figure 4-15: (a) SEM of GaN resonator with 2DEG IDT. The 2DEG electrodes are patterned with a 70 nm deep AlGaIn etch. Ohmic contacts are used to access the 2DEG outside of the resonant structure. (b) Strain fields of the bulk contour mode excited using the 2DEG IDT.

substrate, enabling a simple release of membranes and cantilevers. However, when cooling down from high growth temperatures ($800 - 1100^{\circ}\text{C}$), GaN and the (111) Si substrate compress at different rates due to different thermal expansion coefficients, leading to residual stress in the GaN film. In the case of released structures, this can affect the mechanical properties of the resonators and even lead to cracking and breaking. Additionally, the large dislocation density region at the bottom of the GaN film can lead to scattering and, as a result, low quality factors as well as lower piezoelectric transduction efficiency.

In order to isolate the intrinsic mechanical properties of GaN, it is necessary to minimize other loss mechanisms that limit the Q of a MEMS resonator, as discussed in Section 2.5. A study of this fundamental limit is required to interrogate the acoustic performance of various GaN growth processes. However, most piezoelectric transducers are realized using metal electrodes. Metal electrodes result in added acoustic losses, and contribute to mode distortion through mass loading. In AlN, efforts to minimize losses associated with metal in piezoelectric resonators have included physically separating the electrodes from the piezoelectric film [88] and segmentation of IDT metal electrodes [89]. In GaN, the standard MMIC platform provides a metal free conductive sheet inherent to the heterostructure, which can be used to define electrodes, eliminating the metal completely from the resonant structure.

4.5.2 Principle of Operation

The piezoelectric resonator presented here uses 2DEG IDTs to drive acoustic waves in an AlGa_N/GaN heterostructure. 2DEG electrodes have previously been demonstrated as IDTs in a SAW AlGa_N/GaN filter [85]. However this is the first use of 2DEG IDTs in MEMS resonators.

Figure 4-14 (a) shows the cross-section of the typical starting epitaxial structure for a 2DEG IDT resonator. The 2DEG can then be patterned with a shallow AlGa_N etch as shown in Figure 4-14 (b). To drive acoustic waves in the structure, an AC electric field is applied through the GaN, between the interdigitated 2DEG electrodes.

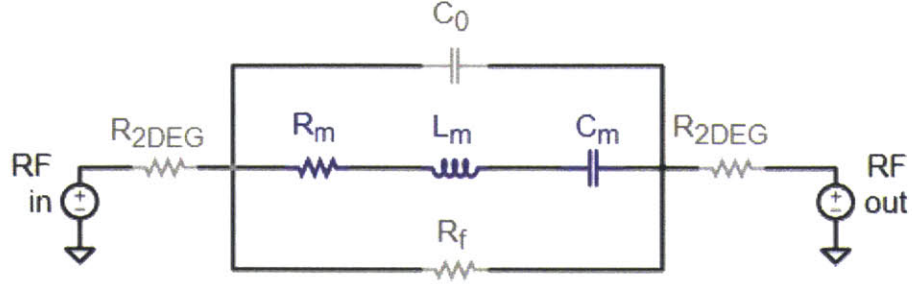


Figure 4-16: Equivalent circuit model of 2DEG IDT. Elements in blue represent the mechanical resonance while elements in grey are electrical parasitics of the structure and are deembedded from the measurement.

4.5.3 Results

Devices were fabricated using the procedure detailed in Section 3.2.1. A GaN Lamb-wave piezoelectric resonator using a 2DEG IDT is shown in Figure 4-15 (a), with the simulated resonant mode shape shown in Figure 4-15 (b). This structure corresponds to “Design A”, with dimensions $50 \times 65 \mu\text{m}$ and using quarter wavelength suspension beams to minimize anchor losses. For comparison, an identical resonator using Ohmic metal IDTs is also fabricated.

Devices were tested under vacuum to reduce air damping. The parasitics of the RF pads were deembedded using an open structure. Since the goal of this work is to isolate the mechanical performance of the AlGaIn/GaN resonators, further deembedding needs to be performed to eliminate electrical parasitics, especially the loss associated with feed-through capacitance and the series resistance of the 2DEG. The equivalent circuit describing this device is captured by Figure 4-16. The electrical parasitics to be deembedded are represented in grey. After parameter fitting was performed to extract C_0 , R_f , and R_{2DEG} , these contributions were deembedded from the admittance of the device, leaving only the mechanical response shown in Figure 4-17 (a). The measured deembedded frequency response of the resonator with Ohmic metal IDT is shown in Figure 4-17 (b). The mechanical quality factor of the device with metal electrodes is $3\times$ lower than that of the 2DEG IDT, which can be attributed to the additional mass-loading and damping mechanisms associated with metal electrodes.

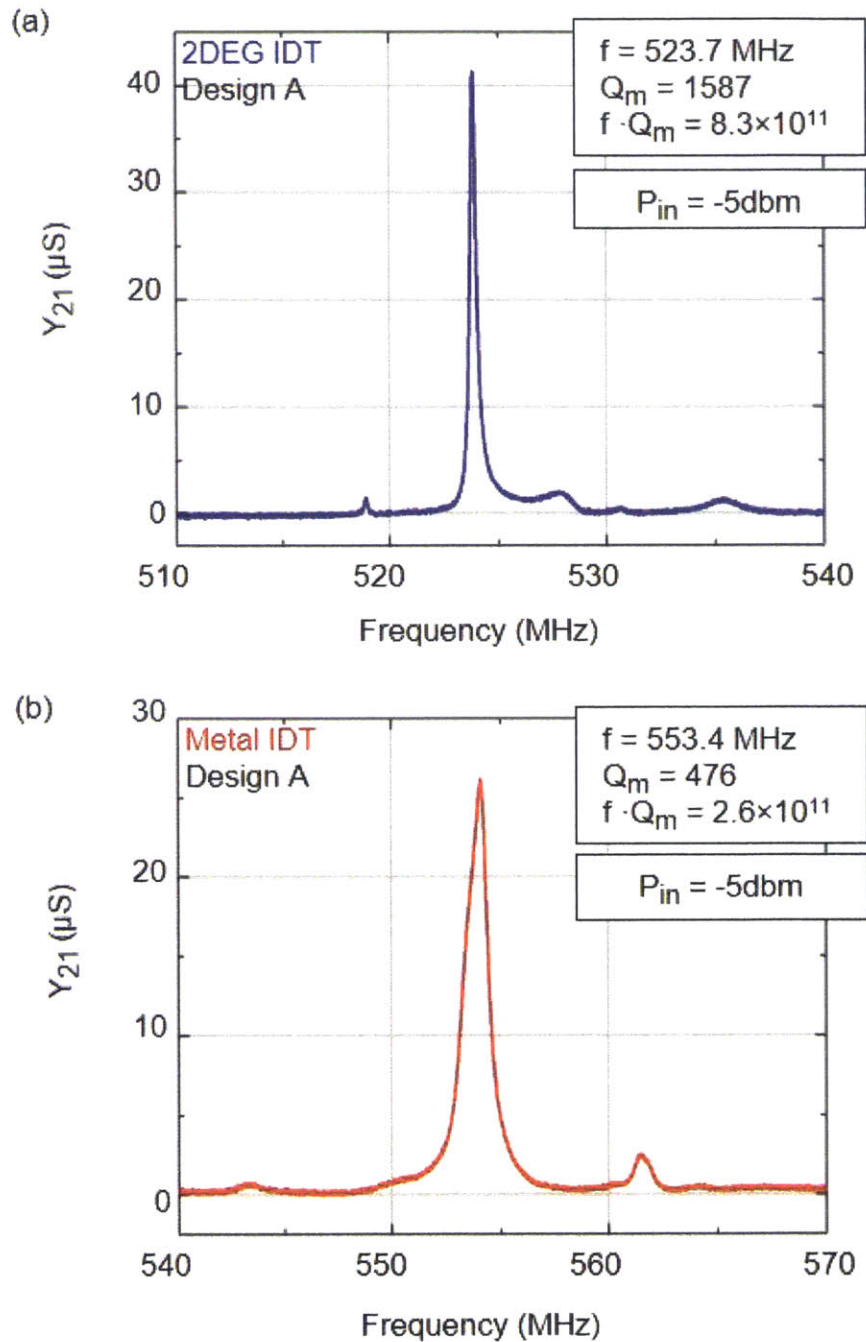


Figure 4-17: (a) Frequency response of “Design A” resonator using 2DEG IDT after deembedding the electrical parasitics. (b) The deembedded measured response of a metal IDT resonator with equivalent design.

Table 4.2: Comparison of Metal and 2DEG IDT Resonators.

		f (MHz)	Q_m –	fQ_m (s ⁻¹)	k_{eff}^2 (%)
Design A	2DEG	523.7	1587	8.3×10^{11}	0.091
	Metal	553.4	476	2.6×10^{11}	0.095
Design B	2DEG	525.3	1193	6.3×10^{11}	0.08
	Metal	516.4	460	2.3×10^{11}	0.05

Table 4.2 summarizes the extracted mechanical Q and $f \cdot Q$ products for two resonator designs, each measured using 2DEG IDTs and metal IDTs. As mentioned above, “Design A” resonators use quarter wavelength suspension beams. In the case of “Design B”, a phononic crystal is used to mechanically isolate the resonant mode. In both cases, the Q of the 2DEG IDT device is significantly higher than that of the metal IDT.

4.5.4 Discussion

This section has introduced and demonstrated a GaN piezoelectric resonator that uses 2DEG electrodes to drive and sense acoustic waves. This resonator is metal-free, enabling the intimate interrogation of GaN material properties, in the absence of losses and distortions associated with metal electrodes. However, it is important to mention that these devices are not suitable for operation, as the series resistance associated with the 2DEG electrode fingers will severely reduce the quality factor of the frequency response. Nevertheless, since this work was realized in a standard MMIC heterostructure, with only two modifications to the HEMT process flow it shows high potential of 2DEG electrodes for benchmarking the electro-mechanical properties of GaN for material optimization.

Chapter 5

Lamb-Mode Resonators in GaN MMIC Technology

5.1 Motivation

Chapter 4 discussed the unique transduction capabilities of the AlGa_N/Ga_N platform as enabled by the presence of an inherent 2DEG, which could eventually enable reconfigurable systems and the study of new physical phenomena. Since most of the Ga_N technology development has been driven by RF electronics applications, and due to the benefits of having integrated MEMS resonators with high power, high-frequency electronics, this chapter presents a detailed study of the design of MEMS resonators within the constraints of the Ga_N Monolithic Microwave Integrated Circuit (MMIC) platform [90].

There are two main goals to this study. First, we want to maximize the performance of the resonators with as little modification to the Ga_N High Electron Mobility Transistor (HEMT) process as possible. Second, we want to interrogate the electromechanical performance of the HEMT stack (both Ga_N film and available metalization) and determine the feasibility of this technology for realizing high performance resonators, seamlessly integrated with Ga_N electronics.

In a monolithically integrated solution, various constraints of the technology must be considered when optimizing the design of the MEMS resonators. There are three

key considerations by which we optimize our design.

GaN Film Thickness

As discussed in Chapter 1, the growth of GaN has been primarily driven by the optoelectronic market, as well as the potential for high-power, high-frequency electronics. As a result, the thickness and composition of the films have been optimized for the best performance within these areas. In the case of the MMIC stack, the growth parameters are set to maximize charge density and mobility at the interface of GaN with a top AlGaIn layer, where the channel of a HEMT is formed. In the case of MEMS resonators, the thickness of the GaN film constrains the design space, in terms of the acoustic modes and frequency ranges that can be excited in these cavities. Even in the case of contour modes, i.e. modes with frequencies mainly depending on the lateral dimensions of the cavity, there will be a weak dependence of the frequency on the thickness of the cavity, and the transduction efficiency will depend on the ratio between the wavelength and thickness.

Residual Stress and Crystal Imperfections

As discussed in Section 4.5, when cooling down from high growth temperatures (800–1100°C), GaN and the (111) Si substrate compress at different rates due to different thermal expansion coefficients, leading to residual stress in the GaN film. In the case of released structures, this can affect the mechanical properties of the resonators and even lead to cracking and breaking. Careful design of the resonant cavities and anchors can alleviate these issues.

Available Metalization Layers

Due to the epitaxial growth process and RF requirements of the substrate, MMIC technology prohibits the use of bottom electrodes, more commonly found in sputtered piezoelectric materials, (e.g. AlN). While bottom electrode configurations can be realized through postprocessing [8], these additional steps would lead to extra cost, reduced yield, and lower resonator quality factors.

5.2 GaN Lamb-mode resonators

Given the design considerations mentioned above and the goal of being able to achieve multiple frequencies on the same chip with one single photo-lithographic step, we investigate the potential of realizing piezoelectric Lamb wave resonators. As discussed in Chapter 2, Lamb-wave resonators are an attractive alternative to SAW and FBAR for high-frequency filters and oscillators, due to their large phase-velocities and small frequency sensitivity to process variations such as film thickness.

The zeroth order symmetric and anti-symmetric modes, S_0 , and A_0 , respectively are shown in Figure 5-1. The most common method of launching and detecting this family of modes is using an interdigital transducer, as discussed in Chapter 2. Figure 5-2 shows two of the most common IDT configurations used in Lamb-mode resonators. While the first configuration, that uses a top-metal electrode only, is easier to fabricate in an integrated solution, the addition of a bottom electrode in (b) has the advantage of a more efficient electromechanical transduction [91].

In order to design high performance resonators, we first study the theoretical transduction capabilities present in our material stack. First, we desire to decouple the influence of metal loading of the resonators from the ideal performance of the piezoelectric GaN film, which would be the ultimate achievable limit in this technology. So we choose to simulate the piezoelectric film in the absence of metal electrodes. To still be able to compare the transduction characteristics of the two types of transducers shown in Figure 5-2, we use a massless electrode approach [92, 93] that was discussed in Subsection 2.3.5.

We employ a 2D Finite Element Analysis simulation in Comsol to extract two of the performance metrics of interest, the phase velocity and the theoretical electromechanical coupling coefficient, k^2 , which was first introduced in Section 2.3. The theory behind this simulation follows the matrix method, described in detail by Adler [94]. The main goal is to quantify the change in phase velocity as the wave propagates through the piezoelectric film, under different electrical boundary conditions. To do this, we use Eigenmode analysis in the Comsol Piezoelectric Module to extract the



Figure 5-1: Cross-section of an infinite plate of finite thickness, h_{GaN} shows the first two Lamb modes propagating in the x -direction. The zeroth order symmetric Mode, S_0 , is shown for a normalized wavelength $\lambda/2d = 4.3$. The mode shape of the zeroth order antisymmetric mode, A_0 is shown for a normalized wavelength $\lambda/2d = 6$. Arrows represent the displacement fields, while the color maps the strain fields.

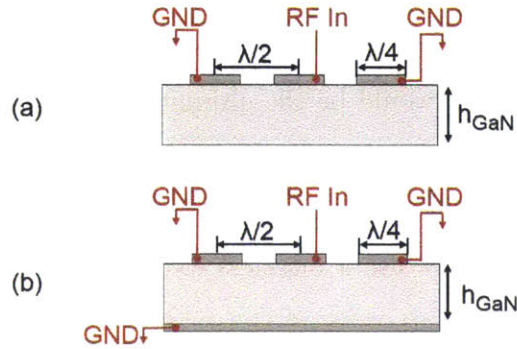


Figure 5-2: Typical interdigital transducer configurations (IDT) used to drive and sense Lamb waves. (a) uses a single metal layer at the top of the piezoelectric film to induce a periodic electric field through the substrate. (b) includes an additional bottom electrode that can be grounded to confine the electric fields in the piezoelectric field.

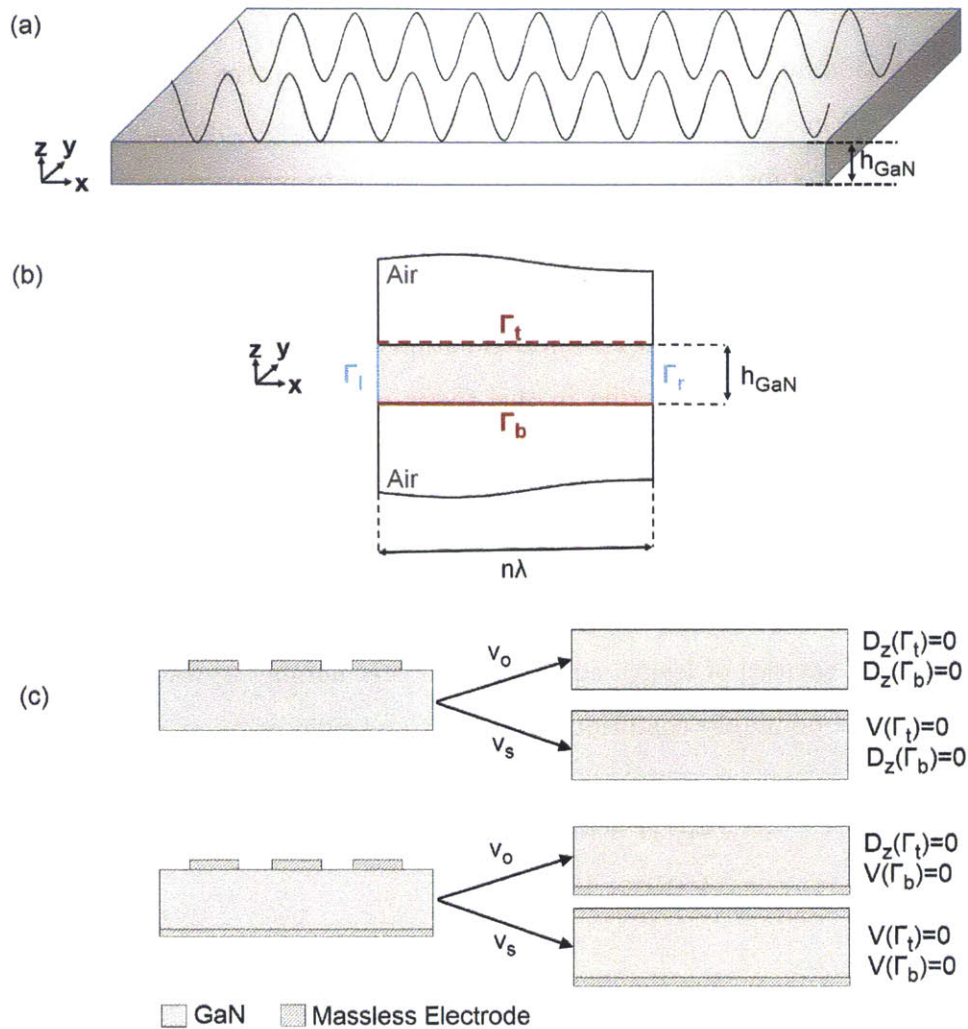


Figure 5-3: (a) Guided Lamb-modes propagate in the x -direction in an infinite plate of thickness h_{GaN} . (b) Unit cell used in FEM analysis to extract eigenmodes. (c) Electrical boundary conditions used to extract v_0 and v_s for the two IDT configurations.

eigenfrequencies, f , of the modes of interest for a particular wavelength λ and we then compute the phase velocity as:

$$v = \lambda f. \quad (5.1)$$

We start by considering a traveling Lamb wave propagating in the x direction in an infinite plate of thickness h_{GaN} , as shown in Figure 5-3 (a). The boundary conditions discussed in Chapter 2 for this family of modes allows us to reduce the problem to a 2D building unit cell (Figure 5-3 (b)). Here, we assume no displacements or variations of any physical quantities in the y direction, so we can limit the problem to the sagittal plane zx by using the Plane Strain 2D approximation method in Comsol. Given that the materials that we are considering in this thesis have a relatively low dielectric constant, it is important to include an air-box around the piezoelectric material to model the electric fields and potential correctly. However, this air region can be treated solely as an electrical domain, since its low mechanical stiffness will not affect the acoustic fields. To reduce the computation power requirements we define a unit cell by considering cavities of length equal to an integer number of wavelengths, i.e. by defining periodic boundary conditions at the left and right edges of the geometry:

$$u_i(\Gamma_l) = u_i(\Gamma_r), \quad i = x, z \quad (5.2)$$

$$V(\Gamma_l) = V(\Gamma_r), \quad (5.3)$$

where u_i are the displacements fields and V is the electric potential. The top and bottom edges of the piezoelectric domain are then set as traction-free boundaries, consistent with the Lamb-mode propagation discussed in Chapter 2.

Next, we want to differentiate between the two IDT configurations discussed above. In the case of the top-metal-only IDT, the bottom surface is set to a zero-charge/symmetry condition ($D_z(\Gamma_t) = 0$), while for the bottom-electrode configuration we set $V(\Gamma_b) = 0$ to simulate the presence of a massless, infinitesimally thin metal. To extract the phase velocity in the free case (v_0) we define a zero charge

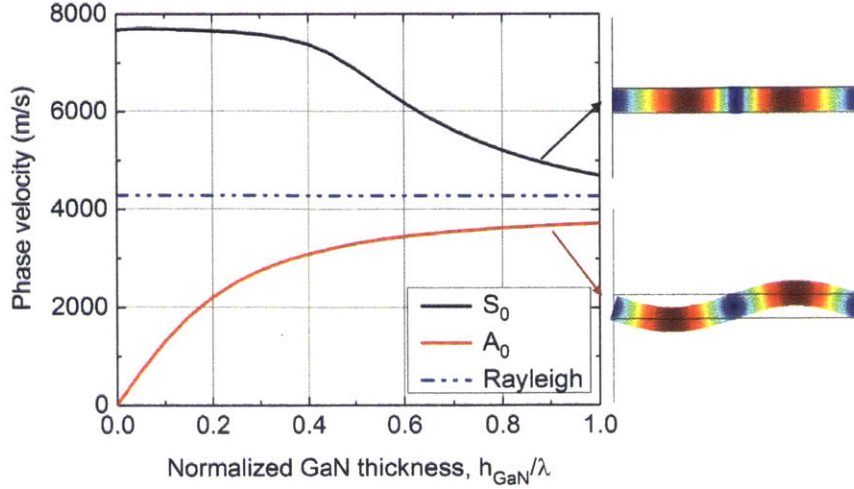


Figure 5-4: Phase velocity dispersion curve for the first Lamb modes, A_0 and S_0 assuming massless electrodes of infinitesimal thickness. The phase velocity corresponding to Rayleigh waves in GaN is overlaid for comparison [6]. Insets show mode shape, with the color map corresponding to the displacement field.

boundary condition on the top surface, while in the case of the electrically shorted surface we set the electrical potential of the top surface to zero, which will allow us to compute v_s .

The first performance metric is the phase velocity that can be achieved in these structures or, more specifically, the dispersion relation. Figure 5-4 shows the simulated phase velocity for the two IDT configurations, as a function on the normalized GaN thickness, h_{GaN}/λ . The GaN material properties used in this simulation are listed in Table A.1. For comparison, we overlaid the simulated Rayleigh wave dispersion curve for GaN [6]. We notice a very similar behavior as in the case of AlN Lamb-mode resonators [91], as expected given that both materials belong to the wurtzite crystal symmetry class. It can be observed at once that the phase velocity of the symmetric mode is larger than the SAW velocity and that, for large normalized wavelengths ($h_{\text{GaN}}/\lambda < 0.4$), the symmetric mode shows a relatively dispersion-free behavior. Both symmetric and antisymmetric dispersion curves converge towards the Rayleigh velocity as the wavelength becomes comparable to the film thickness.

To compare the intrinsic electromechanical coupling efficiency of these different

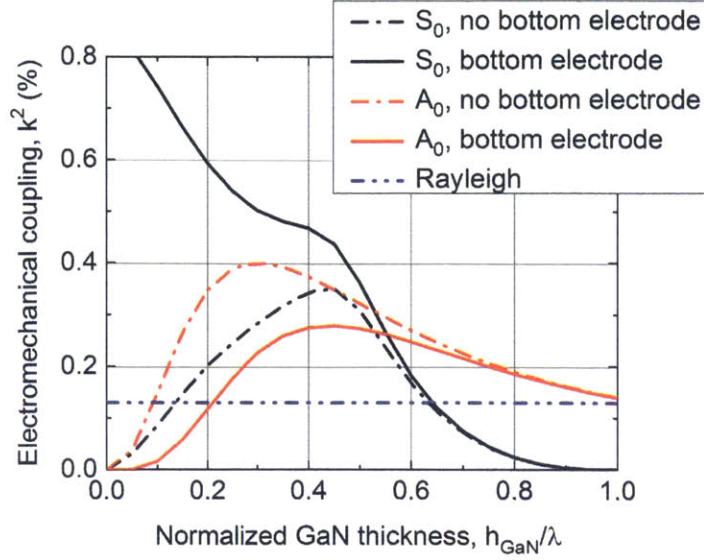


Figure 5-5: Simulated intrinsic electromechanical coupling efficiency, k^2 of S_0 , and A_0 , respectively. The efficiency of a Rayleigh SAW propagating in GaN is also included for comparison [6].

modes, we calculate k^2 which was shown in Section 2.3.5 to be:

$$k^2 = 2 \frac{v_0 - v_s}{v_0}, \quad (5.4)$$

using the phase velocities extracted from the FEA simulation in Figure 5-3. A plot of k^2 for both A_0 and S_0 , for the two IDT configurations introduced earlier is shown in Figure 5-5.

Based on the findings in Figures 5-4 and 5-5, we focus on the symmetric mode due to its higher phase velocities and flatter dispersion curve, relative to the antisymmetric mode. Although the bottom-electrode IDT configuration would offer a higher electromechanical coupling coefficient, we chose to design zeroth order (S_0) Lamb-wave resonators driven piezoelectrically with a top metal interdigital transducer and no bottom electrode. This choice is mainly driven by the desire to achieve high performance in a fully integrated solution, without major modifications to the HEMT process. Additionally, this design has the advantage of higher Q relative to bottom-electrode devices, since an additional metal electrode would lead to mass loading,

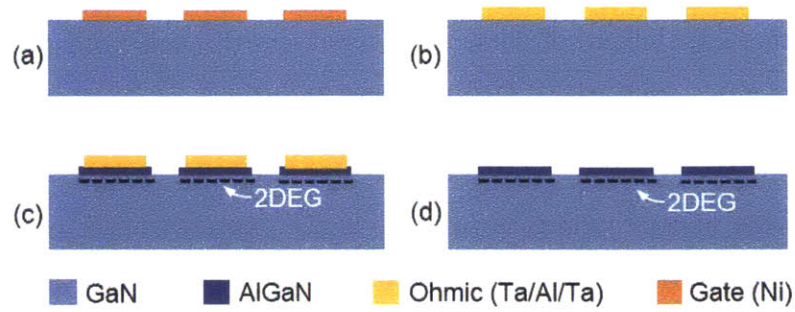


Figure 5-6: Different IDT configurations that can be realized in a GaN-HEMT process using: (a) the gate metal, (b) the ohmic metal, (c) ohmic metal over patterned 2DEG electrodes and (d) 2DEG electrodes only.

distortion of the mode and increased acoustic loss through interfacial scattering as discussed in Chapter 2.5. In AlN Lamb-mode resonators operating in a similar frequency range, the quality factor of the device using a bottom electrode was almost $4\times$ lower than of an equivalent device with top-IDT drive [91].

5.3 Implementation in GaN MMIC Technology

As mentioned previously, one of the goals of this study is to realize high performance GaN resonators integrated with HEMTs, with as little modification as possible to the MMIC process. While this puts some constraints on the final MEMS structure (i.e. no bottom electrodes), it also offers various metal layers for piezoelectric transduction of the acoustic waves, as pictured in Figure 5-6. These include the Schottky metal used to form the gate of the transistor and the ohmic metals used for accessing the source and drain regions of the transistor. Additionally, we can explore IDTs formed out of ohmic metal in contact with patterned 2DEG, and also the 2DEG itself. The use of the 2DEG for metal-free resonators is discussed in more detail in Section 4.5. While this type of IDT provides an excellent way for directly interrogating the material properties of the MMIC epi in the absence of metal loading, the series resistance of the 2DEG fingers reduces the performance at high-frequency significantly, making it not suitable for operation.

In this chapter we focus on the metal based IDTs, with the goal of characterizing

the transduction capabilities of these different layers through both simulation and direct experimental verification. Details about the metal stacks used in this study can be found in Chapter 3 and in Appendix A.

To gain some understanding as to what is the expected effect of mass-loading in each of these transducers, we choose to simulate the frequency response, using the approach illustrated in Figure 5-7 (a). It is important to note that the actual epi structure used here includes a thin layer of AlN at the bottom, used for lattice matching between GaN and Silicon during growth. This nucleation layer is included in the simulation. The nitride passivation layer is also included in the simulation. We assume an isotropic loss factor of $1/Q_{sim}$, where we take $Q_{sim} = 3000$ to be in the middle of range of electrically loaded quality factor values found experimentally (see Section 5.4). Similar to the eigenvalue simulation introduced in Section 5.2, we define periodic boundary conditions at the edges of the unit cell, Γ_l and Γ_r , and we include an airbox to account for the fringing of the electric fields outside of the resonator. The simulated electric fields and potential can be seen in Figure 5-7 (b). We don't solve the electrostatics problem inside the gate domain, which is defined as a metal. To account for mass loading, we now include the transducer electrodes, as well as the nitride passivation layer. The layer defined as Electrode in the simulation will have different material properties and thickness, depending on whether we are simulating the gate transducer or the ohmic one. In the case of the ohmic with patterned 2DEG, this domain will include the thin AlGaIn layer, a thin ($\approx 50 \text{ nm}$) GaN layer which is patterned as a result of an overetch into the substrate, and then the ohmic metal. The material properties of the ohmic alloy used in this run are calculated in Appendix A. To extract the admittance of this structure, we then ground one of the fingers, and define a terminal to the other one. This simulated admittance is shown in Figure 5-7 (c) for a normalized GaN thickness $h_{GaN} = 0.3$. The corresponding mode shape at the mechanical resonance can be seen in (d). From this simulation we fit the data to an RLC mechanical branch in parallel with the capacitance C_0 , as shown in the inset of Figure 5-7 (d), neglecting other electrical parasitics that are not included in this model. The resulting phase velocity and effective transduction efficiency are shown

in Figure 5-8.

5.4 Experimental Results

We fabricate these resonators at MIT using Raytheon’s standard MMIC GaN heterostructure, comprised of Molecular Beam Epitaxy (MBE) AlGaN(25 nm)/GaN(1.7 μm) on (111)-Si as discussed in more detail in Chapter 3. The fabrication process involved a subset of a GaN HEMT flow with only two additional steps, illustrated in Figure 5-9. More details about the process flow are included in Chapter 3. Processing starts with a shallow AlGaN etch which removes the 2DEG to allow for transduction through the volume of the entire GaN film. For the 2DEG-based devices (Figure 5-6 (c)), this etch is used to pattern the 2DEG under the electrodes. The ohmic and gate metals of the transistor are then used to define piezoelectric IDTs. Since these devices are processed side by side with GaN HEMTs, a PECVD Si_3N_4 layer ($\approx 200\text{nm}$) is deposited to passivate the surface and protect the 2DEG channel. Metal pads are then connected to the ohmic and gate electrodes through vias in the passivation layer. The two modifications to the HEMT process involve: a deep GaN etch to define the acoustic cavities (Figure 2-10 (c)), and a final isotropic silicon etch to release the resonators (Figure 5-9 (d)). This is the first time when MEMS resonators were fabricated in a Au-free HEMT process flow. While typical HEMT MMIC processes use Au electrodes to make contact to the 2DEG channel and for low-resistance transistor gates, many efforts have been made to realize Au-free metallization schemes in order to allow for the integration of GaN MMICs in CMOS foundries [32]. Eliminating Au-electrodes from the resonators also allows for higher resonator quality factors, since Au is known to lead to additional dissipation through mass-loading, phonon-electron scattering and interfacial losses. The choice of metallization for this process is discussed more in Chapter 3. Additionally, a list of mechanical material properties of these various metal layers is tabulated in Appendix A.

Figure 5-10 (a) shows the SEM image of a fabricated S_0 Lamb mode resonator. This particular device is a 5th harmonic 1 GHz S_0 mode using the gate metal from

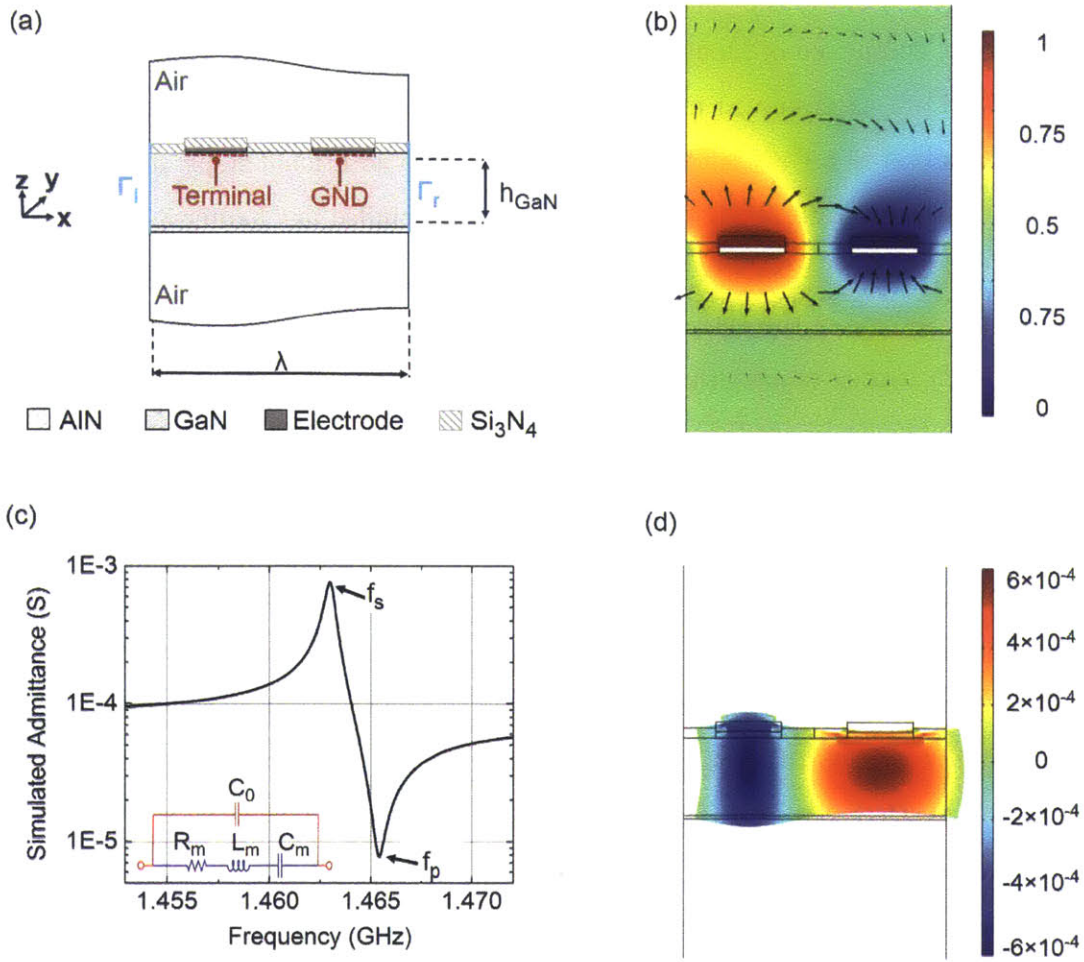


Figure 5-7: (a) Unit cell used in frequency response FEM analysis. (b) Electric potential (color map) and fields (arrow plot) induced by the drive signal. (c) Simulated admittance for $h_{\text{GaN}} = 0.3$. Inset shows equivalent circuit model. (d) Resonant mode shape.

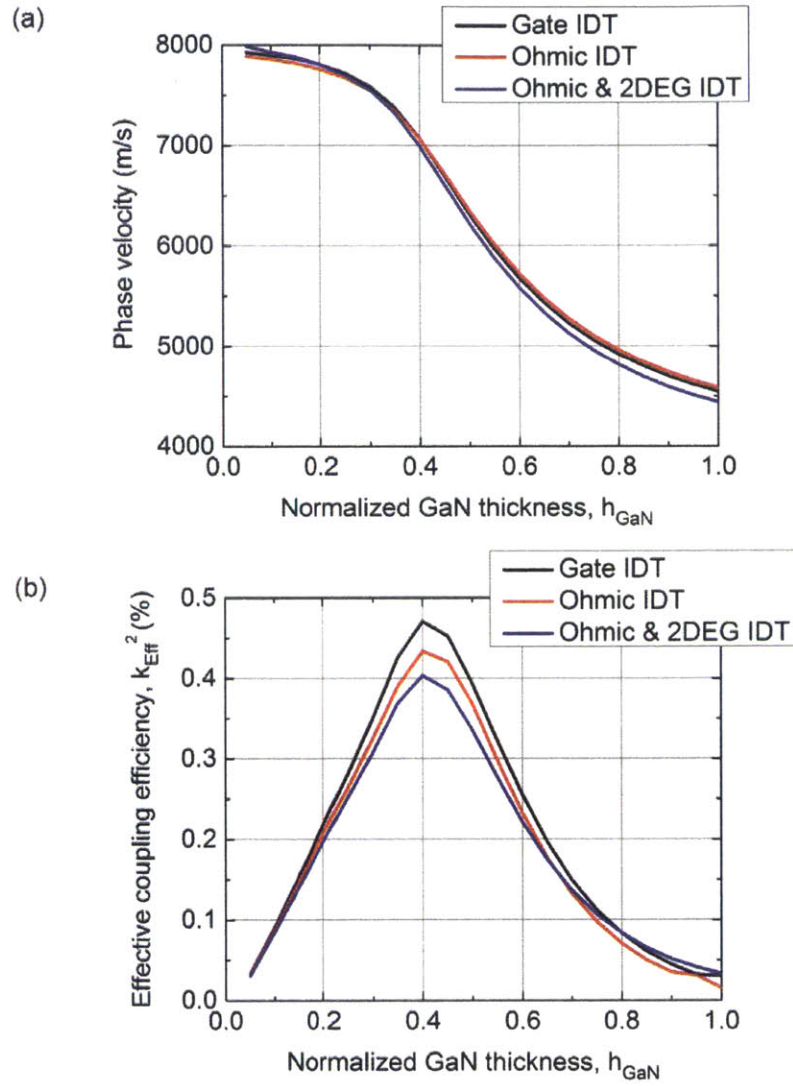


Figure 5-8: 2D frequency response simulation of (a) phase velocity and (b) effective coupling efficiency, k_{Eff}^2 .

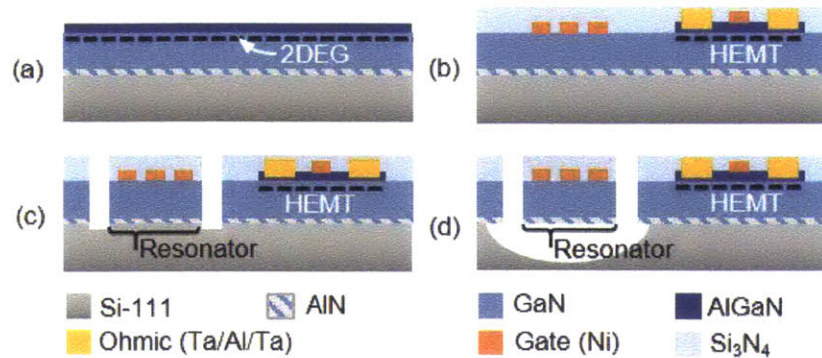


Figure 5-9: Fabrication process of GaN Lamb-Mode resonators integrated with HEMTs in a Au-free MMIC process. (a) Starting HEMT epitaxial heterostructure. (b) Standard HEMT front-end process. (c) First modification to HEMT process: deep GaN etch. (d) Second modification to HEMT process: isotropic silicon etch for MEMS release.

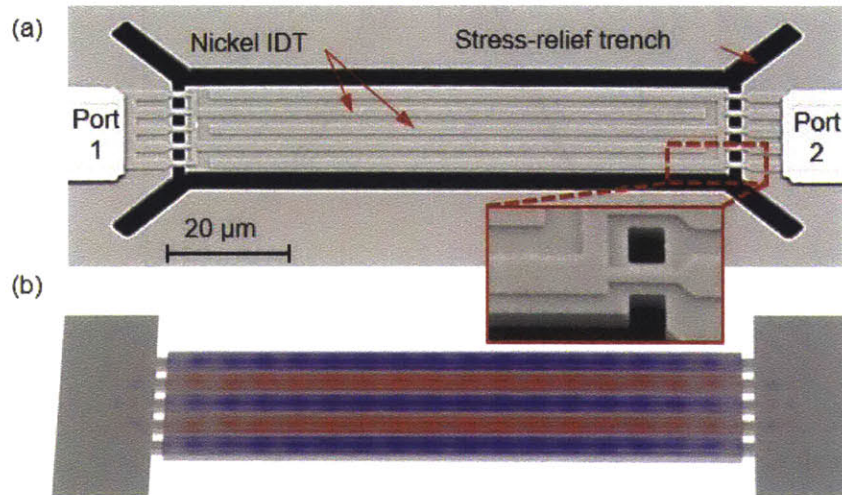


Figure 5-10: (a) SEM image of a 5th harmonic 1 GHz Lamb Mode resonator. The 3D FEM simulation in (b) illustrates the strain fields induced at resonance.

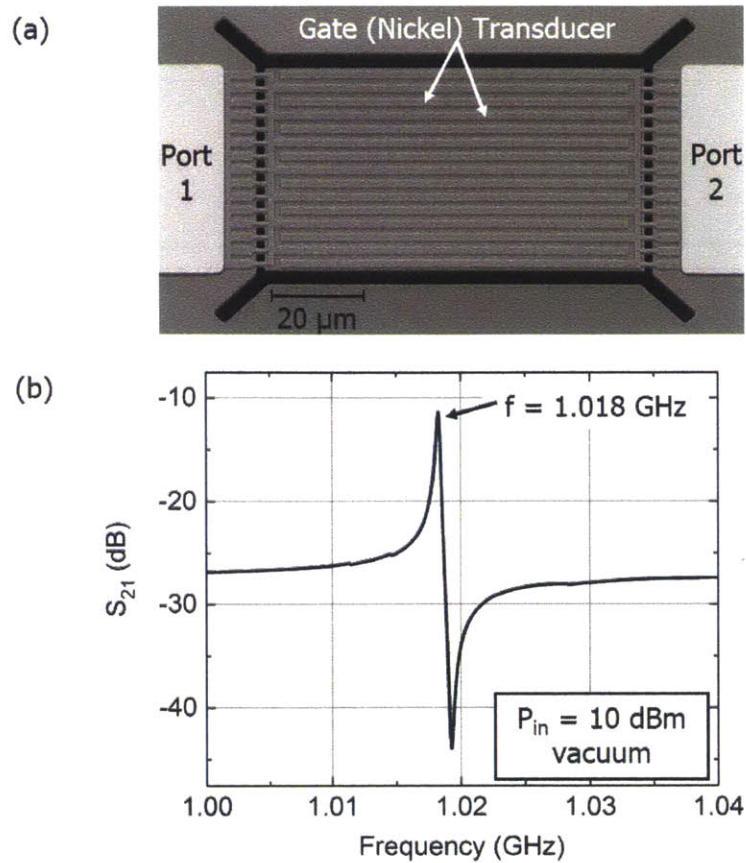


Figure 5-11: (a) SEM image of a 15th harmonic 1GHz Lamb-mode resonator. (b) Measured S Parameters under vacuum.

the HEMT process as IDT. A 3D Comsol FEA simulation shows the strain fields induced at resonance (Figure 5-10 (b)).

To prevent the formation of fractures at points of maximum stress, 45°-oriented trenches have been etched through the GaN film, in order to discontinue the released membrane around the resonator. Stress can be further relieved by using multiple suspension beams to the resonator. Using multiple anchor beams with a length equal to a quarter wavelength has also been shown to lead to higher Q , suppressed spurious modes, and increased power handling [13].

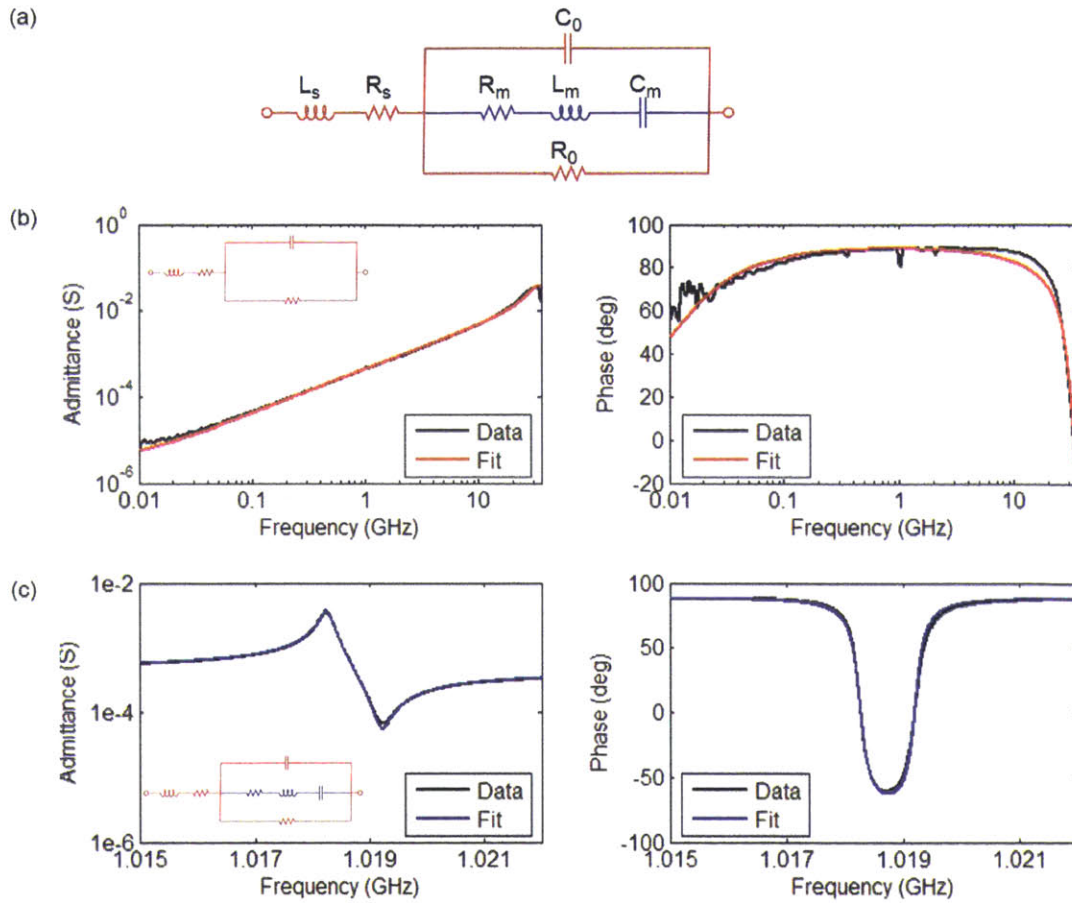


Figure 5-12: (a) Equivalent Circuit Model of the Lamb-mode resonators. (b) Frequency response of the device shown in Figure 5-11 is fitted over a wide frequency range, taking into account only the electrical parasitics. (c) Resonance peak is fitted to both mechanical branch and electrical parasitics.

5.4.1 Parameter Extraction

Resonators were measured in vacuum on a Cascade RF probe station, using a standard 2-port measurement on an Agilent Parametric Network Analyzer, and deembedded using an on-chip Open structure, as described in Section 3.3. The measured frequency response of a 15th harmonic resonator is shown in Figure 5-11.

To analyze this data we use the equivalent circuit model that was first introduced in Section 2.4 and is shown in Figure 5-12 (a). Here, the characteristics of the mechanical resonance are lumped into a series RLC branch (shown in blue) and the circuit elements shown in red are parasitics associated with the electrode fingers and

the losses through the GaN film.

Fitting a single dataset to a 7-parameter model can turn out to be quite challenging, especially as the competing contributions of the R_s and R_m resistances can lead to an erroneous extraction of the mechanical quality factor, Q_m . This can be simplified by making the observation that, for frequencies far from resonance, the response of the device will be mainly dominated by the parasitics. So we first perform a fitting of the data over a wide frequency range to a model that only includes the electrical parasitics associated with the transducer, but without including the mechanical RLC branch. Figure 5-12 (b) shows the fitted admittance, Y_{21} from 10 MHz to 35 GHz for the device introduced in Figure 5-11. From this model we pin down the values of R_s , L_s , C_0 and R_0 . We then move on to fitting the narrow frequency range data. We now include both the mechanical RLC branch and the electrical parasitics in the model, but we constrain these latter parameters to vary by only 5% from the values found in the wide sweep fit. The result can be seen in Figure 5-12 (c). Both the wide and narrow range fits are performed with a least-squares optimizer method in MATLAB, starting with initial parameter values based on either the material and geometrical properties of the resonators, or on estimates from the slope of the measured data.

From this analysis we can now extract the parameters of interest, i.e. the lumped equivalent circuit components, the mechanical quality factor, Q_m , and the electromechanical transduction efficiency, k_{eff}^2 . The relevant parameters from the fit performed above are listed in Table 5.1. One important figure of merit for a resonator is the product of frequency and quality factor, $f \cdot Q_m$, which was first introduced when discussing loss mechanisms in Section 2.5. Next, as derived in Section 2.3.5, the effective transduction efficiency of a resonator can be computed from the difference between the resonance frequency, f_s , and anti-resonance frequency, f_p :

$$k_{eff}^2 = 1 - \frac{f_s^2}{f_p^2}. \quad (5.5)$$

Table 5.1: Fitting parameters to the frequency response shown in Figure 5-12

Parameter	Value	Units
C_0	71.27	fF
R_0	0.25	$MOhm$
R_s	26.30	Ohm
L_s	0.30	nH
R_m	260.72	Ohm
C_m	0.13	fF
L_m	0.18	mH
Q_m	4528	-
Q_L	4113	-
f_s	1.018	GHz
f_p	1.019	GHz
k_{eff}^2	0.185	%
fQ	4.6×10^{12}	s^{-1}
FOM	7.64	-

Then the relevant figure of merit for a resonator is given by

$$FOM = \frac{k_{eff}^2 Q_L}{1 - k_{eff}^2}, \quad (5.6)$$

Here, Q_L is the electrically loaded quality factor of the resonator, calculated by:

$$Q_L = \frac{R_m Q_m}{R_m + R_s}. \quad (5.7)$$

Based on the data shown above, we can already see that these devices are very promising, both in terms of quality factor and transduction efficiency. First, we note that the $f \cdot Q$ value is higher than any results published previously in GaN. This is due to both the Au-free metalization used for the first time to fabricate MEMS integrated with HEMT, as well as to a good control of the sidewall profile of the GaN acoustic cavity. A more detailed study of the dependence of the mechanical quality

factor on frequency and transducer material is presented in Subsection 5.4.2. Second, the 1 GHz resonator shown above exhibits a k_{eff}^2 of 0.185%, for a normalized GaN thickness, $h_{GaN}/\lambda = 0.21$, which is not far from the expected theoretical value of k^2 expected from Figure 5-5. This means that the electromechanical properties of the GaN heterostructures used for MMICs are close to the performance expected from bulk crystal. However, for a better comparison between theory and experiment, we need to simulate the devices to include mass loading from both the metal electrodes and the passivation layer and study the frequency dependence of the coupling coefficient for the various types of IDTs introduced earlier. The results are shown in Subsection 5.4.3.

5.4.2 Quality Factor

Figure 5-13 shows a survey of extracted mechanical quality factors, Q_m , and their corresponding $f \cdot Q$ product, from devices operating at 4 different nominal frequency points, using the three types of IDTs introduced in Figure 5-2. Due to fabrication failure, the ohmic with patterned 2DEG devices shows no mechanical resonance at the highest frequency point, 1.9 GHz so there is no corresponding data point in Figure 5-13. There are three designs for each transducer, at each of the 4 frequency points considered in this study. The only difference between the three resonators designs for one type of transducer, for the same frequency is the length of the anchoring beams. One design uses an anchor length equal to a quarter wavelength, while use ± 50 nm variations of this length. As expected, different transducer types will mass load the resonator differently, leading to small variations in the resonant frequency. Additionally, it can be seen that the quality factor varies significantly among these devices, which means that the losses associated with leakage through the anchors are limiting the overall performance, not allowing us to draw a definite conclusion as to which is the better transducer material in terms of lower intrinsic material losses. Moreover, looking back at the frequency response obtained for the 1.9 GHz resonator, we note that we don't have a clean resonance, but rather multiple peaks of similar height, which means that the design of the cavity itself is not fully optimized, leading

to distortion and coupling of multiple modes (Figure 5-14). We notice similar response across all the 5th harmonic designs at 1.9 GHz. However, since the quality factors are within the same order of magnitude, and all devices exhibit quality factor comparable of larger than any GaN resonators to date, we can conclude that all of these transducer choices are appropriate for operation. Besides the goal of characterizing the intrinsic mechanical properties of these transducers, we also care about potential performance of these resonators in actual operation within a circuit or system, so it important to also consider the effect of the series resistance associated with the electrodes, R_s , which will lower the overall quality factor of the resonance. That is why we also compare the loaded quality factor, Q_L for these devices (Figure 5-15). The inset in this figure plots an average extracted series resistance of the three resonators designed for each frequency point, for the three types of transducers. Values for the resistivity and thickness of these transducers can be found in Chapter 3 and in Appendix A.

As discussed in Section 2.4, the overall insertion loss of a resonator scales with the area of transduction. To increase this area, we can realize resonant cavities with higher number of harmonics. Choosing the maximum number of harmonics for these devices was mainly motivated by structural issues related to fabrication. As discussed in Chapter 3, the resonators are released through the GaN etch trenches on the side, using an isotropic silicon etch. This implies that the release time is directly proportional to the dimension of the cavity. Moreover, since the silicon undercut is isotropic, we etch an equal distance under the GaN surrounding the resonator, which could lead to structural issues, such as cracking due to residual stress or coupling to low frequency membrane modes. Since the resonant cavities scale down in size as the frequency increases, we are able to implement 25 harmonic resonators for the highest design frequency, while for the lower frequency designs we limit ourselves to 15 harmonics.

Figure 5-16 shows a study of the dependence of Q_m on the number of harmonics for three different design frequencies. While the data in (a) doesn't show a conclusive trend when scaling with number of harmonics, in (b) and (c) we note a clear enhancement in Q_m as we increase the size of the acoustic cavity. The most significant trend

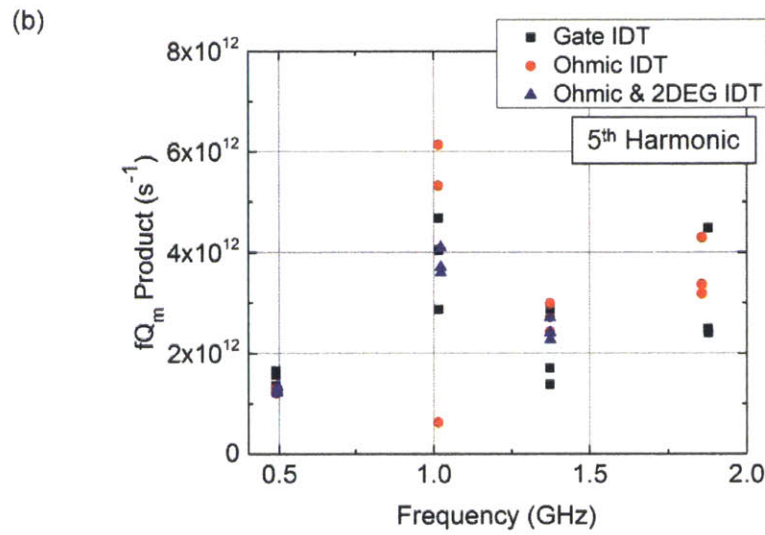
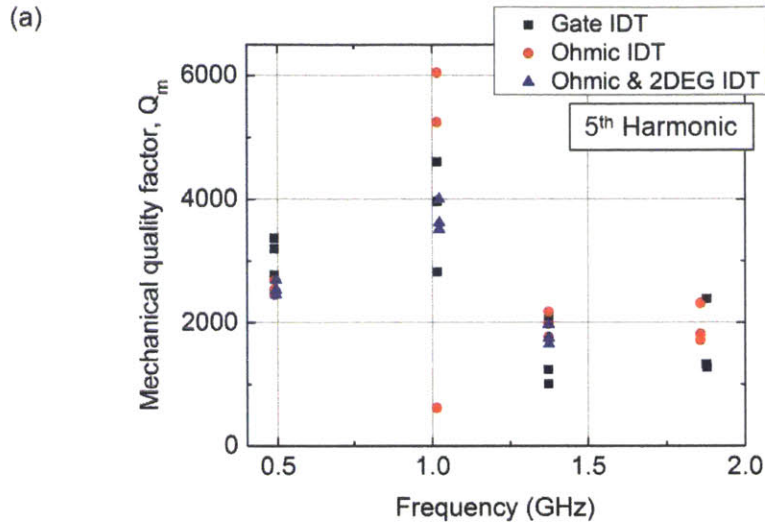


Figure 5-13: Measured mechanical quality factors (a) and $f \cdot Q$ (b) for devices using three different IDT configurations: gate IDT, ohmic IDT, and ohmic with patterned 2DEG IDT.

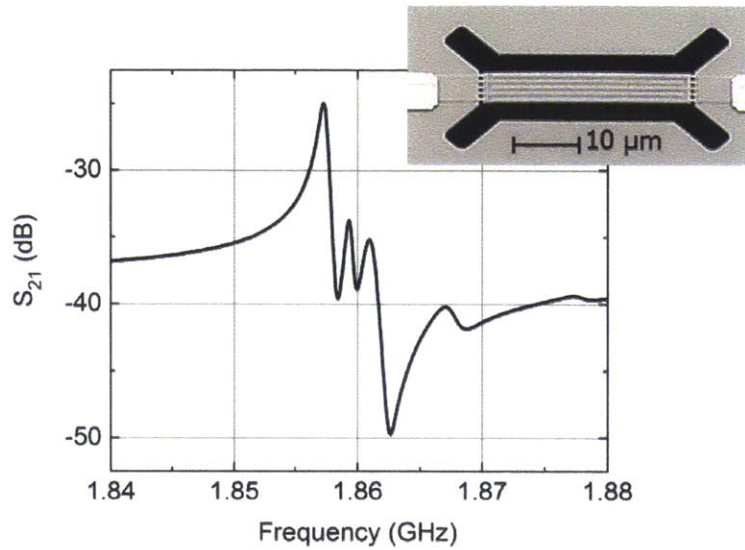


Figure 5-14: Measured frequency response of a 1.9 GHz gate IDT resonator.

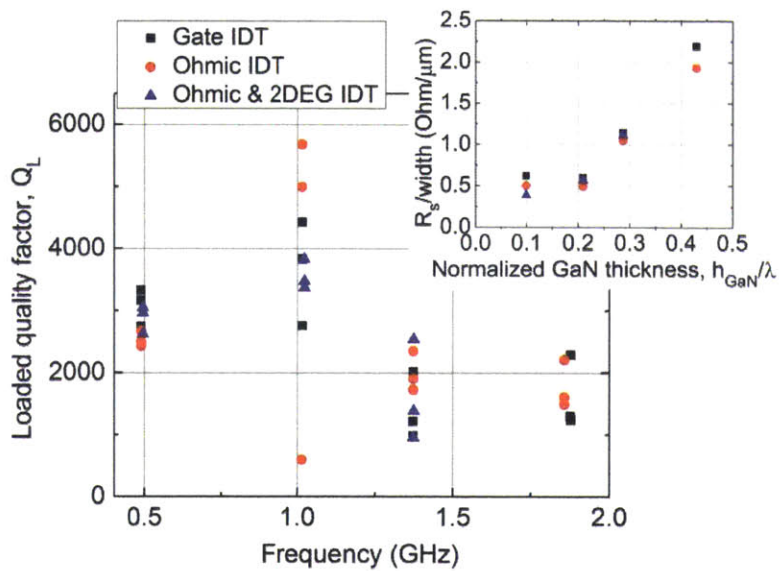


Figure 5-15: Electrically loaded quality factor, Q_L for devices using three different IDT configurations: gate IDT, ohmic IDT, and ohmic with patterned 2DEG IDT. Inset shows average extracted series resistance, scaled by the resonator width.

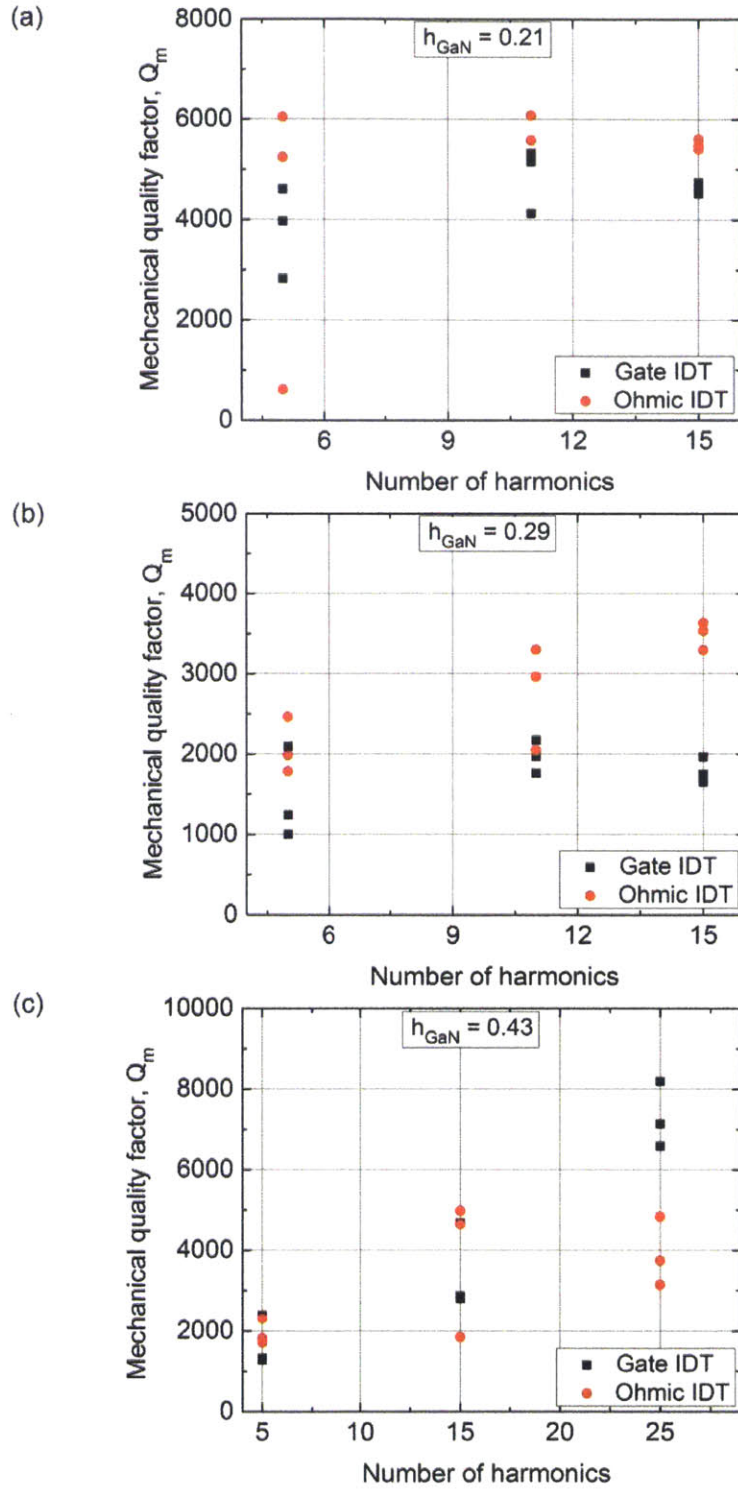


Figure 5-16: Mechanical quality factor of resonators with different number of harmonics.

is in the case of the highest frequency data, which is also the data set where we vary the number of harmonics by the largest increment.

This trend can be understood by going back to the physical interpretation of the quality factor, of stored energy divided by energy dissipated per cycle, which was first introduced in Chapter 2. As discussed in Section 2.5 and demonstrated above, one of the limiting loss mechanisms is the energy dissipation through radiation to the surrounding substrate through the anchoring beams. We have already discussed the dependence of this loss factor on the area:

$$\frac{1}{Q_{rad}} = A. \quad (5.8)$$

At the same time, the energy stored will be directly proportional to the volume of the acoustic cavity. As a result, we expect that an increase in volume will lead to more energy stored. However, in the case of the data shown above, the volume and the number of anchors are proportional to the number of harmonics, which should not lead to a higher Q. Another cause of the trend observed above could be related to losses due to scattering at the edge of the cavity. As the volume increases, the stored energy is higher, but the edges of the cavity stay constant, which leads to a lower ratio of scattering to stored energy and, as a result, more uniform, high-Q modes. This problem has a correspondent in the realm of electromagnetic cavities, and has been formulated by Edward Purcell [95].

This scaling of the acoustic cavity allowed us to achieve unprecedented quality factor values in GaN, reaching the limit of what is believed to be the phonon-phonon scattering limit in this material (see Section 2.5). For example, the device in Figure 5-17, with a mechanical Q_m of 8327 at 1.87 GHz, exhibits an $f \cdot Q$ of 1.56×10^{13} , making it the highest measured in GaN resonators to date. The fitted data and the extracted parameters are shown in Figure 5-18 and Table 5.2, respectively. To extract the parameters of interest for this device we used a similar approach as described in Subsection 5.4.1. However, since the measurement exhibits strong spurious mode responses close to the resonance of interest, we had to fit the data to a model including

multiple mechanical RLC branches added in parallel, as illustrated in Figure 5-18 (a). The spurious modes are a result of the fact that the cavity is finite in the other in-plane dimension, which leads to spurious modes. As the overall energy dissipation through scattering is reduced, the quality factors of the spurs are increased as well, leading to more prominent responses. However, as shown in the inset of Figure 5-17, the strains induced at the spurious resonance cancel out over the length of the electrodes, leading to a poor transduction efficiency, of only 0.02%. On the other hand, the mode of interest exhibits a high transduction efficiency, of 0.376% , leading to a FOM of 17.9, higher than any previously demonstrated GaN MEMS resonators. These results show high potential for using this technology for radio communications and timing applications.

5.4.3 Transduction Efficiency

Next, we want to study the electromechanical efficiency of the transducers available in this technology. We primarily want to answer two questions, First, we are interested in which type of transducer mass-loads the cavities the least, giving a higher transduction efficiency. Second, we want to compare the extracted k_{eff}^2 to the fundamental limit of transduction discussed in Section 5.2, to answer questions regarding the crystal quality of the MMIC stack, and its suitability for use as a MEMS technology, without additional processing or thinning down of the material.

We overlay the extracted k_{eff}^2 from the 5th harmonic devices that were already introduced in Figure 5-13, for the three types of transducers, as a function of frequency. First, we note that the measured phase velocity is lower than expected from simulation. This could be due to various factors, ranging from residual stresses that alter the elastic properties to other crystal non-idealities, especially in the region dominated by dislocations. In terms of transduction efficiency, we note that while for the lower frequency designs the experimental values are close to the simulated ones, the high-frequency design is lower than expected. However, looking back at the frequency response obtained for this design, shown above in Figure 5-14, we note that we don't have a clean mode, but rather multiple peaks of similar height, which leads

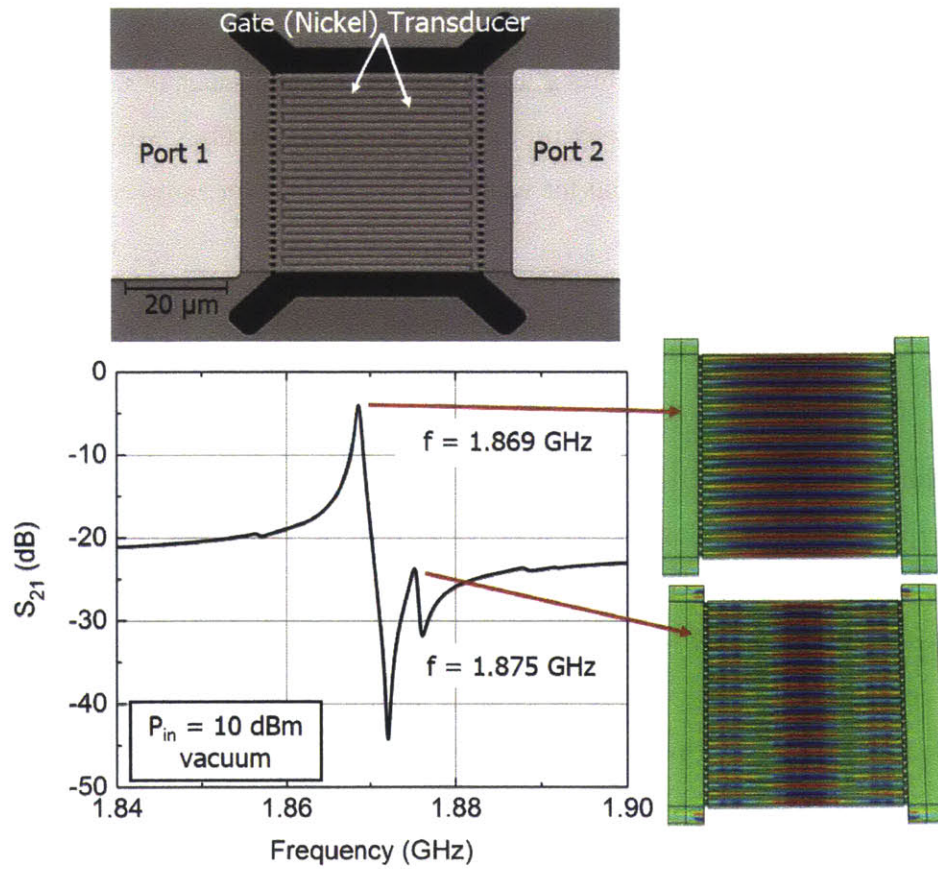


Figure 5-17: (a) SEM image of a 25th harmonic 1.9 GHz Lamb-mode resonator. (b) Measured S-Parameters under vacuum. Insets show 3D FEA simulation corresponding to resonance of interest and spurious mode.

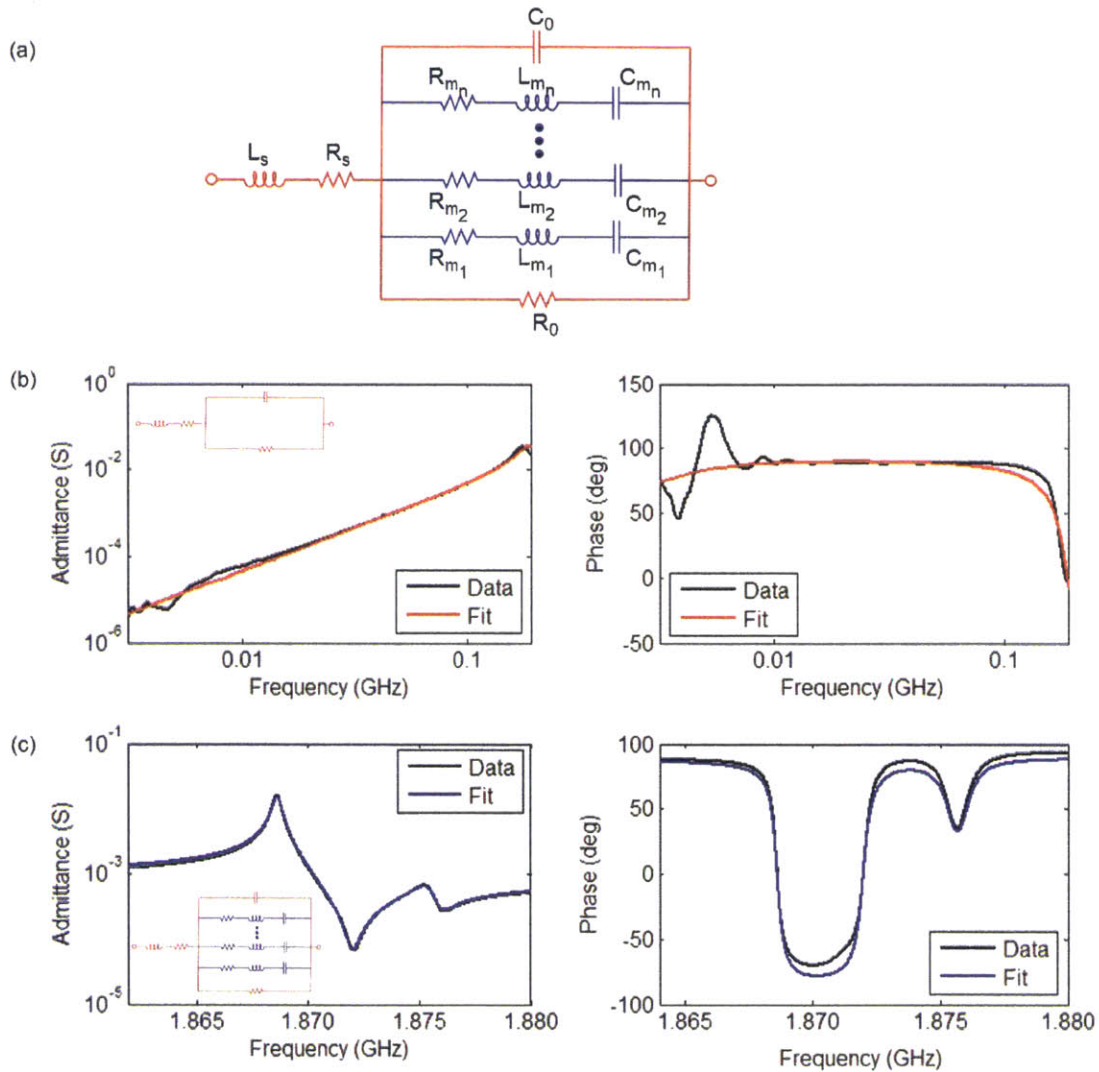


Figure 5-18: (a) Equivalent Circuit Model including spurious mode contribution. (b) Frequency response of the device shown in Figure 5-11 is fitted over a wide frequency range, taking into account only the electrical parasitics. In (c), the resonance peak is fitted to both mechanical branch and electrical parasitics.

Table 5.2: Fitting parameters to 1.9 GHz device shown in Figure 5-17.

Parameter	Value	Units
C_0	72.30	fF
R_0	0.78	$MOhm$
R_s	27.77	Ohm
L_s	0.29	nH
R_{m1}	37.52	Ohm
C_{m1}	0.27	fF
L_{m1}	0.03	mH
Q_{m1}	8327	–
Q_{L1}	4786	–
f_{s1}	1.869	GHz
f_{p1}	1.872	GHz
k_{eff1}^2	0.376	%
$f_{m1}Q_{m1}$	1.56×10^{13}	s^{-1}
FOM_1	17.92	–
R_{m2}	564.17	Ohm
C_{m2}	0.018	fF
L_{m2}	0.399	mH
Q_{m2}	2023	–
Q_{m2}	1928	–
f_{m2}	1.8754	GHz
f_{m2}	1.8756	GHz
k_{eff2}^2	0.025	%
$f_{m2}Q_{m2}$	3.8×10^{12}	s^{-1}
FOM_2	0.48	–

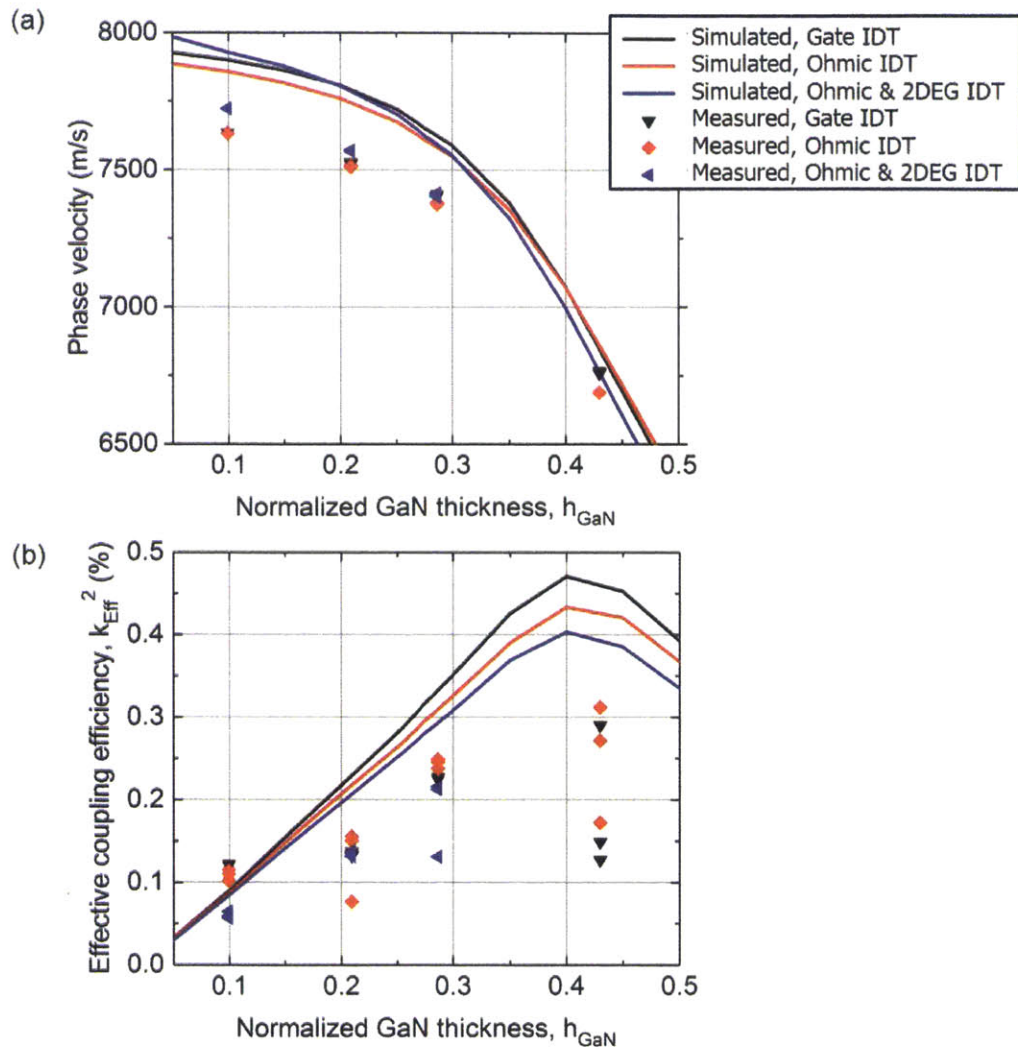


Figure 5-19: Comparison between simulated and measured (a) phase velocity and (b) transduction efficiency for 5th harmonic devices using different transducers.

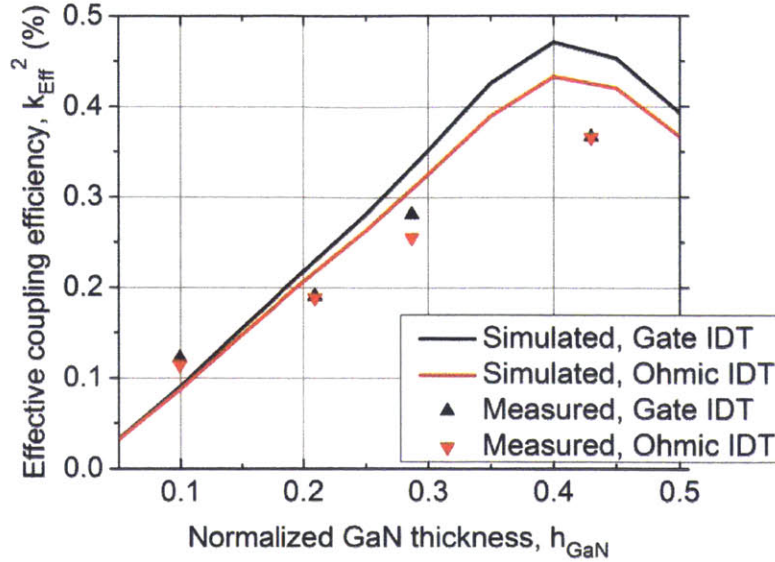


Figure 5-20: Comparison between simulated and measured transduction efficiency for higher harmonic devices using different transducers.

to distortion of the mode shape, and therefore low transduction efficiency.

As a result, to really get a measure of how good of a transduction we can get in this technology, we compare the best values of extracted k_{eff}^2 with the simulations. This allows us to pick the devices with the cleanest frequency responses and not be limited by the spurious mode coupling seen in the 5th harmonic devices. Since we don't have any data for the ohmic and patterned 2DEG IDT other than the results shown in Figure 5-19, we only show the gate and ohmic comparison here.

While the simulation is based on values of the piezoelectric coefficients that correspond to bulk single-crystal GaN, the thin-film material used to fabricate the resonators contains a high dislocation-density buffer region at the bottom of the stack [33, 63]. These defects are due to the lattice mismatch between the silicon substrate and GaN and can span up to a micron of the thickness of the film. Such crystal imperfections can affect the electromechanical properties of the material, leading to modified values of the piezoelectric coefficients and as a result, lower k_{eff}^2 . Additionally, the simulation does not include additional losses, such as leakage and dielectric

loss in the GaN film itself. We can conclude that, despite getting lower transduction than in the simulation, these resonators achieved high transduction efficiency and quality factors at the same time, leading to large values of the relevant FOM. This highlights the potential for using the HEMT stack for bulk acoustic resonators without additional processing of the material.

5.4.4 Ambient Operation and Power Handling

Pressure

Robust filters and oscillators in wireless systems require a complete characterization of the impact of ambient conditions, such as pressure and temperature on their performance, as well as excellent power handling capabilities. The pressure dependence of a 1GHz, gate IDT, resonator is shown in Figure 5-21. While a roll-off characteristic due to Couette damping can be seen in the range 1-1000 mbar, a total drop in Q_m of only 1.5% between high vacuum and atmospheric pressure is observed. This weak dependence on ambient pressure is another benefit of high frequency bulk modes, as discussed in Section 2.5. This shows high potential for monolithic integration of GaN resonators with HEMTs, without the need for expensive, ultra-high vacuum packaging.

Temperature

As GaN is increasingly used in high-power applications and for operation in harsh environments, it is important to characterize the effect of temperature on the performance of these resonators. To this end, we have tested these devices over a temperature range spanning $20^{\circ}C$ to $80^{\circ}C$, as shown in Figure 5-22. The relevant figure of merit here is the first order temperature coefficient of frequency (TCF), which was introduced in Section 3.3. From the data shown in Figure 5-22, the TCF is extracted to be $-24.2 \text{ ppm}/^{\circ}C$. This is comparable with other previously reported bulk mode GaN resonators [8], as well as AlN contour modes [91]. Several groups have demonstrated temperature-compensation in AlN Lamb-mode resonators that achieve a zero

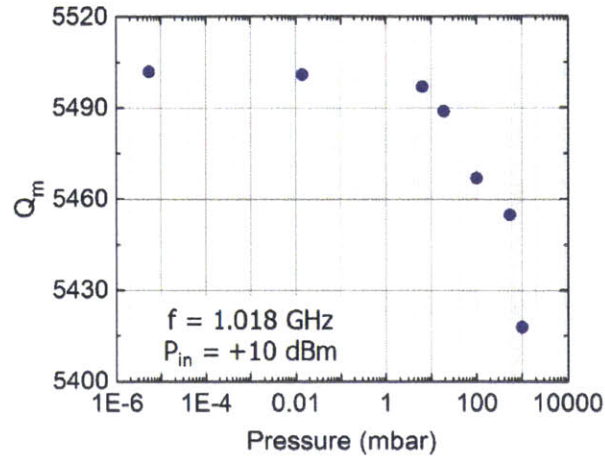


Figure 5-21: Ambient pressure dependence of mechanical quality factor for 1 GHz Lamb-mode resonator.

first order TCF, by incorporating a thin layer of silicon dioxide in the resonant cavity [96, 97]. Typical HEMT processes use a thin layer of dielectric for passivation. While here we use nitride as a passivation layer, which has a negative TCF, an oxide layer can be incorporated in the passivation stack to alleviate the change in resonant frequency due to temperature shifts. This has been shown in a thickness-mode GaN MEMS resonator, with an overall improvement $> 50\%$ [98] but yet remains to be demonstrated in GaN Lamb-mode resonators.

Power Handling

Another critical requirement for use in broadband radio communications is power handling. In Subsection 3.3.4 we introduced the concept of Third Order Intercept Point, or IP_3 used to quantify the power handling capabilities of a resonator for filtering applications. To investigate this figure of merit in our resonators, we use a similar approach to [79]. As bulk mode piezoelectric devices, the S_0 Lamb-mode resonators presented here exhibit excellent power handling capabilities. Figure 5-23 shows the power nonlinearity measurement of a 5^{th} harmonic, $19.4 \times 90 \mu m^2$ 1GHz resonator, with an extracted IIP3 of +23.3 dBm.

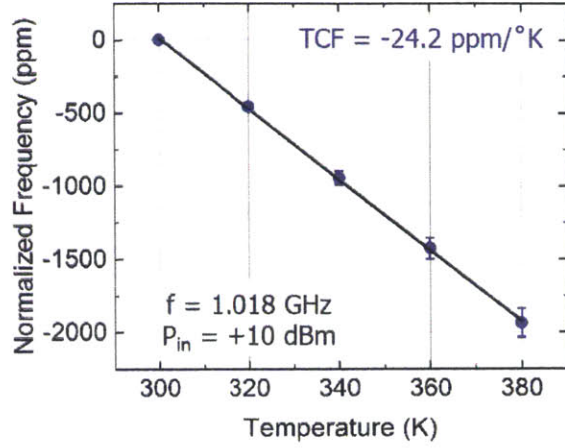


Figure 5-22: Temperature coefficient of frequency (TCF) for 1GHz Lamb-mode resonator.

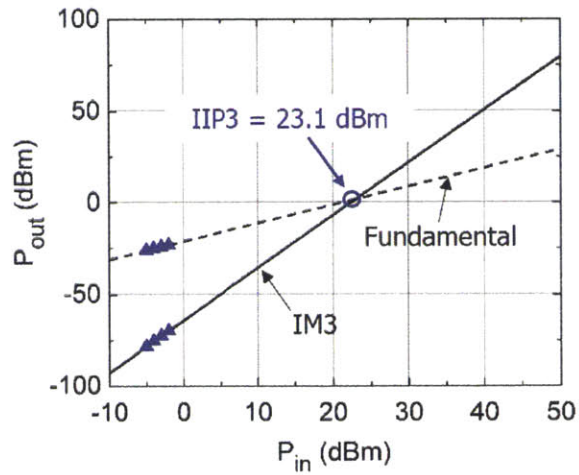


Figure 5-23: Power handling measurement of the 1 GHz Lamb-mode resonator, with an IIP3 of 23.1 dBm, with $19.4 \times 90 \mu\text{m}^2$ footprint.

5.5 Discussion and Benchmarking

In this chapter we have demonstrated multiple GaN Lamb-mode resonators with frequencies ranging from 400 MHz to 2 GHz. Figure 5-24 shows the best extracted mechanical $f \cdot Q$ product at each of the 4 distinct design frequencies, benchmarked against previously demonstrated GaN resonators. This plot also contains the theoretical limit on the $f \cdot Q$, due to phonon-phonon interactions, which was derived in Section 2.5. For simplicity, we only plot the limit corresponding to Lamb waves propagating in the [100] direction, with in-plane displacements, which corresponds to the waves of interest in this chapter, but in Section 2.5 we show that other propagation directions exhibit a very similar behavior. It can be seen that the devices in this work not only achieve the highest $f \cdot Q$ product to date, but also approach the theoretical phonon-phonon limit. One potential explanation for this high performance is the use of a Au-free process, which reduces significantly the loss associated with metal electrodes.

Additionally, this is the first characterization of Lamb-mode resonators using a top-metal transducer with no bottom electrode. We have shown in Section 5.4.3 that the measured transduction efficiency approaches the intrinsic k^2 , as well as the simulated effective electromechanical coupling, k_{eff}^2 . Figure 5-25 shows a comparison between best values of (a) k_{Eff}^2 and (b) $FOM = k_{Eff}^2 Q_m$ reported in this work and values reported previously in literature. While this work uses a top-electrode only IDT, the other work shown also use a bottom electrode, which explains the higher values of k_{Eff}^2 (see Section 5.2). However, the quality factors in this work are the highest in GaN to date, which leads to FOM values comparable to the bottom electrode case. Moreover, this study was realized in a standard GaN MMIC platform, with only two additional fabrication steps. As a result, this high performance, both in terms of transduction efficiency and quality factor means that the properties of the material stack used here approach the theoretical values expected for bulk, in spite of crystal non-idealities, especially at the bottom of the GaN film which exhibits a high dislocation density.

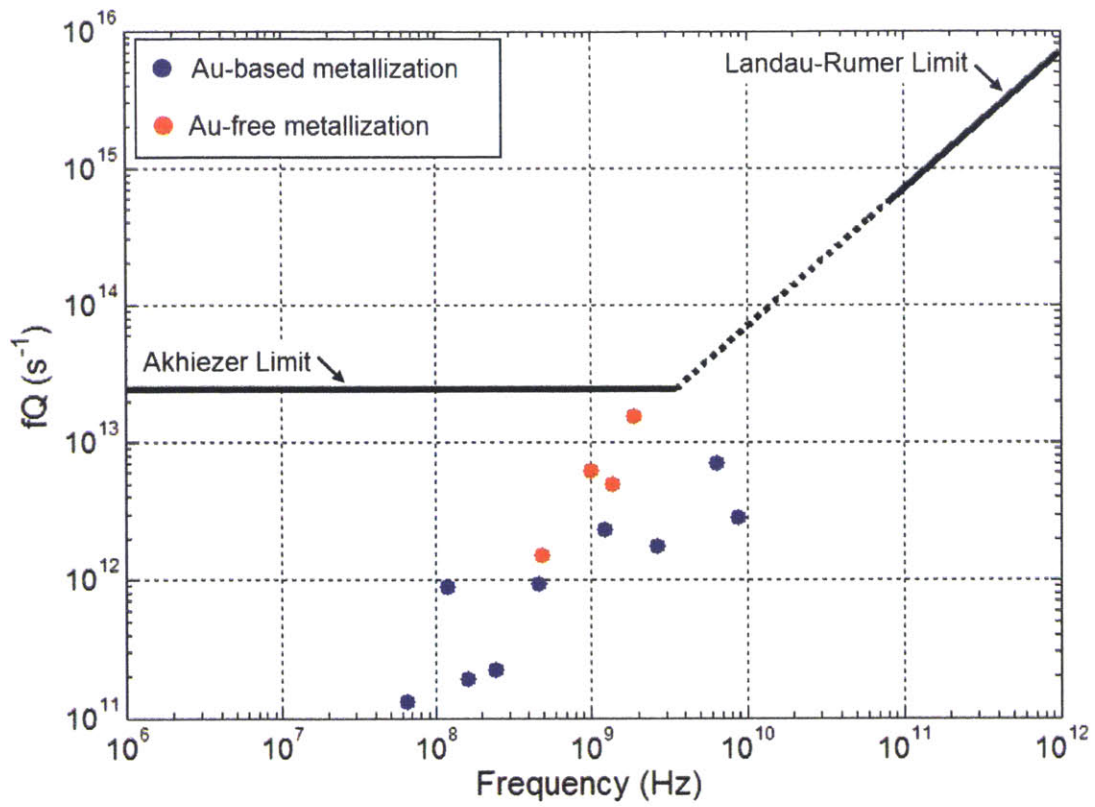


Figure 5-24: Measured $f \cdot Q_m$ from this work and other previously demonstrated GaN resonators from [7], [8], [9], [10], [11], and [12].

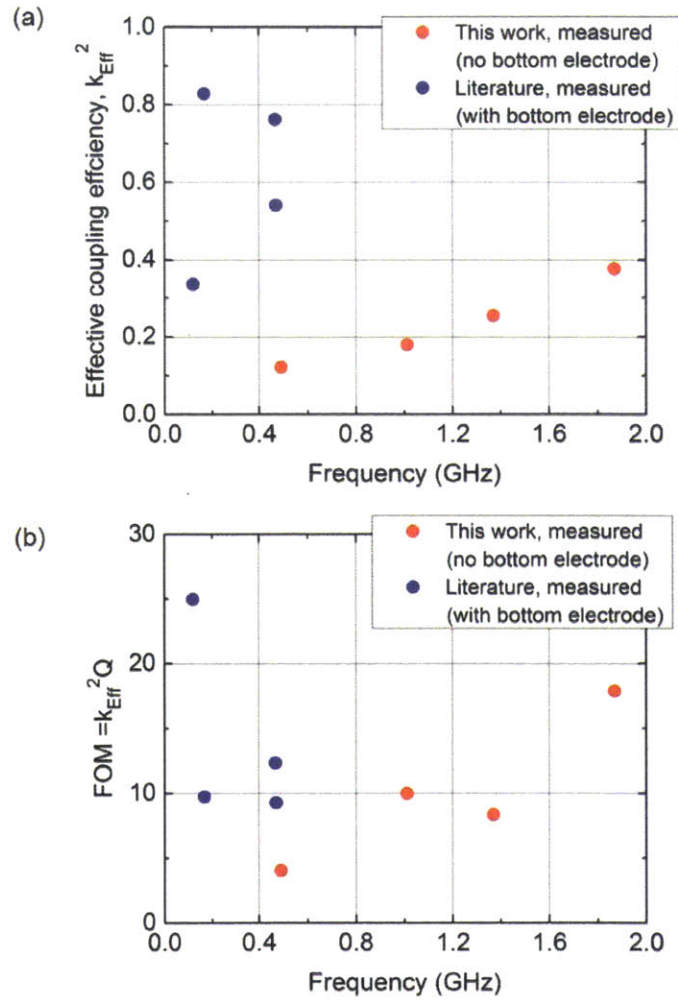


Figure 5-25: Measured k_{Eff}^2 (a) and $FOM = k_{Eff}^2 Q$ (b) from this work and other previously demonstrated GaN resonators from [8], [9].

Finally, the performance of the resonators as a function of pressure and temperature has also been investigated, as well as the power handling capabilities, showing high potential for seamless integration with high power, high frequency ICs for clocking and wireless communication.

Chapter 6

GaN Resonant Body Transistor

6.1 Motivation

As third and fourth generation (3G, 4G) wireless communications have emerged over the past few years the demand for higher bandwidth wireless data transfer has increased. Additionally, new application areas that require multi-GHz frequencies for faster data rates have developed, such as Local Area Networks (LAN) (60 GHz), personal navigation (94 GHz), and high-speed image processing. This has placed great importance on the performance of radio base stations and hardware, requiring low phase-noise frequency sources that exhibit immunity to nearby interferers and excellent power handling. With quality factors in the 1000's at GHz frequencies, small footprints, and the ability to achieve multiple frequencies on the same chip, MEMS resonators can provide building blocks for low phase-noise oscillators operating over a wide frequency range.

For successful implementation in low phase-noise oscillators, these resonators must satisfy two requirements: (1) High net signal-to-noise ratio and (2) small half-power bandwidth, i.e., high Q. For broadband operation, resonators must be scaled to multi-GHz frequencies. At such high frequencies, passive resonators suffer from capacitive feed-through between drive and sense transducers which overwhelms the mechanical peak and lowers the signal-to-noise ratio (SNR). Active Field Effect Transistor (FET) sensing has been shown to overcome this challenge through superior noise characteris-

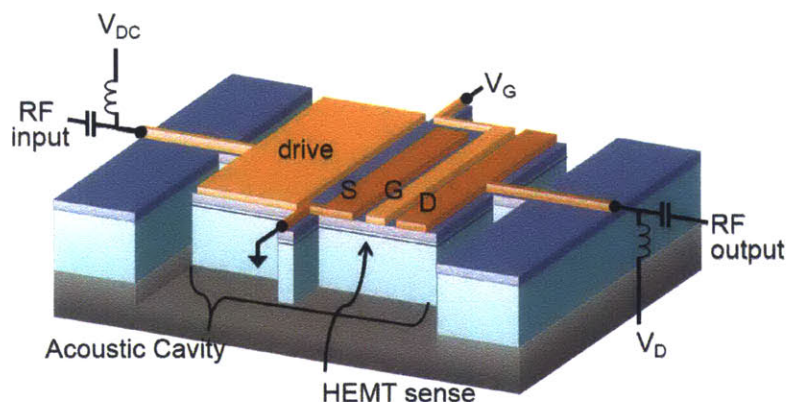


Figure 6-1: Schematic of GaN Resonant Body Transistor, where acoustic vibrations are driven piezoelectrically across the AlGaN layer, while sensing of mechanical waves is done with a HEMT.

tics, by providing internal electromechanical amplification of the resonant signal [99]. In Silicon, FET sensing has enabled resonators over 37 GHz [100].

Recently, there have been many efforts towards realizing RF MEMS resonators integrated with active electronics in standard foundry processes such as CMOS, III-V MMICs. Monolithic integration of MEMS resonators with ICs would lead to reduced matching constraints and parasitics, which ultimately translate into lower phase-noise and reduced jitter clocks, especially at high frequency. Additionally, this would enable a seamless use of the active FET components to directly sense the mechanical resonances. In Silicon, solid-state electrostatic MEMS resonators have been realized at the transistor level, without the need for additional processing [101]. In GaN MMIC technology we can take advantage of both the piezoelectric nature of the material and the high-gain HEMTs available. Multi-GHz HEMT-sensed devices have been demonstrated in flexural mode [102], contour mode [7] and thickness mode resonators [103].

6.2 Principle of operation

The concept of using a transistor to detect and amplify mechanical motion dates back to Nathanson's Resonant Gate Transistor in 1967 [104]. This device consisted of a

FET where the gate was a tuning fork, leading to oscillations in the effective gate potential, which generated an AC component of the drain current at the resonant frequency.

We extend this principle to a bulk, piezoelectric device, which we call the Resonant Body Transistor (RBT). Figure 6-1 shows a GaN RBT. This is a suspended cavity that contains a drive transducer in the left half, and an embedded HEMT for sensing the induced mechanical vibrations. The drive transducer is realized across the AlGa_N film, between the grounded 2DEG electrode and a top Schottky metal, as discussed in Section 4.4. At resonance, the amplified strains will lead to a change in the carrier density of the HEMT channel, leading to an AC drain current contribution at the resonant frequency. This charge is due to a change in the polarization, as a result of the direct piezoelectric effect. For Wurtzite crystal materials such as GaN, the induced polarization field can be written as:

$$\mathbf{P}_{PE} = (e_{51}\epsilon_{zx})\hat{x} + (e_{51}\epsilon_{yx})\hat{y} + (e_{31}\epsilon_x + e_{31}\epsilon_y + e_{33}\epsilon_z)\hat{z}. \quad (6.1)$$

Taking z along the Wurtzite c -axis, ϵ_x , ϵ_x , and ϵ_x are the strains along the x , y and z -axis respectively and ϵ_{yz} and ϵ_{zx} are shear strains. Here, e_{31} , e_{33} and e_{51} are the piezoelectric coefficients found in the Wurtzite crystal structure. There are two contributions to the bound charges associated with this polarization field. First, an interface charge σ is generated by a discontinuity in the polarization at the Al-GaN/GaN interface, induced by the difference in piezoelectric coefficients of the two materials:

$$\sigma = (\mathbf{P}_{PE,AlGaN} - \mathbf{P}_{PE,GaN}) \cdot \hat{z}. \quad (6.2)$$

Second, the polarization generates volume charge ρ throughout the heterostructure:

$$\rho = -\nabla \cdot \mathbf{P}_{PE}. \quad (6.3)$$

The RBT can be modeled according to the equivalent circuit shown in Figure 6-2. In the electrical domain, this device can be decomposed into two branches. The RLC

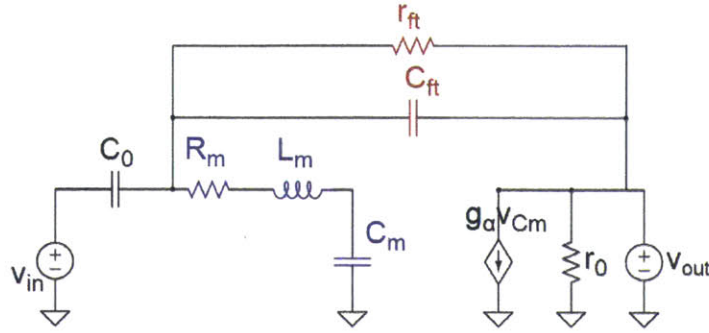


Figure 6-2: Equivalent circuit model of the RBT. Blue elements represent the equivalent mechanical RLC branch, according to a Butterworth Van Dyke model while the right side captures the electromechanical transconductance.

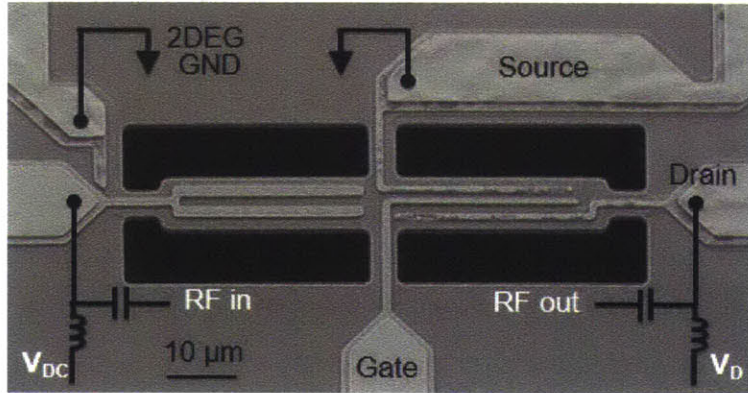


Figure 6-3: SEM of piezoelectric-drive, HEMT-sensed $8.7 \times 70 \mu m$ resonator. The HEMT has gate length of $1 \mu m$.

branch corresponds to the mechanical resonance induced in the two coupled bars, and is equivalent to a 1-port passive device. The second branch is a modified HEMT equivalent circuit, where the normal transistor transconductance is now replaced by an electromechanical transconductance, g_α . The parasitic feed-through between the input and output of the RBT includes a capacitance, C_{ft} and a substrate resistance, r_{ft} .

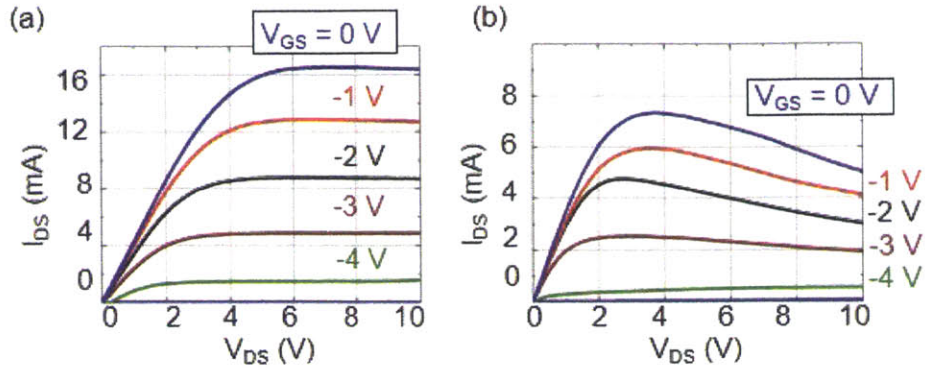


Figure 6-4: Measured IV curves of the HEMT embedded in resonator (a) before and (b) after release step.

6.3 Experimental Results

We have fabricated HEMT-sensed resonators in a standard HEMT process, with only two additional steps for the patterning and release of the acoustic cavities, as discussed in Section 3.2.1. Figure 6-3 shows such a device. The top Schottky metal in the drive transducer has now been patterned to excite higher frequency contour modes, as opposed to the passive case (see Section 4.4).

6.3.1 DC Behavior of RBT

Figure 6-4 shows the measured DC behavior of the HEMT embedded in the resonant structure (a) before and (b) after the release step. Prior to the release step, the HEMT has a threshold voltage V_{th} of 6.2 V, which corresponds to a 2DEG density of $5 \times 10^{12} \text{ cm}^{-2}$. After release, the HEMT exhibits V_{th} of 5.75 V, and the extracted charge density drops to $4.6 \times 10^{12} \text{ cm}^{-2}$. One possible reason for this current reduction is the generation of surface defect states during the final fabrication steps, with a direct impact on the electron density in the 2DEG. These surface effects can be alleviated by introducing a passivation layer early in the process [73]. Another possible cause of this degradation is the stress relaxation due to the release of the structure [105]. Using an optical profilometer to measure the radius of curvature of the released resonators, an initial compressive stress of 1.4 GPa was found at the GaN/Si interface.

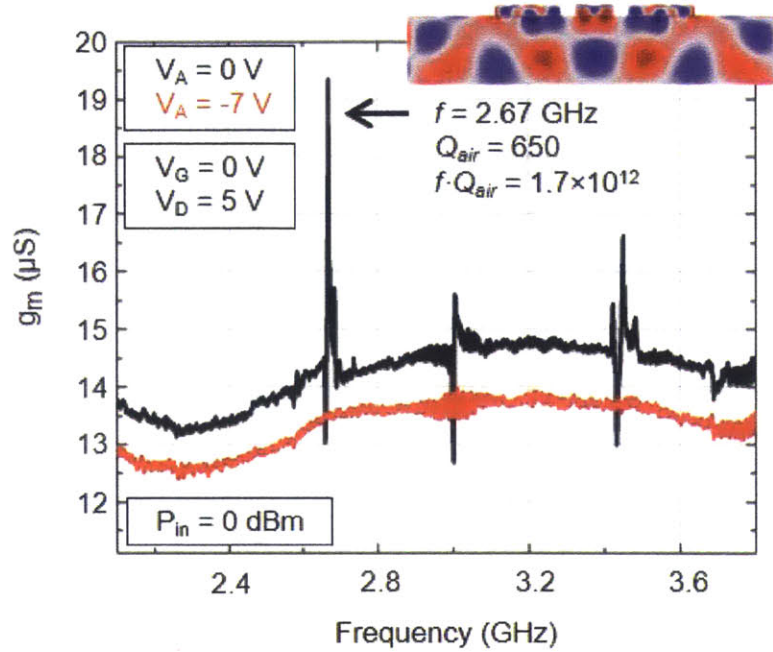


Figure 6-5: Measured frequency response of PE drive-HEMT sense AlGaIn/GaN resonator, in air. The transconductance, $g_m = Y_{21} - Y_{12}$, is suppressed when the 2DEG under the drive electrode is depleted. The inset shows a FEA simulation of the cross-section of the sense HEMT, where the color map represents the strain fields induced at resonance.

In addition, a $2\times$ reduction in the drain current in the saturation regime is observed, caused by the high channel temperature. AlGaIn/GaN HEMTs on Silicon substrates have been shown to exhibit channel temperatures as high as 350°C [106]. After the release step, the HEMT is thermally isolated, increasing the operational temperature. This reduces the mobility of the 2DEG, which translates into an increase in the channel resistance and a negative differential resistance at the output of the HEMT, as observed in Figure 6-4 (b). Both stress and temperature effects can be alleviated through an increased number of suspension beams of the resonator, which has also been shown to suppress spurious modes and enhance Q [13].

6.3.2 RF Behavior of RBT

Using HEMT sensing, resonators up to 3.5 GHz were realized and detected with simple 2-port measurements as shown in Figure 6-5. The electromechanical transconductance is defined as:

$$g_{em} = Y_{21} - Y_{12}, \quad (6.4)$$

where Y are the admittance parameters measured for the 2 ports. The active device is measured in air with 50Ω termination. While a Line-Reflect-Match algorithm was used to de-embed the testing setup up to the RF probes, no on-chip de-embedding structures were used for this particular measurement. The resonance at 2.67 GHz has Q of 650 in air with $f \cdot Q$ of 1.7×10^{12} , one of the highest reported in GaN resonators to date. A COMSOL simulation of the stress distribution of this resonance is shown as an inset in Figure 6-5, with maximum stress under the gate of the transistor. This translates into an efficient modulation of the charge density in the channel of the HEMT. It is also worth mentioning that this is the highest frequency contour mode measured in GaN to date. As in the case of the passive device introduced in Section 4.4, applying a negative bias $V_{DC} = -7 V$ to the drive transducer depletes the 2DEG and suppresses the resonance signal, while reducing the drive capacitance C_0 by $13\times$.

6.4 Mechanically Coupled RBTs

6.4.1 Principle of Operation

The RBT demonstrated above RBTs implements a single resonant cavity containing both drive transducer and sense transistor, resulting in direct electrical coupling between the RF input and transistor terminals (Figure 6-6 (a)), which increases the broad-band floor of the device. This parasitic feed-through is represented in the small signal model in Figure 6-2 by the components C_{ft} and r_{ft} .

Another approach, is to embed the drive transducer and sense transistor in two electrically isolated, mechanically coupled resonators (Figure 6-6 (b)). While mechanical coupling of two or more passive MEMS resonators has been previously used

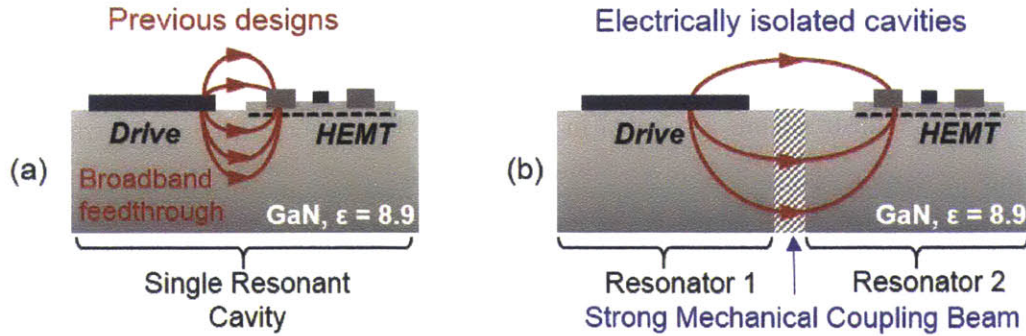


Figure 6-6: Schematic of GaN Resonant Body Transistor. (a) Placement of drive transducer and sense transistor in the same acoustic cavity leads to broadband feedthrough. (b) Electrical isolation between drive transducer and sense transistor is done by mechanically coupling two resonators.

to achieve tunable, low insertion-loss filters [107], this is the first implementation that takes advantage of active transistor sensing [108].

6.4.2 Experimental Results

Fig. 2 shows the SEM of a mechanically coupled GaN RBT, fabricated in an Au-free HEMT process, as discussed in Section 3.2.2. Acoustic waves are launched piezoelectrically with an interdigitated transducer (IDT) in resonator 1. This first resonator is mechanically coupled to resonator 2, via an array of beams of length equal to half wavelength of the beam vibration at the desired resonant frequency. This guarantees that the two bars will resonate in phase [107]. A HEMT is embedded in resonator 2 for sensing. At resonance, standing waves are induced in both drive and sense resonators, leading to strain fields that modulate the carrier concentration of the 2DEG in the channel of the HEMT just as in the case of the single cavity approach.

While mechanically coupled RBTs can be implemented in various bulk or flexural modes, in this work we focus on the zero order symmetric Lamb mode, S_0 . We have previously optimized and investigated the transduction capability of these modes in standard MMIC technology (see Chapter 5), achieving Q s as high as 8300 at 1.9 GHz and effective electromechanical coupling (k_{eff}^2) of 0.39% for resonators between 1-2 GHz [90]. Figure 6-8 (a) shows a 3D simulation of 2 mechanically coupled Lamb

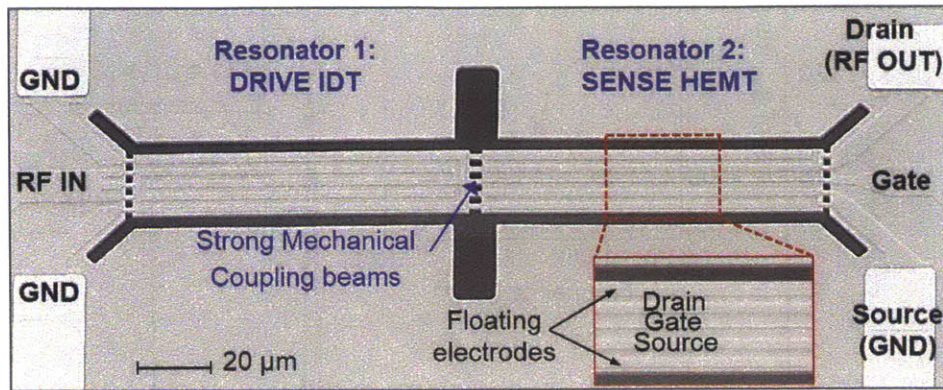


Figure 6-7: SEM of mechanically coupled drive and sense resonators. Source and drain electrodes, and two additional floating electrodes are patterned to match the drive transducer. A 5-tether approach is implemented to allow for a larger heat sink due to the HEMT current, as well as for improved power handling and spurious mode reduction [13]. Trenches are patterned through GaN to provide stress relief and better isolation between drive/sense.

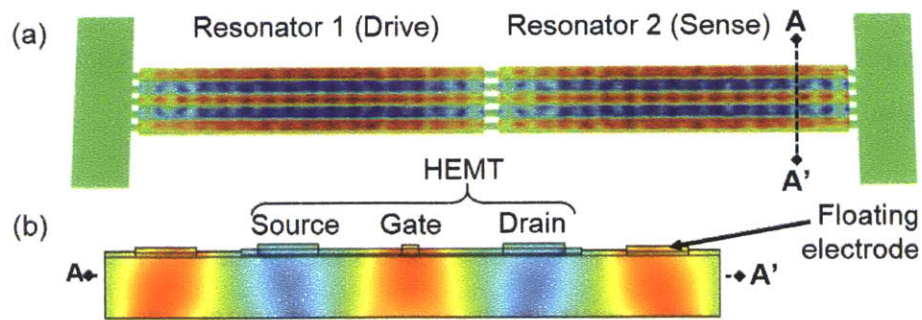


Figure 6-8: (a) 3D mode shape of strongly coupled resonators. (b) Gate of sense HEMT is placed at maximum strain. Source, drain and floating electrodes are patterned to match drive IDT.

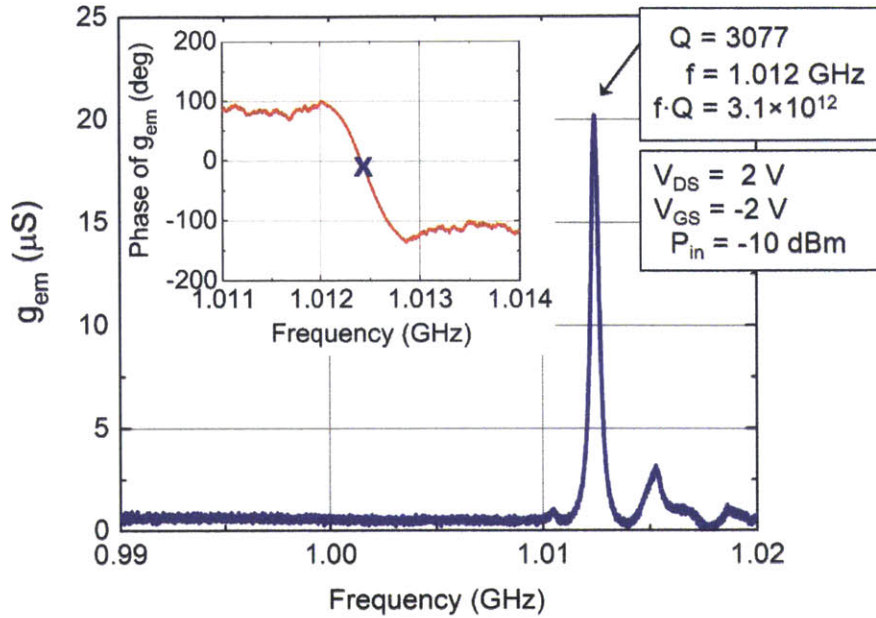


Figure 6-9: Measured g_{em} of mechanically coupled RBT in Figure 6-7 shows $> 10\times$ reduction in broadband floor compared to previously reported results. Inset shows 180° phase shift corresponding to mechanical resonance.

mode resonators. The 2D cross-section of the strain under the HEMT, with maximum modulation under the gate for optimal drain current modulation, is presented in Figure 6-8 (b). The gate of the embedded HEMT is designed at 500 nm. Two floating electrodes are patterned in gate metal on either side of the HEMT in order to maintain mass loading symmetric to the drive IDT.

Low-velocity coupling

Figure 6-9 plots the measured electromechanical transconductance, g_{em} , of the device shown in Figure 6-7. The 1.012 GHz resonance exhibits Q of 3077, with $f \cdot Q$ product of 3.1×10^{12} . The off-resonance floor in this device is below $0.8\mu S$, which is $> 10\times$ lower than previously reported GaN RBTs [7], [103] in this frequency range. This corresponds to an SNR of 20.4. As discussed before, this broadband suppression is critical for the realization of low phase-noise oscillators, especially when scaling to

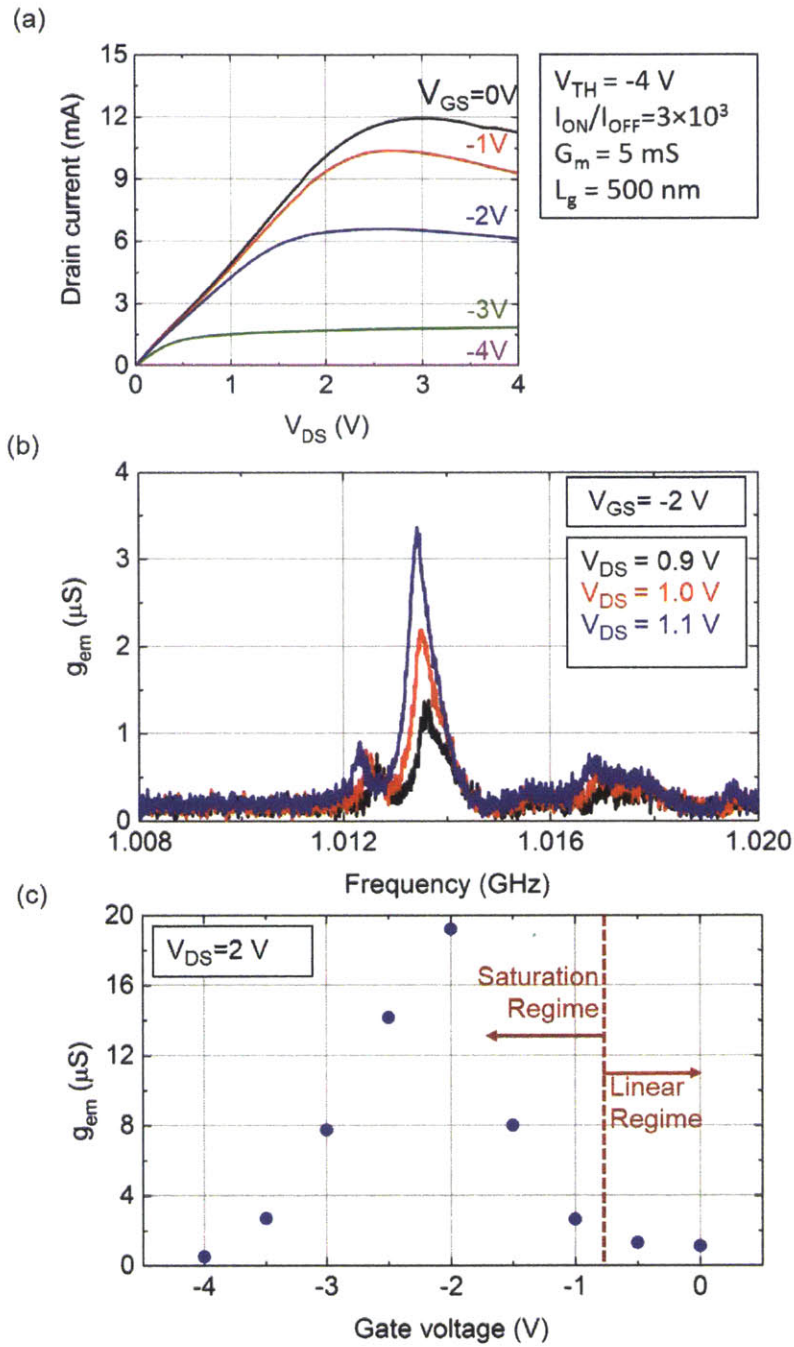


Figure 6-10: (a) DC behavior of embedded HEMT. (b) Dependence of g_{em} on drain voltage in the linear regime shows linear increase in acoustic transconductance, while floor remains mainly unchanged. (c) Dependence of g_{em} on gate voltage in the saturation regime shows optimal performance when the gate is set to -2 V.

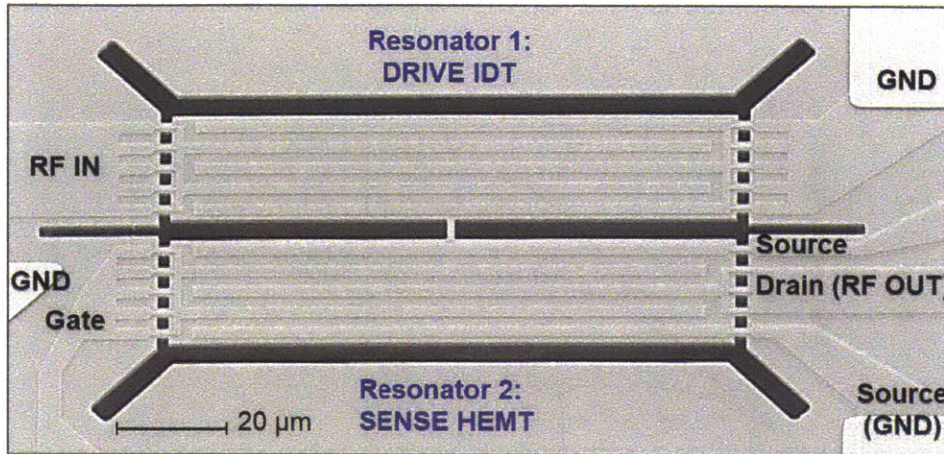


Figure 6-11: SEM of mechanically coupled RBT, with coupling beam at maximum velocity point. The embedded HEMT has two fingers, with gate length of $3.7 \mu\text{m}$. Similar to the low-velocity case, trenches etched in GaN are used for stress relief and better isolation between drive/sense. An extra ground electrode is placed between the RF input and gate for better shielding.

GHz frequencies. The effect of reduced broadband floor can be seen in the inset of 6-9, which shows a clear 180° shift at the mechanical resonance.

The DC behavior of the embedded HEMT used for electromechanical sensing is shown in Figure 6-10 (a). The transistor drives a maximum current of 12 mA in saturation, and has a threshold voltage of -4 V. The current degradation at drain bias (V_{DS}) > 2 V can be attributed to self-heating, as the HEMT is released from the substrate so the heat can only dissipate through the 5 anchoring tethers. In Figure 6-10 (b), the dependence of g_{em} on drain bias in the linear regime is shown, exhibiting a linear increase in electromechanical transconductance at resonance. It is important to note that the broadband floor remains constant independent of drain voltage. This behavior yields an increase in SNR from 7.6 for $V_{DS} = 0.9\text{V}$ to 13.6 for $V_{DS} = 1.1\text{V}$. In Figure 6-10 (c), the effect of gate bias (V_{GS}) on the electromechanical transconductance is shown for a fixed drain voltage. Optimal performance is obtained when V_{GS} is set to -2 V.

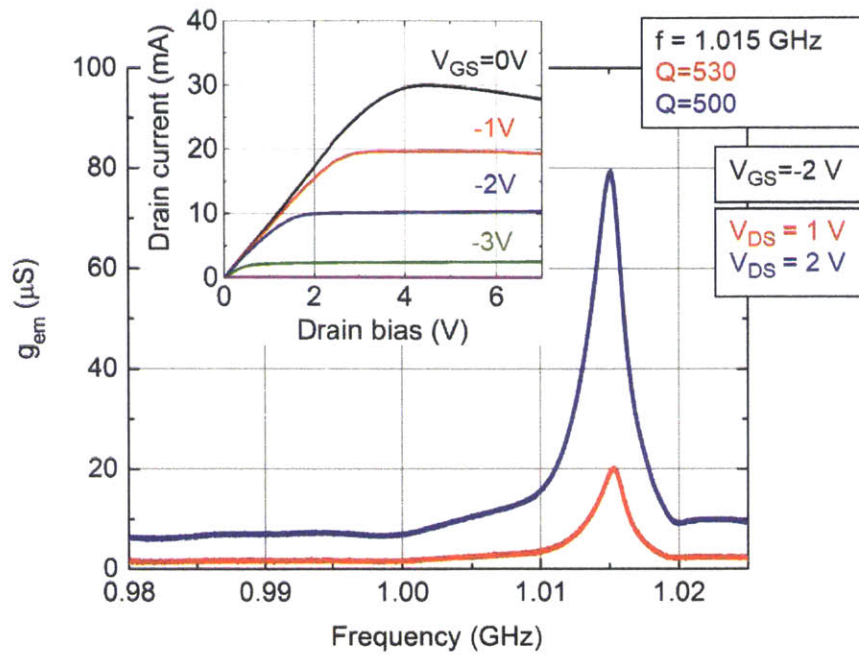


Figure 6-12: Measured g_{em} for double-gate RBT shows an acoustic transconductance of $72 \mu S$, $> 2\times$ higher than previously reported GaN RBTs, with SNR > 50 . Inset shows DC IV characteristics of HEMT used for electromechanical transconductance.

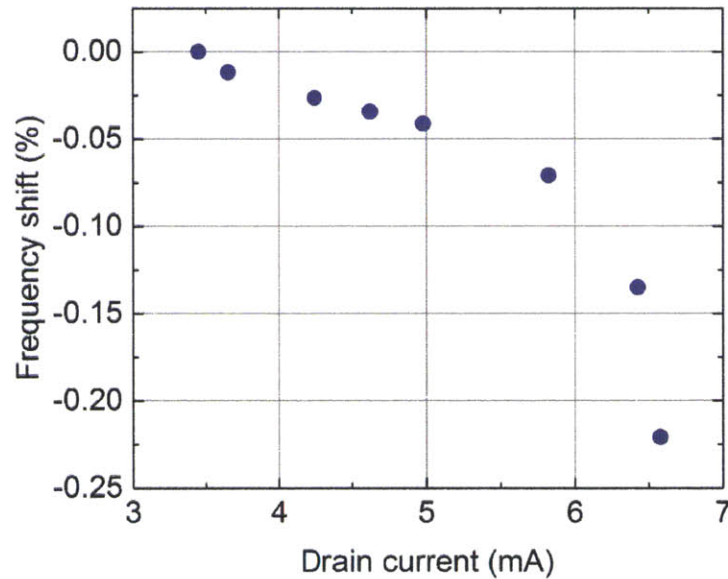


Figure 6-13: Measured resonant frequency shift with drain current for low-velocity coupling device shows 0.2 % tuning capability.

High-velocity coupling

Figure 6-11 presents an SEM of an RBT where the mechanical coupling between the drive and sense resonators is realized at the point of maximum velocity. This design opens up additional tethers on the sense resonator to enable routing for multi-finger HEMTs, necessary to achieve higher electromechanical transconductance, g_{em} . To optimize performance, both gates of the multi-finger HEMT are placed at points of maximum strain. The 2-gate transistor reaches a saturation current of 30 mA. The measured g_{em} for two drain bias points is shown in Figure 6-12. While there is a small change in the broadband floor with biasing conditions, the floor at $V_{DS} = 2V$ is still smaller than previously demonstrated devices, while the g_{em} of $72 \mu S$ is the largest achieved in GaN RBTs to date. Possible reasons why this device provides less isolation than the low-velocity coupling case include spatial proximity of electrode routing outside the resonant structure, larger overlap area between the drive and sense cavity, and a higher overall transistor transconductance. However, the SNR for this device is higher than in the low-coupling case.

Frequency tuning

One consequence of HEMT sensing in the GaN RBT is self-heating of the suspended structure, which is thermally grounded only through small suspension beams. This self-heating leads to a change in the elastic constants of the resonant cavity, resulting in a frequency shift. In Chapter 5 we found the temperature coefficient of frequency to be $-24.2 \text{ ppm}/^\circ C$. Here, we investigate the frequency shift as a function of applied drain current, as shown in Figure 6-13, with over 0.2% frequency shift at 6.6 mA bias current. Besides heating, changing the DC bias point will lead to different static electric fields through the structure. This could lead to nonlinearities associated with the dependence of the elastic constants on strain, which could also explain the frequency shifts seen here. The device provides a built-in microheater enabling tuning capabilities for frequency drift compensation due to temperature, packaging stresses, or other time-dependent parameters. Integrated microheaters have been previously

used for tuning MEMS resonators, both in the case of capacitive [109] and piezoelectric transduction [110].

6.5 Discussion and Benchmarking

Table 6.1: Summary of mechanical performance of state-of-the art GaN RBTs shows $100\times$ improvement in SNR in this work

	f	Q	G_M	I_{max}	g_{em}	floor	SNR
	GHz	–	mS	mA	μS	μS	–
Single cavity	2.67	650	2.5	7.5	6	14	0.4
Single cavity [103]	4.23	250	3	8	25	50	0.5
Coupled, low-velocity 1	1.013	3068	4.3	11	9	0.8	11.3
Coupled, low-velocity 2	1.013	3077	5	12	19	0.9	20.4
Coupled, high-velocity 2	1.015	530	10	30	72	1.4	51.4

We have demonstrated HEMT-sensed devices up to 3.67 GHz, the highest contour mode resonance detected in GaN to date. We also developed a method for suppressing off-resonance feed-through in GaN RBTs, enabling $> 100\times$ improvement in SNR. These devices were fabricated in a Au-free process which has yielded the highest fQ products in GaN RBTs to date. At the same time, the RBTs presented here achieved $> 2\times$ higher acoustic transconductance than previous GaN devices. Table 6.1 summarizes the results for 4 devices described in this work, including the single-cavity device, 2 low-velocity coupled RBTs (one with $L_{gate} = 3.7 \mu m$ and the other shown in Figure 6-7) and one high velocity coupled RBT (Figure 6-11). These resonators are compared with HEMT-sensed GaN resonators published in literature, and demonstrate order-of-magnitude improvement in SNR. Realized in standard MMIC technology, these devices can leverage strong piezoelectric coupling, large breakdown fields, and high speed HEMTs for monolithically integrated, low phase-noise clocks.

Chapter 7

Conclusion

7.1 Summary of Results

We were able to harness the electromechanical properties of the GaN heterostructure by developing MMIC compatible resonator designs and fabrication methods. While most HEMT processes use Au-based electrodes for low-resistance gates and to form Ohmic contacts, Au has extremely high acoustic losses, which can lead to poor performance of the MEMS. We developed an Au-free HEMT process at MIT and fabricated for the first time GaN MEMS resonators in an Au-free HEMT process, with Q s of more than 8000 at 2 GHz, showing the highest frequency-quality factor product in GaN to date. With this performance, we then focused on demonstrating several capabilities unique to GaN MMIC technology.

First, we showed the first DC switchable piezoelectric resonator. As the 2DEG is conductive enough to serve as an electrode, we formed a piezoelectric transducer across the AlGa_N film between the 2DEG and a top Schottky metal electrode. Then the resonator was switched between the ON and OFF states with a simple DC bias to the top metal, which depletes the 2DEG electrode and therefore suppresses the drive force. This depletion also results in a 13 \times reduction in the shunt capacitance of the drive transducer, alleviating the issue of capacitive loading of the antenna in large filter banks.

Next, using the 2DEG as electrodes for transduction was taken one step further

in order to realize a completely metal free GaN resonator. This was done with a simple shallow AlGa_N etch that patterns the 2DEG into IDTs. When comparing the performance of this device with an equivalent design that uses metal IDTs we noted a $3\times$ drop in the extracted mechanical Q of the device which can be associated with the additional loss mechanisms induced by the metal itself, the interfacial scattering and mass loading. This type of device can provide a way of directly interrogating the material properties of the GaN crystal, in the absence of metal loading. While GaN is heavily used in electronics and optics, people have only recently started using it for MEMS resonators. As a result, the mechanical properties of the heterostructures are not optimized for high acoustic performance. Having a tool that can intimately characterize the material properties can be used for providing feedback to the material growers and optimizing GaN heterostructures for MEMS applications.

Finally, recent years have seen a large push towards scaling of these resonators to high frequencies (10s of GHz for personal navigation, LAN, satellite communications, etc.) At such frequencies of operation passive resonators suffer from increased parasitics, especially a high capacitive floor, which eventually overwhelms the signal and degrades signal-to-noise ratio (SNR). Active transistor sensing of the acoustic waves can boost the SNR via an additional internal amplification of the mechanical signal prior to external parasitics. We applied this concept to GaN technology, where we can leverage piezoelectricity and high gain transistors. We demonstrated GaN Resonant Body Transistors (RBTs) up to 3.5 GHz, the highest contour mode (defined by in-plane cavity length) frequency in GaN resonators to date. To further enhance the SNR of the RBTs, we then implemented the first mechanically-coupled RBT, where the drive transducer and sense HEMT were embedded in two separate resonators that were coupled mechanically via half-wavelength beams. This provided additional electrical isolation, leading to $100\times$ increase in SNR compared to previous devices.

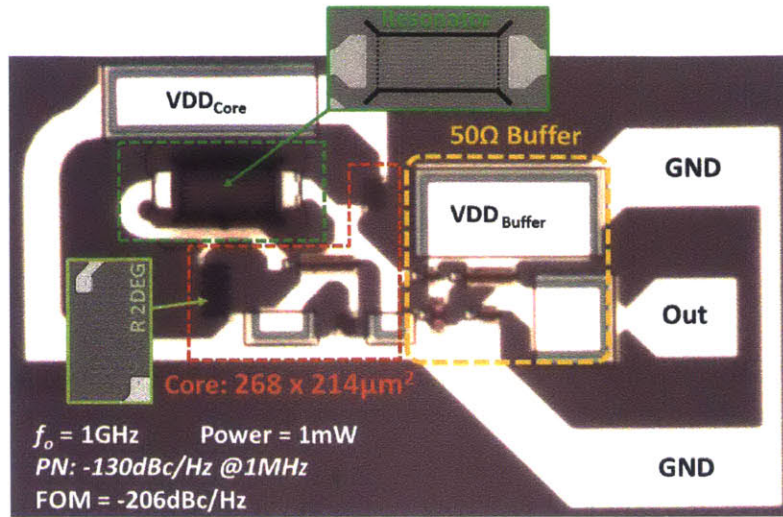


Figure 7-1: Circuit micrograph of 1GHz monolithic Pierce oscillator with GaN Lamb-mode MEMS resonator [14].

7.2 Future Directions

The GaN platform developed in this thesis leverages both high performance piezoelectric resonators and high gain active electronics showing high potential for high sensitivity monolithic sensors as well as for investigating mesoscopic phenomena. The availability of high gain transistors allows for a direct electronic readout of the mechanical signal. Already, in our research group, we were able to use the resonators demonstrated in this thesis to build the first monolithic GaN MEMS-based oscillators, where active HEMTs along with passives and resonators are all integrated on the same chip [14].

7.2.1 Sensors

Extending the functionality of our GaN resonators to include bulk resonant sensors can lead to extraordinary breakthroughs in terms of sensitivity, stability and shock reliability. We can use the strain dependent 2DEG in a variety of physical sensors, especially inertial sensors. Typical resonant inertial sensors operate at lower frequencies (10's kHz to 10 MHz). In this range, we are not limited by the resistivity of the 2DEG, which allows us to use it instead of metal for electrodes. This can increase

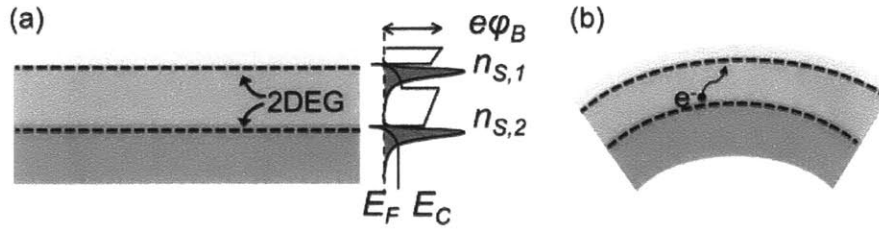


Figure 7-2: Heterostructures with band structures that contain multiple potential wells can be realized (a). In the presence of an applied strain field (b), the barrier height between the two 2DEG regions will change, leading to variations in the tunneling probability between the two electron gases.

transduction efficiency, and lead to higher displacements, higher signal-to-noise ratio. Additionally, active pick-off using HEMT sensing provides an increase in signal-to-noise ratio, allowing for miniaturization and, implicitly higher shock reliability.

Another important direction is the collaboration with material growers to strain engineer heterostructures that contain multiple 2DEGs. This can enable not only new kinds of transduction and enhanced sensitivity in the case of sensors, but also novel means of investigating phenomena such as quantum tunneling and mesoscopic interactions. For example, such a multi 2DEG heterostructure can be used to enable strain dependent tunneling from one 2DEG region to the other one.

7.2.2 Mesoscopic Physics

The ability to couple 2D electron systems and acoustic cavities enables the study of a variety of quantum and mesoscopic phenomena. It can allow to investigate tunneling between different 2DEG islands due to induced strain fields, as well as shot noise and back action phenomena. A giant acoustoelectric effect resulting from the interaction of the waves with the 2DEG has been demonstrated in GaAs systems [111]. Another example of mesoscopic phenomena in such systems is the actuation of an acoustic resonator through the back-action of electrons tunneling through a Quantum Point Contact in an AlGaAs/GaAs heterostructure, as shown in [112]. While AlGaAs/GaAs heterostructures involve modulation doping, AlGaN/GaN systems provide a higher density 2DEG without the need for doping and are 5 times more piezoelectric which

leads to higher magnitudes in the phenomena mentioned above. Larger SNR in these studies can facilitate a shift from cryogenic test temperatures to more practical ranges, enabling a new class of sensors and systems.

Appendix A

Material Properties

A.1 Piezoelectric Wurtzite Materials

For the wurtzite crystal, the elasticity matrix is given by:

$$C_{hexagonal} = \begin{bmatrix} c_{11} & c_{12} & c_{13} & 0 & 0 & 0 \\ c_{12} & c_{11} & c_{13} & 0 & 0 & 0 \\ c_{13} & c_{13} & c_{33} & 0 & 0 & 0 \\ 0 & 0 & 0 & c_{44} & 0 & 0 \\ 0 & 0 & 0 & 0 & c_{44} & 0 \\ 0 & 0 & 0 & 0 & 0 & c_{66} \end{bmatrix}, \quad (\text{A.1})$$

and the piezoelectric matrix is:

$$[e] = \begin{bmatrix} 0 & 0 & 0 & 0 & e_{51} & 0 \\ 0 & 0 & 0 & e_{51} & 0 & 0 \\ e_{31} & e_{31} & e_{33} & 0 & 0 & 0 \end{bmatrix}. \quad (\text{A.2})$$

To compute the coefficients of AlGaN we use Vegard's law for tertiary compound materials to interpolate between the material properties of AlN and GaN [113]. Then the material properties of GaN, AlGaN, and AlN are listed in Table A.1.

Table A.1: Wurtzite GaN, AlN and AlGaN material properties used in simulations

	Parameter	GaN	AlN	AlGaN	Units
Density	ρ	6150	3255	5455	C/m^2
Stiffness constants	c_{11}	390	410	395	GPa
	c_{12}	145	149	146	GPa
	c_{13}	106	99	104	GPa
	c_{33}	398	389	396	GPa
	c_{44}	105	125	110	GPa
	c_{66}	122	130	124	GPa
Piezoelectric constants	e_{31}	-0.3	-0.58	-0.39	C/m^2
	e_{33}	0.65	1.55	0.87	C/m^2
	e_{15}	-0.33	-0.48	-0.39	C/m^2
Dielectric constants	ϵ_r	8.9	8.5	8.8	$10^{-11} F/m$

A.2 Isotropic Materials

The elastic properties of the isotropic materials used in the MMIC stack are listed below.

The ohmic stack is composed of 25 nm of Tantalum and 100 nm of Aluminum. We then compute equivalent material properties assuming the propagation of in-plane waves through layered materials. For example, the density is given by the average of the two layers' density, weighted by their respective thickness:

$$\rho_{Ohmic} = \frac{\rho_{Al}t_{Al} + \rho_{Ta}t_{Ta}}{t_{Ta} + t_{Al}}, \quad (\text{A.3})$$

and the acoustic velocity is given by

$$\rho_{Ohmic} = \frac{Y_{Al}t_{Al} + Y_{Ta}t_{Ta}}{\rho_{Al}t_{Al} + \rho_{Ta}t_{Ta}}, \quad (\text{A.4})$$

where ρ , t , and Y represent the density, thickness and Young's modulus of the layers.

Table A.2: Material properties of isotropic materials used in simulations.

	Parameter	Ni	Ta	Al	Ohmic	Si_3N_4	Units
Density	ρ	8908	16690	2700	5498	2500	$kg \cdot m^{-3}$
Young's Modulus	c_{11}	200	186	70	93	160	GPa
Poisson Ratio	e_{31}	0.31	0.34	0.35	0.25	0.31	C/m^2
Phase Velocity	v	4738	3338	5092	4117	8000	m/s
Resistivity	ρ_{el}	69.3	131	28.2	48.8	–	C/m^2
Dielectric constant	ϵ	–	–	–	–	7	$10^{-11} F/m$

Appendix B

Fabrication Procedures

B.1 Au-free Fabrication Procedure

I: Alignment Marks

A. Deposit SiO₂ hard mask

Use STS-cvd, recipe HFSiO. Deposition time is approximately 3:45 min to obtain a thickness of 300 nm. In principle an oxide thickness of less than 200 nm suffices for the GaN alignment mark etch and is easier to pattern.

B. Coat with PMMA

Samples are dehydrated at 180C for 2 min. Use PMMA Spinner, PMMA A11, spread for 5s at 500 rpm, with acceleration 5000 rpm, spin for 45s 2000 rpm, acceleration 5000 rpm. Bake for 90s at 180C.

Note: when PMMA A8 was used, the film was too thin and it did not last enough through the oxide etch.

C. Elionix Exposure

Use 40 nA current, with 20000 points resolution, 0.320 dose. Develop in MIBK:IPA 1:2 for 90 sec.

D. Oxide Etch

Use a slow etch recipe to avoid resist burning: CH₄H₂_HU. Run it 3 times (all 12 steps). Soak in acetone for 1 hour, ash in barrel asher for 10 min.

E. GaN Etch

Clean the chamber with recipe 91. Run recipe 22, LP3. First condition for 2 min on step 4, then etch for 7 min.

F. Remove Oxide Mask

BOE for 1 min (the HF oxide deposited in sts-cvd is porous and the etch rate previously observed is approximately 290 nm per min.)

II: Mesa Etch

A. Coat with maN-2403

Use PMMA Spinner: spread for 5s at 500 rpm, with acceleration 5000 rpm, spin for 45 s at 1500 rpm, acceleration 5000 rpm. Bake for 60 s at 95 C. Note that this is true for the hotplate by the PMMA room, but it needs to be checked for other hotplates.

B. Elionix Exposure

Used 40 nA current, with 20000 points resolution, 0.18 dose.

Note that the ideal exposure conditions for maN have been found to change drastically with sample surface conditions, air humidity and shelf time of the resist. As a result, it is important to run an exposure matrix before the final exposure. Develop in MF-CD-26 for 120 sec. For etching purposes, hardbake for 10 min in the low temp oven (95 C, called softbake) to increase endurance of the mask.

C. AlGaN etch

Use GaNetch recipe. First condition the chamber by running full recipe (250 sec). A 250 sec etch time will result in a 70 nm step height. Leave in acetone for an hour; ash for 10 min in barrel asher.

III: Ohmic Contact

A. Coat with PMMA

Samples were dehydrated at 180C for 2 min. Use PMMA Spinner, PMMA

A8, spread for 5s at 500 rpm, with acceleration 5000, spin for 45 s at 2000 rpm, acceleration 5000. Bake for 90s at 180 C.

B. Elionix Exposure

Used 40nA current, with 20000 points resolution, 0.320 dose. Develop in MIBK:IPA 1:2 for 90 sec.

C. Metal Deposition and Anneal

Ashed in barrel asher at 800W for 5 min; then did H₂O dip for 1 min, H₂O:HCl 3:1 dip for 1 min, H₂O dip for one min. Deposit metal in Ebeam-Au: 5nm Ta, 100 nm Al, 20 nm Ta. Soak in acetone for almost 20 hours; sonicated at power level 2 for 1 min. Ashed at 1000W in barrel asher for 10 min. Anneal in RTA 35 with recipe GaN600, in folder GaN for 10 min at 600 C. Note that this tool was decommissioned, so a new recipe needs to be optimized on the new RTP tool.

IV: Gate Metal

A. Coat with PMMA

Samples were dehydrated at 180C for 2 min. Use PMMA Spinner, PMMA A8, spread for 5s at 500 rpm, with acceleration 5000, spin for 45 s at 2000 rpm, acceleration 5000. Bake for 90s at 180 C.

B. Elionix Exposure

Used 40nA current, with 20000 points resolution, 0.320 dose. Develop in MIBK:IPA 1:2 for 90 sec.

C. Metal Deposition

Ashed in barrel asher at 800W for 5 min; no acid dip: oxidation actually helps with gate leakage current. Deposit metal in Ebeam-FP or Ebeam-au: 100 nm Ni, leave in acetone over night. Squirted acetone and IPA. Ashed at 1000W in barrel asher for 10 min.

V: Passivation

A. Nitride Deposition

Condition with 5 min of HFSiN. Use HF SiN with 1 min stabilization, deposit for 8 min (62 nm); then MFSiN with 1 min stabilization, 8 min dep (142 nm).

VI: Deep GaN Etch

A. Coat with man-2403

Samples were dehydrated at 180C for 2 min. Use PMMA Spinner: spread for 5s at 500 rpm, with acceleration 5000, spin for 45s at 1500 rpm, acceleration 5000. Bake for 60s at 95C. Note that this is true for the hotplate by the PMMA room, need to check for other hotplates.

B. Elionix Exposure

Use 60000 points, current 2nA, exposure time 0.3. Develop in MF-CD-26 for 120 sec. Then reflow 125C for 60 sec to smooth the sidewalls of the resist.

C. Metal Mask Deposition

Deposit in Ebeam-fp: 5 nm Ti, 80 nm Ni. Leave in acetone over night and sonicate for 2 min at power level 3.

D. Etch Nitride

Etch in plasmaquest using CF4_BL recipe for 350 sec. Condition the chamber first by running entire process. Etched approximately 100 nm in 150 sec.

E. Etch GaN

Etch in SAMCO, using Recipe 23 for 16 min.

F. Remove Hard Mask

Nickel etchant for 2 min with hard agitation; Ti etchant for 10 sec.

VII: Open Via

A. Coat with SPR 700-1

Use Coater: spread for 3s at 750 rpm, spin for 30s at 2000 rpm. Bake for

90s at 95C. With a Q-tip soaked in acetone clean beading from the corners of the piece.

B. MA-6 exposure

Low vacuum setting, 10 sec exposure. Postbake for 90s at 115C. Develop in MF-CD-26 for 2 min. Hardbake for 90 seconds at 125 C.

C. Etch Nitride

Etch in plasmaquest using CF4_BL recipe for 350 sec. Condition the chamber first by running entire process. Etched approximately 100 nm in 150 sec. Soak in acetone for 2 hours; ash in barrel asher for 10 min.

VIII: Metal Pad

A. Coat with AZ-5214

Use Coater: spread for 3s at 750 rpm, spin for 30s at 2000 rpm. Bake for 5 min at 80C. With a Q-tip soaked in acetone clean beading from the corners of the piece.

B. MA-6 exposure

Low vacuum setting, 10 sec exposure. Postbake for 1 min at 110C. Flood exposure for 100 sec. Develop in AZ 422 for 2 min and rinse with DI water.

C. Metal Deposition

Use Ebeam-au or Ebeam-fp, deposit 50 nm Ti, 250 nm Au. Soak in acetone overnight, sonicate at power level 2 for 1 min. Ash at 1000W in barrel asher for 10 min.

IX: Release Step

A. Coat with SPR 700-1

Use Coater: spread for 3s at 750 rpm, spin for 30s at 2000 rpm. Bake for 90s at 95C. With a Q-tip soaked in acetone clean beading from the corners of the piece.

B. MA-6 exposure

Low vacuum setting, 10 sec exposure. Postbake for 90s at 115C. Develop in MF-CD-26 for 2 min. Hardbake for 90 seconds at 125 C.

C. Xe2F Etch

Etch in Xe2F using 30 sec etch cycles. Etch through 2-3 cycles at first to get etch rate, which is highly dependent on surface area of the sample and exposed silicon substrate. Ash in barrel asher for approximately 2 hours to remove photoresist mask.

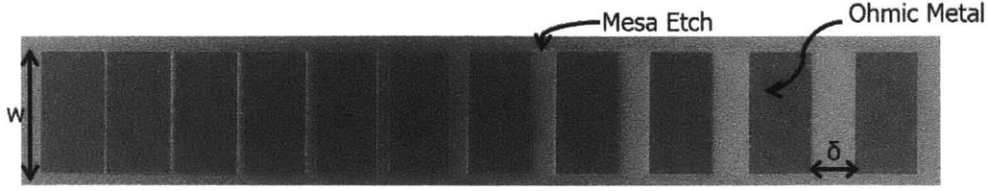


Figure B-1: SEM of fabricated TLM structure used for extracting contact resistance of Ta-based Ohmic metal to the 2DEG.

B.2 Au-free Ohmic Optimization

We use the Transmission-Line-Model (TLM) [114] to extract the contact resistance of the Ohmic metal, as well as the sheet resistance of the 2DEG, as shown in Figure B-1. The extracted DC IV characteristics are then fitted according to the model:

$$R_{Tot} = 2R_C + R_S \frac{\delta}{W}, \quad (\text{B.1})$$

where R_{Tot} is the total resistance measured between two different pads, R_C is the contact resistance, R_S is the sheet resistance of the 2DEG, δ is the separation between the two metal pads and W is the lateral dimension of the metal contact. Table B.1 shows the extracted parameters for various Tantalum-based ohmic metalizations. Dashed lines are used to represent cases when the linear Ohmic behavior has not been established.

Table B.1: Performance of different Ohmic metallizations as a function of anneal temperature.

Metalization (nm)	Temperature ($^{\circ}C$)	Time (min)	R_C ($\Omega \cdot mm$)	R_S (Ω/\square)
Ta(10)/Al(100)/Ta(20)	525	5	—	—
	550	5	—	—
	550	10	—	—
	575	5	—	—
	575	10	—	—
	600	10	2.5	379
Ta(5)/Al(140)/Ta(20)	550	10	—	—
	575	5	—	—
	575	10	5.3	487
	600	10	1.41	426
Ta(5)/Al(100)/Ta(20)	550	10	—	—
	575	5	—	—
	575	10	7.2	320
	600	10	0.9	400

Bibliography

- [1] R. M. White and F. W. Voltmer. "DIRECT PIEZOELECTRIC COUPLING TO SURFACE ELASTIC WAVES". *Applied Physics Letters*", 7(12), 1965.
- [2] R. Aigner. "High performance RF-filters suitable for above ic integration: film bulk-acoustic- resonators (FBAR) on silicon". In *Custom Integrated Circuits Conference, 2003. Proceedings of the IEEE 2003*, pages 141–146, Sept 2003.
- [3] M. Rinaldi, C. Zuniga, C. Zuo, and G. Piazza. "Ultra-thin Super High Frequency two-port ALN contour-mode resonators and filters". In *Solid-State Sensors, Actuators and Microsystems Conference, 2009. TRANSDUCERS 2009. International*, pages 577–580, June 2009.
- [4] T. Niu and M. Palaniapan. "A 10 MHz micromechanical lame-mode bulk oscillator operating in nonlinear region". *Procedia Engineering*, 5(0):1450 – 1453, 2010. Eurosensor {XXIV} Conference Eurosensor {XXIV} Conference.
- [5] G. Piazza, P.J. Stephanou, and A.P. Pisano. "Single-Chip Multiple-Frequency ALN MEMS Filters Based on Contour-Mode Piezoelectric Resonators". *Microelectromechanical Systems, Journal of*, 16(2):319–328, April 2007.
- [6] Y. Takagaki, P. Santos, E. Wiebicke, O. Brandt, H.-P. Schönherr, and K. Ploog. "Guided propagation of surface acoustic waves in AlN and GaN films grown on 4H – SiC(0001) substrates". *Phys. Rev. B*, 66:155439, Oct 2002.
- [7] L.C. Popa and D. Weinstein. "Switchable piezoelectric transduction in Al-GaN/GaN MEMS resonators". In *Solid-State Sensors, Actuators and Microsystems (TRANSDUCERS EUROSENSORS XXVII), 2013 Transducers Eurosensors XXVII: The 17th International Conference on*, pages 2461–2464, June 2013.
- [8] V.J. Gokhale, J. Roberts, and M. Rais-Zadeh. "High performance bulk mode gallium nitride resonators and filters". In *Solid-State Sensors, Actuators and Microsystems Conference (TRANSDUCERS), 2011 16th International*, pages 926–929, June 2011.
- [9] A. Ansari, V.J. Gokhale, J. Roberts, and M. Rais-Zadeh. "Monolithic integration of GaN-based micromechanical resonators and HEMTs for timing applications". In *Electron Devices Meeting (IEDM), 2012 IEEE International*, pages 15.5.1–15.5.4, Dec 2012.

- [10] L.C. Popa and D. Weinstein. "2DEG electrodes for piezoelectric transduction of AlGa_N/Ga_N MEMS resonators". In *European Frequency and Time Forum International Frequency Control Symposium (EFTF/IFC), 2013 Joint*, pages 922–925, July 2013.
- [11] A. Muller, D. Neculoiu, George Konstantinidis, A. Stavrinidis, D. Vasilache, Alina Cismaru, M. Danila, Mircea Dragoman, G. Deligeorgis, and K. Tsagaraki. "6.3-GHz Film Bulk Acoustic Resonator Structures Based on a Gallium Nitride/Silicon Thin Membrane". *Electron Device Letters, IEEE*, 30(8):799–801, Aug 2009.
- [12] A. Ansari and M. Rais-Zadeh. "An 8.7 GHz Ga_N micromechanical resonator with an integrated AlGa_N/Ga_N HEMT". In *Solid-State Sens., Actuators, Microsyst. Workshop, Hilton Head Island, SC, USA*, Jun 2014.
- [13] M. Shahmohammadi, B.P. Harrington, and R. Abdolvand. "Concurrent enhancement of Q and power handling in multi-tether high-order extensional resonators". In *Microwave Symposium Digest (MTT), 2010 IEEE MTT-S International*, pages 1452 – 1455, May 2010.
- [14] B. Bahr, L.C. Popa, and D. Weinstein. "1GHz Ga_N-MMIC Monolithically Integrated MEMS-Based Oscillators". In *Solid-State Circuits Conference, 2015. ISSCC 2015. Digest of Technical Papers. IEEE International*, page to appear, Feb 2015.
- [15] A. Kourepenis, J. Borenstein, J. Connelly, R. Elliott, P. Ward, and M. Weinberg. "Performance of MEMS inertial sensors". In *Position Location and Navigation Symposium, IEEE 1998*, pages 1–8, Apr 1998.
- [16] G. K. Fedder, R. T. Howe, T.-J. K. Liu, and E. P. Quevy. "Technologies for cofabricating MEMS and electronics". *Proceedings of the IEEE*, 96(2):306–322, 2008.
- [17] H. Xie, L. Erdmann, X. Zhu, K. J. Gabriel, and G. K. Fedder. "Post-CMOS processing for high-aspect-ratio integrated silicon microstructures". *Microelectromechanical Systems, Journal of*, 11(2):93–101, 2002.
- [18] B. Otis and J. Rabaey. *"Ultra-low power wireless technologies for sensor networks"*. Springer, 2007.
- [19] J. Mitola and Jr. Maguire, G.Q. "Cognitive radio: making software radios more personal". *Personal Communications, IEEE*, 6(4):13–18, Aug 1999.
- [20] E.H. Armstrong. "A New System of Short Wave Amplification". *Radio Engineers, Proceedings of the Institute of*, 9(1):3–11, Feb 1921.
- [21] J. Huijsing, R.J. van de Plassche, and W. Sansen. *Analog Circuit Design: Low-Noise, Low-Power, Low-Voltage; Mixed-Mode Design with CAD Tools; Voltage, Current and Time References*. Springer, 1996.

- [22] W.G. Cady. "The piezoelectric resonator". *Physical Review A*, 17:531–533, 1921.
- [23] E.A. Gerber and R.A. Sykes. "Quartz frequency standards". *Proceedings of the IEEE*, 55(6):783–791, 1967.
- [24] T. Matsuda, H. Uchishiba, O. Ikata, T. Nishihara, and Y. Satoh. "L and S band low-loss filters using SAW resonators". In *Ultrasonics Symposium, 1994. Proceedings., 1994 IEEE*, volume 1, pages 163–167 vol.1, Oct 1994.
- [25] D. Weinstein, S.A. Bhave, S. Morita, S. Mitarai, and K. Ikeda. "Frequency scaling and transducer efficiency in internal dielectrically transduced silicon bar resonators". In *Solid-State Sensors, Actuators and Microsystems Conference, 2009. TRANSDUCERS 2009. International*, pages 708–711, June 2009.
- [26] J.I. Pankove, E.A. Miller, and J.E. Berkeyheiser. "GaN electroluminescent diodes". In *Electron Devices Meeting, 1971 International*, volume 17, pages 78–78, 1971.
- [27] R. Tabrizian, M. Rais-Zadeh, and F. Ayazi. "Effect of phonon interactions on limiting the f_q product of micromechanical resonators". In *Solid-State Sensors, Actuators and Microsystems Conference, 2009. TRANSDUCERS 2009. International*, pages 2131–2134, June 2009.
- [28] Semiconductors on NSM. <http://www.ioffe.ru/SVA/NSM/Semicond/GaN/>. Accessed: 2014-12-20.
- [29] S. Adachi. "Physical Properties of III-V Semiconductor Compounds". *JOHN WILEY & SONS, NEW YORK, NY(USA)*, 1992, 318, 1992.
- [30] H. Ledbetter, H. Ogi, and N. Nakamura. "Elastic, anelastic, piezoelectric coefficients of monocrystal lithium niobate". *Mechanics of materials*, 36(10):941–947, 2004.
- [31] A. D. Hanser and K. R. Evans. "Development of the Bulk GaN Substrate Market". In Dirk Ehrentraut, Elke Meissner, and Michal Bockowski, editors, *Technology of Gallium Nitride Crystal Growth*, volume 133 of *Springer Series in Materials Science*, pages 3–27. Springer Berlin Heidelberg, 2010.
- [32] T.E. Kazior, R. Chelakara, W. Hoke, J. Bettencourt, T. Palacios, and H.S. Lee. "High Performance Mixed Signal and RF Circuits Enabled by the Direct Monolithic Heterogeneous Integration of GaN HEMTs and Si CMOS on a Silicon Substrate. In *Compound Semiconductor Integrated Circuit Symposium (CSICS), 2011 IEEE*, pages 1–4, Oct 2011.
- [33] V. Cimalla, J. Pezoldt, and O. Ambacher. "Group III nitride and SiC based MEMS and NEMS: materials properties, technology and applications". *Journal of Physics D: Applied Physics*, 40(20):6386, 2007.

- [34] C. Samori, S. Levantino, and A.L. Lacaita. "Integrated LC oscillators for frequency synthesis in wireless applications". *Communications Magazine, IEEE*, 40(5):166–171, May 2002.
- [35] B. Razavi. *"RF Microelectronics"*. Prentice-Hall, Inc., Upper Saddle River, NJ, USA, 1998.
- [36] L. Baggio and *et.al.* Bignotto, M. "A joint search for gravitational wave bursts with AURIGA and LIGO". *Classical and Quantum Gravity*, 25(9):095004, 2008.
- [37] D.B. Sullivan. "Time and frequency measurement at NIST: the first 100 years". In *Frequency Control Symposium and PDA Exhibition, 2001. Proceedings of the 2001 IEEE International*, pages 4–17, 2001.
- [38] H. Goldstein, C.P. Poole, and J.L. Safko. *"Classical Mechanics"*. Addison Wesley, 2002.
- [39] G.R. Fowles and G.L. Cassiday. *"Analytical mechanics"*. Thomson Brooks/Cole, 2005.
- [40] V. B. Braginsky, V. P. Mitrofanov, V. I. Panov, and J. H. Hetherington. "Systems with Small Dissipation" (First published in Moscow in 1981 as "Sistemis Maloi Dissipatsiei" by v. b. braginsky, v. p. mitrofanov, and v. i. panov) (translated by erast gliner). *Journal of the Acoustical Society of America*, 81(5):1652, 1987.
- [41] B.A. Auld. *"Acoustic fields and waves in solids"*. Number v. 2 in Acoustic Fields and Waves in Solids. R.E. Krieger, 1990.
- [42] "IEEE Standard on Piezoelectricity". *ANSI/IEEE Std 176-1987*, 1988.
- [43] H. Lamb. "On Waves in an Elastic Plate". *Proceedings of the Royal Society of London. Series A, Containing Papers of a Mathematical and Physical Character (1905-1934)*, 93(648):114–128, 1917.
- [44] A. Beliveau, G.T. Spencer, K.A. Thomas, and S.L. Roberson. "Evaluation of MEMS capacitive accelerometers". *Design Test of Computers, IEEE*, 16(4):48–56, Oct 1999.
- [45] S. D. Senturia. *"Microsystem design"*, volume 3. Kluwer academic publishers Boston, 2001.
- [46] G. Gautschi. *"Piezoelectric sensorics: force, strain, pressure, acceleration and acoustic emission sensors, materials and amplifiers"*. Springer, 2002.
- [47] P. Muralt, R.G. Polcawich, and S. Trolier-McKinstry. "Piezoelectric thin films for sensors, actuators, and energy harvesting". *MRS bulletin*, 34(09):658–664, 2009.

- [48] "IRE Standards on Piezoelectric Crystals: Determination of the Elastic, Piezoelectric, and Dielectric Constants-The Electromechanical Coupling Factor, 1958". *Proceedings of the IRE*, 46(4):764–778, April 1958.
- [49] R.M. White. "Surface elastic waves". *Proceedings of the IEEE*, 58(8):1238–1276, Aug 1970.
- [50] K. Hashimoto. *"Surface acoustic wave devices in telecommunications"*. Springer, 2000.
- [51] K. A. Ingebrigtsen. "Surface Waves in Piezoelectrics". *Journal of Applied Physics*, 40(7), 1969.
- [52] III. Larson, J.D., R.C. Bradley, S. Wartenberg, and R.C. Ruby. "Modified Butterworth-Van Dyke circuit for FBAR resonators and automated measurement system". In *Ultrasonics Symposium, 2000 IEEE*, volume 1, pages 863–868 vol.1, Oct 2000.
- [53] C. Seoáñez, F. Guinea, and A. H. Castro Neto. "Surface dissipation in nanoelectromechanical systems: Unified description with the standard tunneling model and effects of metallic electrodes". *Phys. Rev. B*, 77:125107, Mar 2008.
- [54] B.P. Harrington and R. Abdolvand. "In-plane acoustic reflectors for reducing effective anchor loss in lateralÅŞextensional MEMS resonators". *Journal of Micromechanics and Microengineering*, 21(8):085021, 2011.
- [55] S. Wang, L.C. Popa, and D. Weinstein. "GaN MEMS resonator using a folded phononic crystal structure". In *Solid-State Sens., Actuators, Microsyst. Workshop, Hilton Head Island, SC, USA*, pages 72–75, Jun 2014.
- [56] A. Akhiezer. "On the Absorption of Sound in Solids". *Journal of Physics (Moscow)*, 1:277–287, 1939.
- [57] L.D. Landau and G. Rumer. "On the absorption of sound in solids". *Phys. Z. Sowjetunion*, 11:18–25, 1937.
- [58] C. Kittel. *"Introduction to solid state physics"*. Wiley, 1986.
- [59] V. J Gokhale and M. Rais-Zadeh. "Phonon-electron interactions in piezoelectric semiconductor bulk acoustic wave resonators". *Scientific reports*, 4, 2014.
- [60] M. Pomerantz. "Ultrasonic loss and gain mechanisms in semiconductors". *Proceedings of the IEEE*, 53(10):1438–1451, Oct 1965.
- [61] A. R. Hutson, J. H. McFee, and D. L. White. "Ultrasonic Amplification in CdS". *Phys. Rev. Lett.*, 7:237–239, Sep 1961.
- [62] P. Perlin, C. Jauberthie-Carillon, J. P. Itie, A. San Miguel, I. Grzegory, and A. Polian. "Raman scattering and x-ray-absorption spectroscopy in gallium nitride under high pressure". *Phys. Rev. B*, 45:83–89, Jan 1992.

- [63] O Ambacher. "Growth and applications of Group III-nitrides". *Journal of Physics D: Applied Physics*, 31(20):2653, 1998.
- [64] W.E. Hoke, R.V. Chelakara, J.P. Bettencourt, T.E. Kazior, J.R. Laroche, T.D. Kennedy, J.J. Mosca, A. Torabi, A.J. Kerr, H.-S. Lee, and T. Palacios. "Monolithic integration of silicon CMOS and GaN transistors in a current mirror circuit". *Journal of Vacuum Science Technology B: Microelectronics and Nanometer Structures*, 30(2):02B101–02B101–6, Mar 2012.
- [65] F. Engelmark, G. Fucntes, I. V. Katardjiev, A. Harsta, U. Smith, and S. Berg. "Synthesis of highly oriented piezoelectric AlN films by reactive sputter deposition". *Vacuum Science and Technology, Journal of*, 18(4):1609–1612, 2000.
- [66] W. C. Oliver and G. M. Pharr. "An improved technique for determining hardness and elastic modulus using load and displacement sensing indentation experiments". *Journal of Materials Research*, 7:1564–1583, 1992.
- [67] J.-M. Wagner and F. Bechstedt. "Properties of strained wurtzite GaN and AlN: *Ab initio* studies". *Phys. Rev. B*, 66:115202, Sep 2002.
- [68] M. Rais-Zadeh, V.J. Gokhale, A. Ansari, M. Faucher, D. TheÀaron, Y. Cordier, and L. Buchailot. "Gallium Nitride as an Electromechanical Material". *Microelectromechanical Systems, Journal of*, 23(6):1252–1271, Dec 2014.
- [69] J.D. Plummer, M.D. Deal, and P.B. Griffin. *"Silicon VLSI Technology: Fundamentals, Practice and Modeling"*. Prentice Hall electronics and VLSI series. Prentice Hall, 2000.
- [70] D. Qiao, L. Jia, L. S. Yu, P. M. Asbeck, S. S. Lau, S.-H. Lim, Z. Liliental-Weber, T. E. Haynes, and J. B. Barner. "Ta-based interface ohmic contacts to AlGa_N/Ga_N heterostructures". *Journal of Applied Physics*, 89(10), 2001.
- [71] A. Malmros, H. Blanck, and N. Rorsman. "Electrical properties, microstructure, and thermal stability of Ta-based ohmic contacts annealed at low temperature for Ga_N HEMTs". *Semiconductor Science and Technology*, 26(7):075006, 2011.
- [72] D. Qiao, L. S. Yu, S. S. Lau, J. M. Redwing, J. Y. Lin, and H. X. Jiang. "Dependence of Ni/AlGa_N Schottky barrier height on Al mole fraction". *Journal of Applied Physics*, 87(2), 2000.
- [73] B.M. Green, K.K. Chu, E.M. Chumbes, J.A. Smart, J.R. Shealy, and L.F. Eastman. "The effect of surface passivation on the microwave characteristics of undoped AlGa_N/Ga_N HEMTs". *Electron Device Letters, IEEE*, 21(6):268–270, June 2000.
- [74] V. Belevitch. "Summary of the History of Circuit Theory". *Proceedings of the IRE*, 50(5):848–855, May 1962.

- [75] Ju-Young Kim, Min-Kwon Choi, and Seonghearn Lee. "A 'Thru-Short-Open' De-embedding Method for Accurate On-Wafer RF Measurements of Nano-Scale MOSFETs". *JOURNAL OF SEMICONDUCTOR TECHNOLOGY AND SCIENCE*, 12(1), 2012.
- [76] H. Ichihashi, T. Yanagitani, S. Takayanagi, M. Kawabe, and M. Matsukawa. "Gigahertz acoustic wave velocity measurement in GaN single crystals considering acousto-electric effect". *Ultrasonics, Ferroelectrics, and Frequency Control, IEEE Transactions on*, 61(8):1307–1313, August 2014.
- [77] N. Miller and G. Piazza. "Nonlinear dynamics in aluminum nitride contour-mode resonators". In *European Frequency and Time Forum International Frequency Control Symposium (EFTF/IFC), 2013 Joint*, pages 9–12, July 2013.
- [78] J. Segovia-Fernandez, A. Tazzoli, M. Rinaldi, and G. Piazza. "Nonlinear lumped electrical model for contour mode AlN resonators". In *Ultrasonics Symposium (IUS), 2011 IEEE International*, pages 1846–1849, Oct 2011.
- [79] Y.W. Lin, S.-S. Li, Z. Ren, and C.T.-C. Nguyen. "Third-order intermodulation distortion in capacitively-driven VHF micromechanical resonators". In *Ultrasonics Symposium, 2005 IEEE*, volume 3, pages 1592–1595, Sept 2005.
- [80] J. P. Ibbetson, P. T. Fini, K. D. Ness, S. P. DenBaars, J. S. Speck, and U. K. Mishra. "Polarization effects, surface states, and the source of electrons in AlGa_N/Ga_N heterostructure field effect transistors". *Applied Physics Letters*, 77(2), 2000.
- [81] F. Calle, J. Grajal, and J. Pedros. "Active SAW devices on 2DEG heterostructures". *Electronics Letters*, 40(21):1384–1386, Oct 2004.
- [82] N. Shigekawa, K. Nishimura, T. Suemitsu, H. Yokoyama, and K. Hohkawa. "SAW Filters Composed of Interdigital Schottky and Ohmic Contacts on AlGa_N/Ga_N Heterostructures". *Electron Device Letters, IEEE*, 28(2):90–92, Feb 2007.
- [83] N. Shigekawa, K. Nishimura, T. Suemitsu, H. Yokoyama, and K. Hohkawa. "Interdigital transducers with control gates on AlGa_N/Ga_N Heterostructures". *Applied Physics Letters*, 89(3):–, 2006.
- [84] K. Brueckner, F. Niebelschuetz, K. Tonisch, S. Michael, A. Dadgar, A. Krost, V. Cimalla, O. Ambacher, R. Stephan, and M. A. Hein. "Two-dimensional electron gas based actuation of piezoelectric AlGa_N/Ga_N microelectromechanical resonators". *Applied Physics Letters*, 93(17):–, 2008.
- [85] K.-Y. Wong, W. Tang, K. M. Lau, and K.J. Chen. "Surface acoustic wave device on AlGa_N/Al_{0.3}Ga_{0.7}N heterostructure using two-dimensional electron gas interdigital transducers". *Applied Physics Letters*, 90(21):–, 2007.

- [86] K. Tonisch, C. Buchheim, F. Niebelschutz, A. Schober, G. Gobsch, V. Cimalla, O. Ambacher, and R. Goldhahn. "Piezoelectric actuation of (GaN/)AlGaN/GaN heterostructures". *Journal of Applied Physics*, 104(8):-, 2008.
- [87] Y. Lv, Z. Lin, T. D. Corrigan, J. Zhao, Z. Cao, L. Meng, C. Luan, Z. Wang, and H. Chen. "Extraction of AlGaN/GaN heterostructure Schottky diode barrier heights from forward current-voltage characteristics". *Journal of Applied Physics*, 109(7):-, 2011.
- [88] L.-W. Hung and C.T.-. Nguyen. "Capacitive-Piezoelectric Transducers for High-Q Micromechanical AlN Resonators". *Microelectromechanical Systems, Journal of*, PP(99):1-1, 2014.
- [89] C. Cassella, J. Segovia-Fernandez, and G. Piazza. "Segmented electrode excitation of aluminum nitride contour mode resonators to optimize the device figure of merit". In *Solid-State Sensors, Actuators and Microsystems (TRANSDUCERS EUROSENSORS XXVII), 2013 Transducers Eurosensors XXVII: The 17th International Conference on*, pages 506-509, June 2013.
- [90] L.C. Popa and D. Weinstein. "L-band Lamb mode resonators in Gallium Nitride MMIC technology". In *Frequency Control Symposium (FCS), 2014 IEEE International*, pages 1-4, May 2014.
- [91] C.-M. Lin, V. Yantchev, J. Zou, Y.-Y Chen, and A.P. Pisano. "Micromachined One-Port Aluminum Nitride Lamb Wave Resonators Utilizing the Lowest-Order Symmetric Mode". *Microelectromechanical Systems, Journal of*, 23(1):78-91, Feb 2014.
- [92] F. Di Pietrantonio, M. Benetti, D. Cannata, R. Beccherelli, and E. Verona. "Guided lamb wave electroacoustic devices on micromachined AlN/Al plates". *Ultrasonics, Ferroelectrics, and Frequency Control, IEEE Transactions on*, 57(5):1175-1182, May 2010.
- [93] E.L. Adler. "Electromechanical coupling to Lamb and shear-horizontal modes in piezoelectric plates". *Ultrasonics, Ferroelectrics, and Frequency Control, IEEE Transactions on*, 36(2):223-230, March 1989.
- [94] A.H. Fahmy and E. L. Adler. "Propagation of acoustic surface waves in multilayers: A matrix description". *Applied Physics Letter*", 22(10), 1973.
- [95] Anonymous. "Proceedings of the American Physical Society". *Phys. Rev.*, 69:674-674, Jun 1946.
- [96] C.-M. Lin, T.-T. Yen, Y.-J. Lai, V.V. Felmetzger, M.A. Hopcroft, J.H. Kuypers, and A.P. Pisano. "Experimental study of temperature-compensated aluminum nitride Lamb wave resonators". In *Frequency Control Symposium, 2009 Joint with the 22nd European Frequency and Time forum. IEEE International*, pages 5-9, April 2009.

- [97] C.-M. Lin, T. Yen, Y.-J. Lai, V.V. Felmetzger, M.A. Hopcroft, J.H. Kuypers, and A.P. Pisano. "Temperature-compensated aluminum nitride lamb wave resonators". *Ultrasonics, Ferroelectrics, and Frequency Control, IEEE Transactions on*, 57(3):524–532, March 2010.
- [98] A. Ansari and M. Rais-Zadeh. "A Temperature-Compensated Gallium Nitride Micromechanical Resonator". *Electron Device Letters, IEEE*, 35(11):1127–1129, Nov 2014.
- [99] R. Marathe, B. Bahr, Wentao Wang, Z. Mahmood, L. Daniel, and D. Weinstein. "Resonant Body Transistors in IBM's 32 nm SOI CMOS Technology". *Microelectromechanical Systems, Journal of*, 23(3):636–650, June 2014.
- [100] D. Weinstein and S. A. Bhave. "Acoustic resonance in an independent-gate FinFET". In *Hilton Head*, pages 459–462, 2010.
- [101] B. Bahr, R. Marathe, and D. Weinstein. "Phononic crystals for acoustic confinement in CMOS-MEMS resonators". In *Frequency Control Symposium (FCS), 2014 IEEE International*, pages 1–4, May 2014.
- [102] M. Faucher, B. Grimbert, Y. Cordier, N. Baron, A. Wilk, H. Lahreche, P. Bove, M. Francois, P. Tilmant, T. Gehin, C. Legrand, M. Werquin, L. Buchailot, C. Gaquiere, and D. Theron. "Amplified piezoelectric transduction of nanoscale motion in gallium nitride electromechanical resonators". *Applied Physics Letters*, 94(23):233506–233506–3, Jun 2009.
- [103] A. Ansari and M. Rais-Zadeh. "HEMT-based read-out of a thickness-mode AlGa_N/Ga_N resonator". In *Electron Devices Meeting (IEDM), 2013 IEEE International*, pages 18.3.1–18.3.4, Dec 2013.
- [104] H.C. Nathanson, W.E. Newell, R.A. Wickstrom, and Jr. Davis, J.R. "The resonant gate transistor". *Electron Devices, IEEE Transactions on*, 14(3):117–133, Mar 1967.
- [105] M. Azize and T. Palacios. "Effect of substrate-induced strain in the transport properties of AlGa_N/Ga_N heterostructures". *Journal of Applied Physics*, 108(2):-, 2010.
- [106] J. Kuzmik, P. Javorka, A. Alam, M. Marso, M. Heuken, and P. Kordos. "Determination of channel temperature in AlGa_N/Ga_N HEMTs grown on sapphire and silicon substrates using dc characterization method". *Electron Devices, IEEE Transactions on*, 49(8):1496–1498, Aug 2002.
- [107] F.D. Bannon, J.R. Clark, and C.T.-C. Nguyen. "High-Q HF microelectromechanical filters". *Solid-State Circuits, IEEE Journal of*, 35(4):512–526, April 2000.

- [108] L.C. Popa and D. Weinstein. "1 GHz GaN resonant body transistors with enhanced off-resonance rejection". In *Solid-State Sens., Actuators, Microsyst. Workshop, Hilton Head Island, SC, USA*, pages 269–272, Jun 2014.
- [109] M.-H. Li, C.-S. Li, C.-H. Chin, C.-Y. Chen, and S.-S. Li. "An ultra-low power ovenized CMOS-MEMS resonator monolithically integrated with interface circuits". In *Micro Electro Mechanical Systems (MEMS), 2013 IEEE 26th International Conference on*, pages 753–756, Jan 2013.
- [110] A. Tazzoli, M. Rinaldi, and G. Piazza. "Ovenized high frequency oscillators based on aluminum nitride contour-mode MEMS resonators". In *Electron Devices Meeting (IEDM), 2011 IEEE International*, pages 20.2.1–20.2.4, Dec 2011.
- [111] M. Rotter, A. Wixforth, W. Ruile, D. Bernklau, and H. Riechert. "Giant acoustoelectric effect in GaAs/LiNbO₃ hybrids". *Applied Physics Letters*, 73(15):2128–2130, Oct 1998.
- [112] J. Stettenheim, M. Thalakulam, F. Pan, M. Bal, Z. Ji, W. Xue, L. Pfeiffer, K.W. West, M.P. Blencowe, and A.J. Rimberg. "A macroscopic mechanical resonator driven by mesoscopic electrical back-action". *Nature*, 466(7302):86–90, 2010.
- [113] A. R. Denton and N. W. Ashcroft. "Vegard's law". *Phys. Rev. A*, 43:3161–3164, Mar 1991.
- [114] H.H. Berger. "Models for contacts to planar devices". *Solid-State Electronics*, 15(2):145 – 158, 1972.